



THE HONG KONG
POLYTECHNIC UNIVERSITY

香港理工大學

Pao Yue-kong Library

包玉剛圖書館

Copyright Undertaking

This thesis is protected by copyright, with all rights reserved.

By reading and using the thesis, the reader understands and agrees to the following terms:

1. The reader will abide by the rules and legal ordinances governing copyright regarding the use of the thesis.
2. The reader will use the thesis for the purpose of research or private study only and not for distribution or further reproduction or any other purpose.
3. The reader agrees to indemnify and hold the University harmless from and against any loss, damage, cost, liability or expenses arising from copyright infringement or unauthorized usage.

IMPORTANT

If you have reasons to believe that any materials in this thesis are deemed not suitable to be distributed in this form, or a copyright owner having difficulty with the material being included in our database, please contact lbsys@polyu.edu.hk providing details. The Library will look into your claim and consider taking remedial action upon receipt of the written requests.

**NON-RARE-EARTH DOPED THIN-FILM
PHOTONIC MATERIALS WITH
ULTRABROADBAND NEAR-INFRARED
LUMINESCENCE**

BAI GONGXUN

Ph.D

The Hong Kong Polytechnic University

2016

The Hong Kong Polytechnic University

Department of Applied Physics

**NON-RARE-EARTH DOPED THIN-FILM
PHOTONIC MATERIALS WITH
ULTRABROADBAND NEAR-INFRARED
LUMINESCENCE**

BAI Gongxun

A thesis submitted in partial fulfillment of the requirements
for the degree of Doctor of Philosophy

December 2015

CERTIFICATE OF ORIGINALITY

I hereby declare that this thesis is my own work and that, to the best of my knowledge and belief, it reproduces no material previously published or written, nor material that has been accepted for the award of any other degree or diploma, except where due acknowledgement has been made in the text.

_____ (Signed)

_____ BAI Gongxun (Name of student)



Abstract

Photonic materials with near-infrared (NIR) luminescence have continuously received much attention, as they are promising for practical applications in optical telecommunication systems, biomedicine, and light sources. Recently, the development of novel Ni- and Bi-doped photonic materials with ultrabroadband NIR emission are very attractive. Succeeded by the current rare-earth (RE) doped photonic materials, Ni- and Bi-doped materials have great potential application as the gain medium in broadband optical amplifiers and tunable lasers. Since thin-film photonic materials are of great interest in planar optical amplifiers and other integrated photonic technologies. In this thesis, following the studied Ni- and Bi-doped photonic bulks, Ni- and Bi-doped thin-film materials have been synthesized and characterized in this study.

First, simultaneous ferroelectric and ultrabroadband NIR photoluminescence properties are presented in Ni²⁺-doped perovskite Ba_xSr_{1-x}TiO₃. Large tuning of NIR emission is realized by chemical substitution, due to the variation in crystal-field acting on Ni²⁺. In particular, Ni²⁺-doped Ba_{0.5}Sr_{0.5}TiO₃ possesses the most broadly emission band. Then, the dielectric and photoluminescence properties of Ni²⁺-doped Ba_{0.5}Sr_{0.5}TiO₃ were studied at different temperatures. Using Ni²⁺-doped perovskite oxide bulks as target, Ni²⁺-doped thin films were prepared by pulsed laser deposition (PLD). Large tuning of NIR PL is achieved by Ni²⁺-doped perovskite thin films via chemical substitution. In addition, based on strain engineering, tunable NIR



luminescence of Ni^{2+} doped SrTiO_3 thin film grown on piezoelectric $\text{Pb}(\text{Mg}_{1/3}\text{Nb}_{2/3})_{0.7}\text{Ti}_{0.3}\text{O}_3$ (PMN-PT) substrate has been demonstrated, through controlling the thickness of STO:Ni film and the modulated strain from PMN-PT.

Ultrabroadband NIR luminescence has also been observed in Bi-doped oxyfluoride germanate and phosphate glass thin films prepared by PLD. Their emission peaks show tunable performance with controlling oxygen pressure during PLD growth. Systematic investigation revealed that the origins of the luminescence were ascribed to Bi clusters. With the sensitization of Bi NIR active centers, enhanced broadband $\sim 2 \mu\text{m}$ luminescence of Ho^{3+} was realized in Bi/Ho codoped oxyfluoride germanate glass films with high energy transfer efficiency. These results are promising for the realizations of planar waveguide lasers in the NIR region for integrated optics.

In conclusion, Ni- and Bi-doped thin film photonic materials with ultrabroadband NIR luminescence have been developed in this study. Their NIR luminescent properties can be modulated by chemical substitution, strain engineering, and controlling the growth process. These results will be very helpful for a better scientific understanding of ultrabroadband NIR luminescence in non-rare-earth doped photonic materials and selection of the potential materials for a new generation of thin-film integrated photonic technology.



List of Publications

Peer-reviewed Journals

1. **G. X. Bai**, M. K. Tsang, and J. H. Hao, Tuning the luminescence of phosphors: beyond conventional chemical method. *Advanced Optical Materials*, 2015. 3, 431. (Highly cited paper in ESI, updated on Nov. 12, 2015)
2. **G. X. Bai**, Y. Zhang, and J. H. Hao, Chemical substitution-induced exceptional emitting-wavelength tuning in transition metal Ni²⁺-doped ferroelectric oxides with ultrabroadband near-infrared luminescence. *Journal of Materials Chemistry C*, 2014. 2(23) 4631-4635.
3. **G. X. Bai**, Y. Zhang, and J. H. Hao, Tuning of near-infrared luminescence of SrTiO₃:Ni²⁺ thin films grown on piezoelectric PMN-PT via strain engineering. *Scientific reports*, 2014. 4(1) 5724.
4. **G. X. Bai**, W. J. Jie, Z. B. Yang, and J. H. Hao, Temperature dependence of broadband near-infrared luminescence from Ni²⁺-doped Ba_{0.5}Sr_{0.5}TiO₃, *Journal of Applied Physics*, 2015, 118 (18), 183110.
5. L.-B. Huang*, **G. X. Bai***, W.-C. Wong, Z. B. Yang, W. Xu, J. H. Hao, Magnetic-assisted non-contact triboelectric nanogenerator converting mechanical energy into electricity and light-emissions. *Advanced Materials*, 2016, 28, 2744.
(* equal contribution)
6. **G. X. Bai** and J. H. Hao, Novel metal ion doped photonic materials with



- ultrabroadband near-infrared luminescence, *Sci. Adv. Today*, 2016, 2, 25228.
7. M.-K. Tsang, **G. X. Bai**, and J. Hao, Stimuli responsive upconversion luminescence nanomaterials and films for various applications. *Chemical Society Reviews*, 2015. 44 1585-1607. (Highly cited paper in ESI, updated on Nov. 12, 2015)
 8. B. B. Xu, **G. X. Bai**, J. C. Wang, Q. B. Guo, D. Z. Tan, W. B. Chen, X. F. Liu, S. F. Zhou, J. H. Hao, and J. R. Qiu, Enhanced broadband excited upconversion luminescence in Ho-doped glasses by codoping with bismuth. *Optics Letters*, 2014. 39(10) 3022-3025.
 9. B. B. Xu, J. H. Hao, Q. B. Guo, J. C. Wang, **G. X. Bai**, B. Fei, S. F. Zhou, and J. R. Qiu, Ultrabroadband near-infrared luminescence and efficient energy transfer in Bi and Bi/Ho co-doped thin films. *Journal of Materials Chemistry C*, 2014. 2(14) 2482-2487.
 10. L. B. Tang, R. B. Ji, X. M. Li, **G. X. Bai**, C. P. Liu, J. H. Hao, J. Y. Lin, H. X. Jiang, K. S. Teng, Z. B. Yang, and S. P. Lau, Deep ultraviolet to near-infrared emission and photoresponse in layered N-doped graphene quantum dots. *ACS Nano*, 2014. 8(6) 6312-6320.
 11. Z. P. Wu, **G. X. Bai**, Q. Hu, D. Guo, C. Sun, L. Ji, M. Lei, L. Li, P. Li, and J. Hao, Effects of dopant concentration on structural and near-infrared luminescence of Nd³⁺-doped beta-Ga₂O₃ thin films. *Applied Physics Letters*, 2015. 106(17) 171910.
 12. Z. P. Wu, Y. Zhang, **G. X. Bai**, W. Tang, J. Gao, and J. H. Hao, Effect of biaxial



strain induced by piezoelectric PMN-PT on the upconversion photoluminescence of BaTiO₃:Yb/Er thin films. *Optics Express*, 2014. 22(23) 29014-29019.

13. D. Peng, Q. Ju, X. Chen, R. Ma, B. Chen, **G. X. Bai**, J. Hao, X. Qiao, X. Fan, and F. Wang, Lanthanide-doped energy cascade nanoparticles: full spectrum emission by single wavelength excitation. *Chemistry of Materials*, 2015. 27(8) 3115-3120.
14. L. Chen, M.-C. Wong, **G. X. Bai**, W. Jie, and J. Hao, White and green light emissions of flexible polymer composites under electric field and multiple strains. *Nano Energy*, 14 (2014) 372.

Presentations in international conferences

1. **G. X. Bai**, Z. Yang & J. H. Hao, Strain-induced tunable near-infrared luminescence from SrTiO₃:Ni²⁺ thin film grown on piezoelectric PMN-PT, Oral presentation, the 2nd International Conference on Nanogenerators and Piezotronics, Atlanta, USA, June 9, 2014.
2. **G. X. Bai**, C. Y. Tang, K. L. Jim, X. M. Zhang, K. H. Fung, Y. Chai, Y. H. Tsang, J. Q. Yao, and D. G. Xu, Lensed water-core Teflon-amorphous fluoroplastics optical fiber The 3rd International Conference on Optofluidics (Optofluidcs2013) Conference poster, 15-17 August 2013, Hong Kong.



Acknowledgments

During three years of my stay at Department of Applied Physics, The Hong Kong Polytechnic University for a Ph. D. degree, I have had a very great time, both in academic and personal life. I would like to acknowledge everybody who have given endless support to me.

First and foremost I would like to acknowledge my supervisor, **Dr. Hao Jianhua**, for offering me the opportunity to pursue the Ph. D degree in Hong Kong. I wish to express deep gratitude to him, for his excellent guidance, invaluable suggestions, and constant inspiration throughout the period of my research and studies. His profound academic insight, enthusiasm for science, patient and generous assistance greatly contribute to improving my research works and completing the project. His edification will continue to benefit me throughout my future research career.

I would also like to thank Prof. Lau S. P., Prof. Yu S. F., Prof. Dai J. Y., Dr. Mak C. L., Dr. Tsang Y. H., Dr. Zhang X. M., Dr. Yan F., and Dr. Yuan J. K. for their assistance on my research and coursework studies. I also want to thank Dr. Lui Hardy, Dr. Lu W., and Dr. Chan Vincent for their help in facility utilization in our department.

I am gratefully to my research group members for their help and assistance in



my experiments. They include Dr. Zhang Y., Dr. Jie W. J., Dr. Xu B. B., Dr. Huang L. B., Dr. Lin H. H., Dr. Wei X. H., Dr. Wu Z. P., Mr. Yang Z. B., Mr. Tsang M. K., Ms. Chen L., Mr. Wong W. C., Mr. Yuan S. G., Mr. Xu W., Ms. Choi S. Y., and Ms. Tse M. Y.. Particularly Dr. Xu B. B. for his contribution in preparation and characterization of Bi doped glass thin film.

Additional gratitude is given to my friends and colleagues, including Dr. Tang L. B., Dr. Lin S. H., Dr. Tao L. L., Dr. Liu Z. K., Dr. Jian A. Q., Dr. Wang N., Dr. Wu X., Dr. Lin M., Mr. Zhao Y. D., Mr. Li Y. Y., Mr. Chen Q. M., Ms. Long H., Mr. Bao Z. Y., Mr. Jin L. M., Mr. Tang C. Y., Mr. Li T. H., Mr. Yuan Y., Mr. Xiang N., for their friendship, company, and assistance. I would also like to acknowledge my co-operators for our collaborative works. They include Ms. Shi J. Y., Dr. Chen S. J., Dr. Zhao E. G., Dr. Peng D. F..

I gratefully show appreciation to the financial support from the Research Grants Council of Hong Kong (GRF No. PolyU 5002/12P).

Finally from my heart, I would like to thank my parents Bai Qiang and Cui Airong, for their constant support and encouragement, endless love in my study and life.



Table of Contents

Abstract.....	I
List of Publications.....	III
Peer-reviewed Journals	III
Presentations in international conferences	V
Acknowledgments	VI
Table of Contents	VIII
List of Figures.....	XIV
List of Tables	XXIII
List of Symbols	XXIV
List of Acronyms	XXV
Chapter 1 Introduction.....	1
1.1 Background of NIR luminescence	1
1.2 Metal ions-doped photonic materials with NIR luminescence	4



1.3 Current status of non-rare-earth ions doped photonic materials with ultrabroadband NIR luminescence	8
1.3.1 Ni-doped photonic materials with NIR luminescence	8
1.3.2 Bi-doped photonic materials with NIR luminescence	16
1.4 Motivation of research	30
1.5 Structure of thesis.....	33
Chapter 2 Experimental Techniques.....	35
2.1 Sample preparation	35
2.1.1 Fabrication of the bulk samples	35
2.1.2 Pulsed laser deposition (PLD)	36
2.2 Structure characterization	38
2.2.1 X-ray diffraction (XRD)	38
2.2.2 Scanning electron microscopy (SEM)	40
2.2.3 Raman spectroscopy	41
2.3 Luminescence characterization.....	46



2.3.1	Steady-state photoluminescence (PL).....	46
2.3.2	Time-resolved PL.....	49
2.4	Electrical characterization.....	51
2.4.1	Ferroelectric measurement.....	51
2.4.2	Dielectric measurement.....	52
Chapter 3 Ni-doped Photonic Materials with Broadband NIR Luminescence		54
3.1	Chemical substitution-induced emission modulation in Ni ²⁺ -doped ferroelectric oxides	54
3.1.1	Introduction of tunable NIR PL and Ni ²⁺ -doped ferroelectric oxides	54
3.1.2	Samples preparation and measurements of Ni ²⁺ -doped BST- <i>x</i>	57
3.1.3	Results and discussion of Ni ²⁺ -doped BST- <i>x</i>	58
3.1.4	Conclusion of Ni ²⁺ -doped ferroelectric oxides	70
3.2	Temperature dependence of broadband NIR luminescence from Ni ²⁺ -doped Ba _{0.5} Sr _{0.5} TiO ₃	71



3.2.1 Introduction of Ni ²⁺ -doped BST	71
3.2.2 Ni ²⁺ -doped BST Samples preparation and measurements	72
3.2.3 Results and discussion of Ni ²⁺ -doped BST	73
3.2.4 Conclusion of Ni ²⁺ -doped BST	82
3.3 Ni ²⁺ -doped barium strontium titanate thin films with broadband NIR luminescence	84
3.3.1 Background of barium strontium titanate thin films	84
3.3.2 Ni-doped thin-film sample preparation and measurements	85
3.3.3 Ni ²⁺ -doped ferroelectric thin films with broadband NIR luminescence	87
3.3.4 Ni ²⁺ -doped SrTiO ₃ thin films with broadband NIR luminescence ...	90
3.3.5 Conclusion of Ni ²⁺ -doped barium strontium titanate thin films	92
Chapter 4 Strain-Induced Modification of NIR Luminescence of SrTiO₃:Ni²⁺ Thin Films	94
4.1 Introduction of tunable luminescence.....	94



4.2	Preparation and measurements of STO:Ni thin films.....	98
4.3	Misfit strain induced tunable NIR luminescence	99
4.4	Piezoelectric-induced tunable NIR luminescence.....	105
4.5	Conclusions of strain induced tunable PL in STO:Ni thin film	112
Chapter 5 Broadband NIR Luminescence from Bi and Bi/Ho co-doped Thin Films		113
5.1	Introduction	113
5.2	Preparation and measurements of Bi doped thin films.....	115
5.3	Results and discussion of Bi-doped thin films	116
5.3.1	Bi and Bi/Ho codoped germanate glass thin films.....	116
5.3.2	Bi doped phosphate glass thin films.....	129
5.4	Conclusion of Bi doped thin films.....	132
Chapter 6 Conclusions and Suggestions for Future Work.....		134
6.1	Conclusions of the thesis.....	134
6.2	Suggestions for future work	138



References.....142



List of Figures

- Figure 1.1 Electromagnetic spectrum with NIR light highlighted [Harvey, 2015].
..... 1
- Figure 1.2 (a) The loss spectra of fiber & various kinds of rare-earth (RE) doped amplifiers. (b) Optical windows in biological tissues [Smith, 2009]. 2
- Figure 1.3 Typical energy level diagrams of metal ions with NIR emission..... 6
- Figure 1.4 (a) Emission spectra of Ni-doped YAlO_3 , MgO , $\text{Gd}_3\text{Ga}_5\text{O}_{12}$, and MgF_2 crystals at room temperature. (b) Tanabe-Sugano diagram for the d^8 electron configuration. The dashed area corresponds to the Dq/B values of octahedral Ni^{2+} [Kück, 2001]. (c) The absorption spectrum of a $\text{MgGa}_2\text{O}_4:\text{Ni}$ crystal at room temperature [Suzuki, 2010]. 8
- Figure 1.5 (a) Bright-field TEM image of GGO glass ceramics. The insets show the corresponding Selected-area electron diffraction patterns. (b) NIR luminescence spectra of GGO and BASO glass and glass ceramics samples under excitation with 808 and 980 nm lasers. [Zhou, 2009] (c) NIR emission spectra of glass ceramics containing nanocrystals $\text{Ga}_2\text{O}_3:\text{Ni}^{2+}$ with doping In^{3+} and F^- . (d) Configurations of regular $[\text{GaO}_6]$ octahedron, with doping In^{3+} and F^- [Zhou, 2013].



.....	11
Figure 1.6 (a) Fluorescence spectra from Ni-doped optical fibers with diverse heat treatment. (b) Combined Ni- and Tm-doped optical fiber source pumped at 1060 nm. [Samson, 2002].....	15
Figure 1.7 (a) NIR PL spectra of Bi-doped germanate glasses with various bismuth concentrations melted in air at 1500 °C, under 880 nm excitation. (b) NIR PL spectra of 1.0 mol. % Bi-doped glasses melted in air at various temperatures. All the spectra are excited by 880 nm. [Xu, 2013] (c) Fluorescence spectra of Bi-doped phosphate glass excited by different lasers [Wang, 2012]. (d) NIR PL spectra of glasses B and AB excited by 600 nm [Xu, 2013].	16
Figure 1.8 (a) The emission spectra of Bi doped glasses under femtosecond laser irradiation with different energy. a: without irradiation; b: 1.0 μJ ; c: 2.5 μJ [Peng, 2009]. (b) The emission spectra of Bi doped glasses with and without femtosecond laser irradiation [Zhou, 2009]. (c) NIR emission spectra of the γ -irradiated α -BBO:Bi crystal upon 808 nm and 980 nm excitation, respectively. The inset is the decay curve of the 1139 nm emission [Su, 2009].....	20
Figure 1.9 (a) Absorption and luminescence cross section spectra of a Bi-doped aluminosilicate fibre [Haruna, 2005]. (b) A summary scheme of the	



main emission peaks for different fibers. The types of fibers and lifetime values for various luminescence bands are also indicated [Dianov, 2012]. (c) The 1460 nm Bi-doped fiber laser. HR, high reflectivity fiber Bragg grating; OC, output coupler. [Firstov, 2011] (d) A Bi-doped fiber amplifier. ISO, optical isolator; WDM, wavelength division multiplexing coupler; OSA, optical spectrum analyzer; FC APC connector, Fiber-optics connector for Angled Physical Contact [Melkumov, 2011].....24

Figure 1.10 (a) Cross-sectional HRTEM image of the annealed superlattices. (b) NIR PL spectra of the annealed glass film (G) and superlattices (S) under the excitation of 325 and 405 nm. (c) The normalized NIR PL spectra of the samples G and S under the excitation. [Sun, 2010]...29

Figure 2.1. Flow diagram of the ceramics's preparation procedure.36

Figure 2.2. Schematic view of a typical PLD system [Kramer, 2003].37

Figure 2.3 (a) Schematic of a typical SEM. (b) The schematic diagram of interactions between electron beam and a sample [Claudionico, 2013].40

Figure 2.4 Simplified Jablonski diagram illustrating Rayleigh, Stokes, and anti-Stokes Raman scattering.43



Figure 2.5 Photograph of LabRAM HR 800 Raman spectrometer in our laboratory.	44
Figure 2.6 Photography of Edinburgh FLSP920 spectrometer used in our laboratory.	46
Figure 2.7 Schematic diagram of Edinburgh FLSP920 spectrometer.....	47
Figure 2.8 Sample of fluorescence decay curve [Zhang, 2012].....	49
Figure 2.9 Experimental setup of typical <i>P-E</i> loop measurement [Wu, 2014]..	51
Figure 3.1 (a) XRD patterns of Ni ²⁺ -doped BST- <i>x</i> samples in the 2θ scan range of 10 to 80 °. (b) 2θ diffraction peaks around 32 ° for the Ni ²⁺ -doped BST- <i>x</i> samples. (c) 2θ diffraction peaks around 46 ° for the Ni ²⁺ -doped BST- <i>x</i> samples.....	59
Figure 3.2 Polarization hysteresis loop of Ni ²⁺ -doped BST- <i>x</i> , measured at room temperature.....	60
Figure 3.3 (a) PL and (b) normalized PL spectra of Ni ²⁺ -doped BST samples when pumped at 360 nm.	61
Figure 3.4 (a) PLE spectra of Ni ²⁺ -doped BST- <i>x</i> samples. (b) PL spectra of Ni ²⁺ -doped BST- <i>x</i> samples when pumped at 980 nm.....	62



Figure 3.5 PLE spectrum of Ni ²⁺ -doped STO and PL spectrum of Ni ²⁺ -doped STO when pumped at 808 nm.....	64
Figure 3.6 (a) PL decay curves of Ni ²⁺ -doped BST samples. (b) Peak position and lifetime of NIR PL from Ni ²⁺ -doped BST.....	66
Figure 3.7 Crystal structures of perovskite BST. With the increase of barium atoms, the crystal parameter gradually expands.	67
Figure 3.8 (a) XRD pattern of Ni ²⁺ -doped BST powder in the 2θ scan range of 20 to 80°. (b) Temperature dependent dielectric constant of Ni ²⁺ -doped BST disc.	74
Figure 3.9 (a) Temperature dependent PLE spectra of Ni ²⁺ -doped BST disc, λ _{em} =1350 nm. (b) Energy levels and transitions of Ni ²⁺ in octahedral sites.....	75
Figure 3.10 Temperature dependent PL spectra of Ni ²⁺ -doped BST disc, λ _{ex} =350 nm.	76
Figure 3.11 PL intensity and peak position of Ni ²⁺ -doped BST disc as a function of temperature changed from 100 K to 300 K.	76
Figure 3.12 Phase transition of Ni ²⁺ -doped BST.	77
Figure 3.13 PL decay curves of Ni ²⁺ -doped BST disc at different temperature,	



$\lambda_{ex}=350$ nm and $\lambda_{em}= 1350$ nm.	79
Figure 3.14 (a) XRD pattern of Ni ²⁺ -doped BST(1200 nm)/LAO sample. (b) PL spectrum of Ni ²⁺ -doped BST(1200 nm)/LAO sample.	81
Figure 3.15 Photographs of STO bulk target (Left), Ni ²⁺ -doped STO thin films grown on LAO and Pt-Si wafer (Right).	86
Figure 3.16 Normalized PL spectra of Ni ²⁺ -doped BST- <i>x</i> thin films grown on Pt-Si wafer, $\lambda_{ex}=325$ nm.	86
Figure 3.17 PLE spectra of Ni ²⁺ -doped BST- <i>x</i> thin films grown on Pt-Si wafer.	87
Figure 3.18 Decay curves of Ni ²⁺ -doped BST- <i>x</i> thin films.	89
Figure 3.19 Raman spectra of Ni ²⁺ -doped BST- <i>x</i> thin films.	90
Figure 3.20 XRD pattern of Ni ²⁺ -doped STO grown on LAO in the 2θ scan range of 20 to 80 °.	91
Figure 3.21 PL spectra of Ni ²⁺ -doped STO thin films grown on different substrates, $\lambda_{ex}=325$ nm.	91
Figure 4.1 (a) Schematic of strained thin film of STO:Ni grown on PMN-PT. (b) The setup used for measuring the NIR emission of STO:Ni/PMN-PT	



under an external electric field.....	96
Figure 4.2 NIR PL spectra of STO:Ni thin films with different thickness (t) and ceramic bulk under 325 nm excitation.	99
Figure 4.3 The PLE spectra of the STO:Ni samples.....	100
Figure 4.4 The normalized NIR PL decay curves of the STO:Ni samples.....	101
Figure 4.5 Configurational coordinate diagrams for STO:Ni samples. The lowest electronic states $^3A_{2g}$ are shown; Horizontal lines represent vibrational energy levels. The upward and downward arrows indicate absorption and emission transitions, respectively. R is the distance between Ni^{2+} ions and ligands. E_{dis} represents the difference between the excited state vibrational level reached in the absorption transition and the minimum level of the same state.....	104
Figure 4.6 The SEM image of ITO/STO:Ni (600 nm)/PMN-PT.....	105
Figure 4.7 The PL spectra of STO:Ni (600 nm)/PMN-PT under 325 nm excitation, when DC bias voltage is applied from 0 to 500 V.	106
Figure 4.8 The summarized PL results of STO:Ni (600 nm)/PMN-PT.....	107
Figure 4.9 The NIR PL decay curves of STO:Ni (600 nm)/PMN-PT.....	107



- Figure 4.10 XRD patterns of STO:Ni (600 nm)/PMN-PT under DC bias voltage ranging from 0 to 500 V..... 108
- Figure 4.11 Schematic of the compressive STO:Ni thin film biaxially strained to match the substrate PMN-PT. 109
- Figure 4.12 The PL emission peak position of STO:Ni (600 nm)/PMN-PT as a function of the applied voltage from -500 V to 500 V..... 111
- Figure 5.1 XRD pattern of Bi-doped germanate film deposited under 1.0 Pa. The inset is SEM plan view of the film. 117
- Figure 5.2 PL and PLE spectra of Bi-doped germanate films deposited under different P_{O_2} measured by InGaAs detector. (a) The inset is the P_{O_2} dependent emission peak position change. (b) The monitored emission wavelength is at 1500, 1370 and 1240 nm, respectively. The inset is the fluorescence decay curves of the Bi-doped germanate films..... 118
- Figure 5.3 (a) PL and (b) PLE spectra of Bi-doped germanate film deposited under 1.0 Pa..... 119
- Figure 5.4 XPS spectra of Bi-doped glass and films deposited under different P_{O_2} . Solid lines represent measured curves, the dashed lines fit the



Lorentzian-Gaussian curves.....	121
Figure 5.5 PL spectra of germanate films deposited under 1.0 Pa. The luminescence in (a) and (b) is measured by InSb and InGaAs detectors, respectively. The inset in (b) is the fluorescence decay curve of Bi/Ho co-doped germanate film monitored at 1500 nm. .	122
Figure 5.6 Raman spectra of Bi-doped, Bi/Ho co-doped germanate glasses and films.	126
Figure 5.7 Absorption spectra of Bi-doped and Bi/Ho co-doped germanate glasses.	127
Figure 5.8 Energy level scheme and energy transfer process between Bi cluster and Ho^{3+}	128
Figure 5.9 PL spectra of Bi-doped phosphate film deposited under 1.0 Pa and the glass target.....	130
Figure 5.10 PLE spectra of Bi-doped phosphate film deposited under 1.0 Pa and the glass target.....	130
Figure 5.11 The fluorescence decay curves of Bi-doped phosphate film and the glass target.....	131



List of Tables

Table 3.1 Comparison of NIR PL from Ni²⁺-doped materials.....65

Table 4.1 PL comparison of STO:Ni on PMN-PT and the ceramic bulk.....102



List of Symbols

Symbol	Description
a, b, c, β	lattice parameters
d_{33}	piezoelectric constant
ε	relative permittivity
T_c	Curie temperature
E	electric field
E_c	electrical coercive field
P_r	remnant polarization
λ_{ex}	excitation wavelength
λ_{em}	emission wavelength
τ	luminescence lifetime
d_{hkl}	interplanar spacing of the {hkl} set of lattice planes
θ_{hkl}	incident angle of the beam



List of Acronyms

Acronyms	Description
BTO	Barium titanate, BaTiO ₃
BST- <i>x</i>	Barium strontium titanate, Ba _{<i>x</i>} Sr _{1-<i>x</i>} TiO ₃
BST	Ba _{0.5} Sr _{0.5} TiO ₃
ET	energy transfer
FWHM	Full width at half maximum
NIR	Near-infrared
<i>P-E</i> loop	polarization-electric field hysteresis loop
PL	photoluminescence
PLE	photoluminescence excitation
PLD	Pulsed laser deposition
STO	Strontium titanate, SrTiO ₃
SEM	scanning electron microscope
XRD	X-ray diffractions

Chapter 1 Introduction

1.1 Background of NIR luminescence

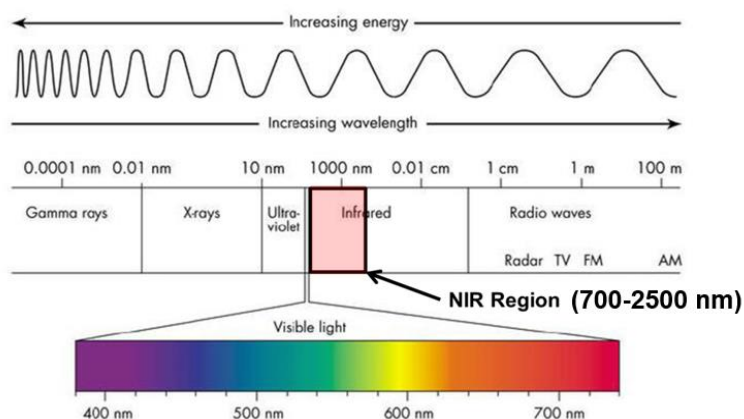


Figure 1.1 Electromagnetic spectrum with NIR light highlighted. [Harvey, 2015]

Near-infrared (NIR) is invisible to humans, electromagnetic radiation with lower energy than that of visible light, ranging from the nominal red edge of the visible spectrum at 700 nm (frequency 430 THz) to 2500 nm (120 GHz) (Figure 1.1) [Blasse, 1994; Xiang, 2013]. In recent decades, NIR light has been widely used in industrial, scientific, and medical communities [Bünzli, 2010]. Meanwhile, the ever-increasing demand in optical telecommunication, biomedicine, energy, and many other applications has raised expanding requirement for NIR luminescence materials [Bünzli, 2010; Chen, 2012; Eliseeva, 2010].

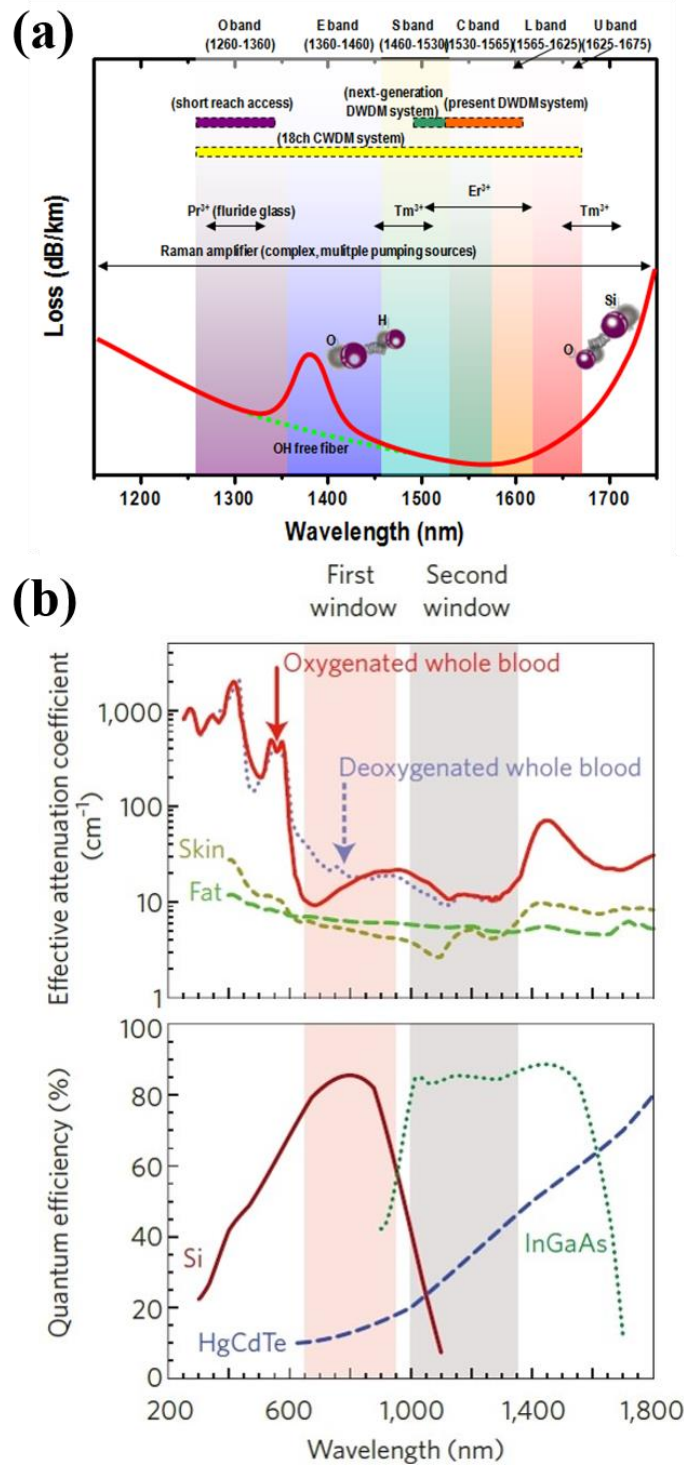


Figure 1.2 (a) The loss spectra of fiber & various kinds of rare-earth (RE) doped amplifiers. (b) Optical windows in biological tissues [Smith, 2009].



Optic fiber communications systems depend on the low-loss propagation of NIR optical signals inside pure silica glass fibers, as shown in Figure 1.2 (a) [Bagad, 2009]. The extended telecommunications wavelength band covers 1200-1700 nm. From 1989, the modern optical telecommunication networks have been greatly stimulated by the Wavelength Division Multiplexing (WDM) technique. The WDM system based on Er^{3+} -doped fiber amplifier (EDFA) can provide higher transmission speed and capacity (Figure 1.2 (a)) [Hagimoto, 1989; Nakazawa, 1989]. Due to the rapid development of the internet industry and other data-transmitting services, optical communication networks demands broadband amplifiers with broader gain bandwidth and higher optical gain. Therefore, it is necessary to investigate and develop novel broadband amplifiers, including fiber and planar waveguide amplifiers [Bünzli, 2010].

NIR optical imaging of living tissue attracts increasing interest from biomedicine areas. Using visible luminescence probes, multicolored and sensitive fluorescence imaging of cancer cells has been demonstrated in the traditional visible spectral region (400-700 nm) [Sargent, 2005]. However, deep organs such as the spleen and liver could not be detected with visible tags in mice due to the limited penetration depth of visible light [Wang, 2004]. Absorption and scattering of photons induced by water and hemoglobin are the major reasons for the attenuation of signal proportional to tissue depth. As shown in Figure 1.2 (b), to tackle this problem, biological transparency windows: the NIR I window (650-900 nm) and



NIR II window (1000-1450 nm) have been developed for bioimaging [Won, 2012]. In fact, NIR I window is not optimal because tissue autofluorescence produces substantial background noises and tissue penetration depth is still limited to 1-2 cm. In 2003, simulations and modelling studies of optical imaging in turbid media such as tissue or blood suggested that it would be possible to improve signal-to-noise ratios by over 100-fold by using quantum dot fluorophores that emit light within NIR II window [Smith, 2009]. However, the lack of luminescent material emitting in NIR II window has prevented the use of this highly sensitive spectral range for in vivo imaging.

Sunlight is an abundant source of energy on Earth, which can be captured by new technologies and transformed into electricity. It is expected that the use of solar energy can meet a large portion of future energy consumption requirements. A major problem limiting the conversion efficiency of photovoltaic cells is their insensitivity to a full solar spectrum. Current photovoltaic cells only utilize a relatively small fraction of the solar photons. This is ascribed to the fact that each photovoltaic material responds to a narrow spectral range of solar emission photons with energy matching the characteristic bandgap of the semiconductors [Chen, 2012]. It is notable that nearly 50 % of the energy from the Sun reaching the Earth is in the form of NIR radiation [Xiang, 2013]. Thus it is important to extend the radiation absorption of photovoltaic devices from the ultra violet/visible into the NIR region.

1.2 Metal ions-doped photonic materials with NIR



luminescence

One large group of commonly used luminescent material is so-called metal-ion doped phosphors. To date, numerous kinds of metal-ion doped phosphors have been fabricated in different forms such as glasses, crystals, powders, nanoparticles, and thin films, in which the luminescent properties mainly depend on the energy transition of activators in the phosphors [Bai, 2015]. The luminescence of metal-ion doped phosphors can cover broad optical spectra, including NIR spectral regions. These metal ion-doped phosphors have drawn great attention due to their widespread applications from optoelectronics to biomedicines, through to approximately every aspect of human life [Tsang, 2015]. Generally, three types of metal ions are mostly served as impurities in NIR spectral regions, including lanthanide ions, transition metal ions, and main group metal ions. As shown in Figure 1.2 (a), considerable efforts have been made to broaden and flatten the gain spectra of currently used rare-earth doped fiber amplifiers (e.g., Er-, Pr-, or Tm-doped amplifiers) [Belancon, 2014; Li, 2011], specifically Er-doped amplifiers [Giles, 1991], in order to meet the great demands of the continued growth of information traffic in telecommunication networks. However, limited by the intrinsic narrow f - f transitions among the $4f$ orbits of rare-earth ions confined in the inner-shell (Figure 1.3), the emitting bandwidth of rare-earth ions activated amplifiers is usually less than 100 nm, which is relatively independent of the host matrices [Feng, 2013; Liu, 2013].

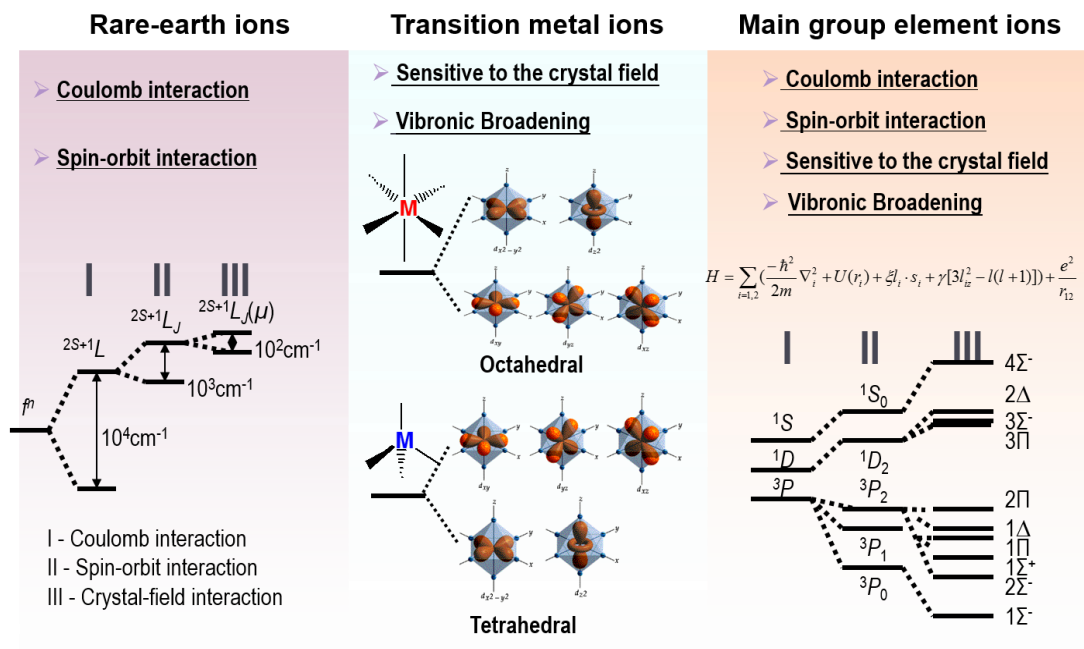


Figure 1.3 Typical energy level diagrams of metal ions with NIR emission.

In order to broaden the bandwidth of the photonic materials, the principle of vibronic broadening is introduced, namely that the electronic transitions involve the simultaneous absorption or emission of both photons and phonons. Since the transitions among d orbitals of ions are very sensitive to matrixes [Kuleshov, 1997], the luminescence is expected to be strongly related to electronic transitions with simultaneous vibrational excitations of the lattice rather than purely electronic lines observed in most of rare-earth ions [Brik, 2006]. It has been reported that 3d transition metals ions such as Ni^{2+} , Cr^{4+} , and Co^{2+} can be doped into inorganic matrices as activators to achieve broadband NIR photoluminescence [Brik, 2006]. However, for Cr^{4+} and Co^{2+} , it is difficult to stabilize the specific valence and



suitable coordination states. Therefore, Ni^{2+} seems to be the most promising choice which can serve as a broadband NIR activator [Gao, 2012]. In fact, various types of Ni^{2+} doped NIR photonic materials, such as glass ceramics and crystals, have been developed due to their potential applications in tunable lasers and broadband optical amplifiers.

Apart from lanthanide ions and transition metal ions, main group metal ions, including $6p$ (Bi, Pb) and $5p$ (Sb, Sn, In, Te), are also promising as a new type of active ions, due to broadband NIR luminescence of main group metal ions doped materials [Xu, 2011.]. In particular, bismuth (Bi)-doped glasses and thin films have drawn much attention due to their ultrabroadband NIR luminescence in the wavelength region from 1000 to 1700 nm with the full-width at half maximum of (FWHM) over 300 nm, which covers the entire windows of optical fiber communications [Qiu, 2008]. They possess long emitting lifetime of several hundred microseconds. It is expected that Bi-doped NIR luminescent glasses can serve as novel ultrabroadband NIR optical fiber gain and laser media.



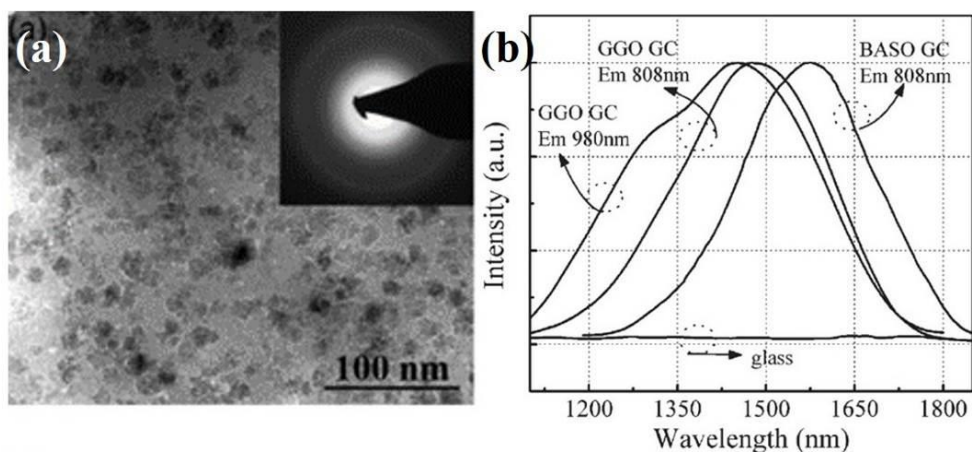
[Kück, 2001]. (c) The absorption spectrum of a MgGa₂O₄:Ni crystal at room temperature [Suzuki, 2010].

Recently, the reported Ni²⁺ doped NIR photonic materials include bulk materials, glass fibers, and these forms of materials show the broadband emission, covering the entire optical fiber communication window [Mironova-Ulmane, 2013; Sigaev, 2012]. In general, Ni²⁺ ions can present three different coordination states in an inorganic matrix, namely tetrahedral (fourfold, ^{IV}Ni²⁺), trigonal (fivefold, ^VNi²⁺) and octahedral (sixfold, ^{VI}Ni²⁺). Only ^{VI}Ni²⁺ has been demonstrated to provide efficient NIR emission [Dugue, 2012; Zannoni, 1999]. Meanwhile, the electron configuration of transition metal Ni²⁺ ion is 3d⁸4s⁰, therefore the emissions due to the transitions among *d* orbitals of Ni²⁺ ion is more sensitive to matrixes compared to the previously studied rare-earth doped photonic materials. Hence, ultrabroadband emission corresponding to Ni²⁺ electron transition could be tuned through controlling the nature of the transition metal-ligand interaction.

1.3.1.1 Ni-doped bulk photonic materials

Previous reports on Ni-doped NIR photonic materials are focused on crystals, such as Ni-doped MgF₂, KMgF₃, MgO, CaY₂Mg₂Ge₃O₁₂ (GGG), etc. As shown in Figure 1.4 (a), all the luminescent crystals present ultrabroadband NIR emission [Kück, 2001]. Notably, with the different crystal hosts, the Ni²⁺ emission center can shift from 1100 nm to 1700 nm. In octahedral coordination, Ni²⁺ energy-level

scheme is described by the Tanabe-Sugano diagram presented in Figure 1.4 (b). The tunable ultrabroadband NIR emission originates from spin-allowed transition ${}^VI\text{Ni}^{2+}$: ${}^3\text{T}_2({}^3\text{F}) \rightarrow {}^3\text{A}_2({}^3\text{F})$. The Ni^{2+} energy configuration can be derived from the crystal-field strength Dq and Racah parameter B [Brik, 2012]. Therefore, diverse crystal-field strengths Dq and Racah parameters B in different matrixes leads to the tunable NIR emission. Figure 1.4 (c) displays a typical absorption spectrum of Ni-doped NIR single crystal MgGa_2O_4 [Suzuki, 2010]. The Ni-doped crystal exhibits broad absorption bands in both visible and infrared areas. Three bands corresponding to the spin-allowed transitions from the ${}^3\text{A}_2({}^3\text{F})$ ground state to the ${}^3\text{T}_2({}^3\text{F})$, ${}^3\text{T}_1({}^3\text{F})$, and ${}^3\text{T}_1({}^3\text{P})$ excited states are detected.



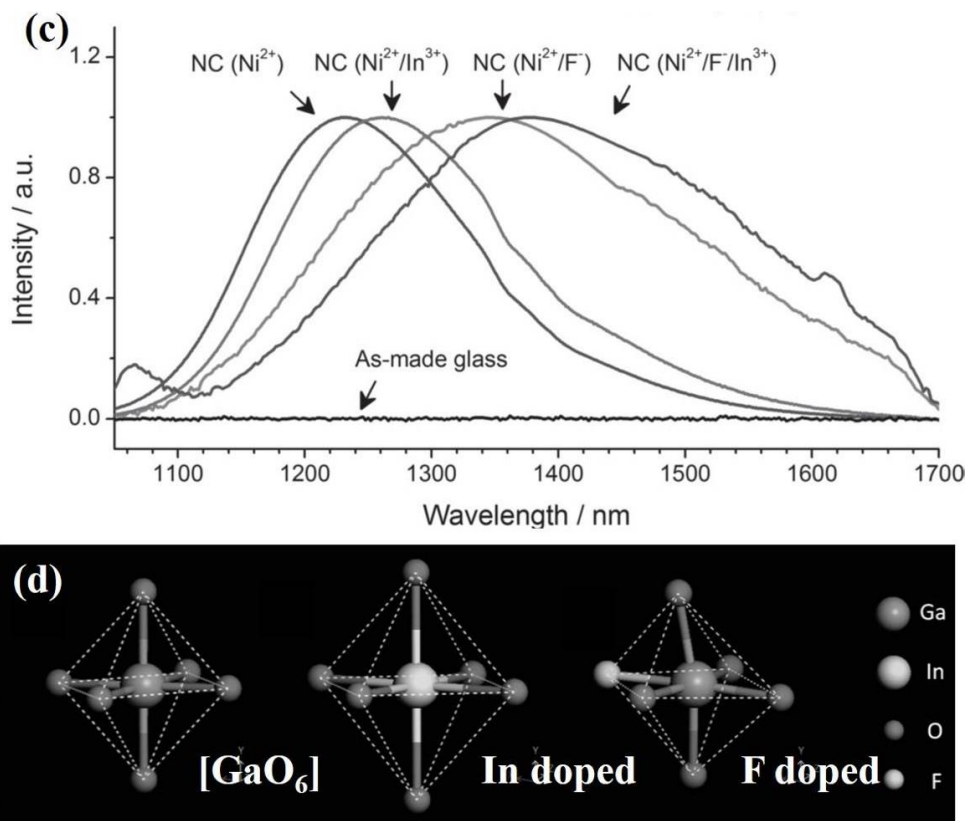


Figure 1.5 (a) Bright-field TEM image of GGO glass ceramics. The insets show the corresponding Selected-area electron diffraction patterns. (b) NIR luminescence spectra of GGO and BASO glass and glass ceramics samples under excitation with 808 and 980 nm lasers. [Zhou, 2009] (c) NIR emission spectra of glass ceramics containing nanocrystals $\text{Ga}_2\text{O}_3:\text{Ni}^{2+}$ with doping In^{3+} and F^- . (d) Configurations of regular $[\text{GaO}_6]$ octahedron, with dopant In^{3+} and F^- [Zhou, 2013].

For decades, glass ceramics embedded with nanocrystals have been demonstrated as a kind of promising photonic materials for applications in luminescence devices,



tunable solid state lasers and optical amplifiers [Bai, 2013; Teng, 2012]. Glass ceramics share some advantages with both glasses and ceramics [Bai, 2013]. Ni-doped glass ceramics with stable valence state and ultrabroadband NIR emission have attracted great attention for their potential applications in broadband optical amplifiers [Gao, 2012; Wu, 2013]. Particularly, a series of Ni-doped glass ceramics have been developed [Zhou, 2011], and the optical properties of Ni-doped glass ceramics could be tailored by tuning nanocrystal size [Zhou, 2008]. Control of the local ligand field around Ni^{2+} and co-doped with other active ions (e.g. Cr^{3+} , Yb^{3+} , Bi ions) have been reported [Wu, 2008; Wu, 2009; Zhang, 2012]. An interesting example regarding the tailoring of the local ligand field around Ni^{2+} has achieved tunable ultrabroadband NIR emission [Zhou, 2009]. In the experiment, two glass samples with compositions of $80\text{GeO}_2\text{-}12\text{Ga}_2\text{O}_3\text{-}8\text{Na}_2\text{O}\text{-}0.1\text{NiO}$ (mol %) (GGO) and $45\text{SiO}_2\text{-}15\text{Al}_2\text{O}_3\text{-}12\text{Na}_2\text{O}\text{-}13\text{BaF}_2\text{-}12\text{MgO}\text{-}3\text{ZrO}_2\text{-}0.1\text{NiO}$ (mol %) (BASO) were fabricated by the melt-quenching method. After heat treatment ($720\text{ }^\circ\text{C}$ for GGO and $680\text{ }^\circ\text{C}$ for BASO) for 2 h, the $(\text{Ga}_2\text{O}_3)_3(\text{GeO}_2)_2$ [JCPDS (50-0354)] and $\text{Ba}_{0.808}(\text{Al}_{1.71}\text{Si}_{2.29})\text{O}_8$ [JCPDS (88-1050)] were precipitated successfully as verified by the X-ray diffraction (XRD) patterns and transmission electron microscopy (TEM) images (as shown in Figure 1.5 (a)). Figure 1.5 (b) presents the NIR emission spectra of the GGO and BASO glass and glass ceramics. The luminescence peaks display obvious red shifted from high energy (1300 nm) to low energy (1450 nm) bands in GGO glass ceramics and even to 1570 nm for BASO glass ceramics, indicating the effective tuning of luminescence properties to the extent that the luminescence



covered almost the whole NIR region. In particular, GGO glass ceramics present a significant ultrabroadband NIR luminescence characteristic with FWHM of about 400 nm under the excitation of a 980 nm laser, which can cover the optical telecommunication bands at 1200-1600 nm. By contrast, Ni-doped as-prepared glass samples show no emission in this region. The tunable and ultrabroadband luminescence can be understood from the absorption spectra and Tanabe-Sugano diagram. The fluctuation of crystal field strength may shift the vertical positions of the energy levels, leading to a variation of the energy gap between the ${}^3T_2(F)$ and ${}^3A_2(F)$ levels. Therefore, the tunable luminescence is achieved by the fine-tuning crystal field strength of Ni^{2+} ions. Then, through introduction of various cation/anion impurities (e.g., F^- and In^{3+}), exceptional tunable NIR emission from glass ceramics containing nanocrystals $Ga_2O_3:Ni^{2+}$ have been achieved (see Figure 1.5 (c)). As shown in Figure 1.5 (d), with doping impurities in the nanocrystals, the distortion of local structure may induce formation of mixed Ni^{2+} environments with different Dq . Consequently, the fluctuation of crystal field strength results in tunable transition emission.

1.3.1.2 Ni-doped fiber photonic materials

Nowadays, optical fiber is widely used as a medium for telecommunication and an active gain medium for fiber laser. Samson *et al.* in Corning Inc. developed Ni-doped nanocrystalline glass ceramics fiber [Samson, 2002]. They prepared the base glass with the composition $SiO_2-Ga_2O_3-Al_2O_3-K_2O-Na_2O-Li_2O$. And then the heat-



treated glass ceramic fiber was fabricated by a rod-in-tube technique. As shown in Figure 1.6 (a), the photoluminescence spectra are depended on the heat treatment given the fiber. The optimized spectrum has about 250 nm FWHM peaking at around 1200 nm, and the spectrum obviously changes from several sharp peaks at longer wavelength to a smooth more Gaussian line shape as the cerammed temperature increases. After the optimum ceramming process, the lifetime and fluorecence efficiency for the active Ni²⁺ ions have been dramatically improved. The effective lifetime τ is recorded as 1.1 ms. The radiative quantum efficiency for Ni-doped gallate spinel nanocrystals in these fibers even reaches ~70 % at low pump powers. Figure 1.6 (b) presents the outputs of combined Ni and Tm doped fibers, pumped with a single Yb fiber laser at 1060 nm. The combined output of the all fiber device exceeds 450 nm at 5 dB bandwidth. Through modulation of the pump power ratio provided to each active fiber, the output spectrum can be readily optimized. More importantly, such fiber based broadband sources have applications in future optical coherence tomography and commercial optical coherence domain reflectometer systems.

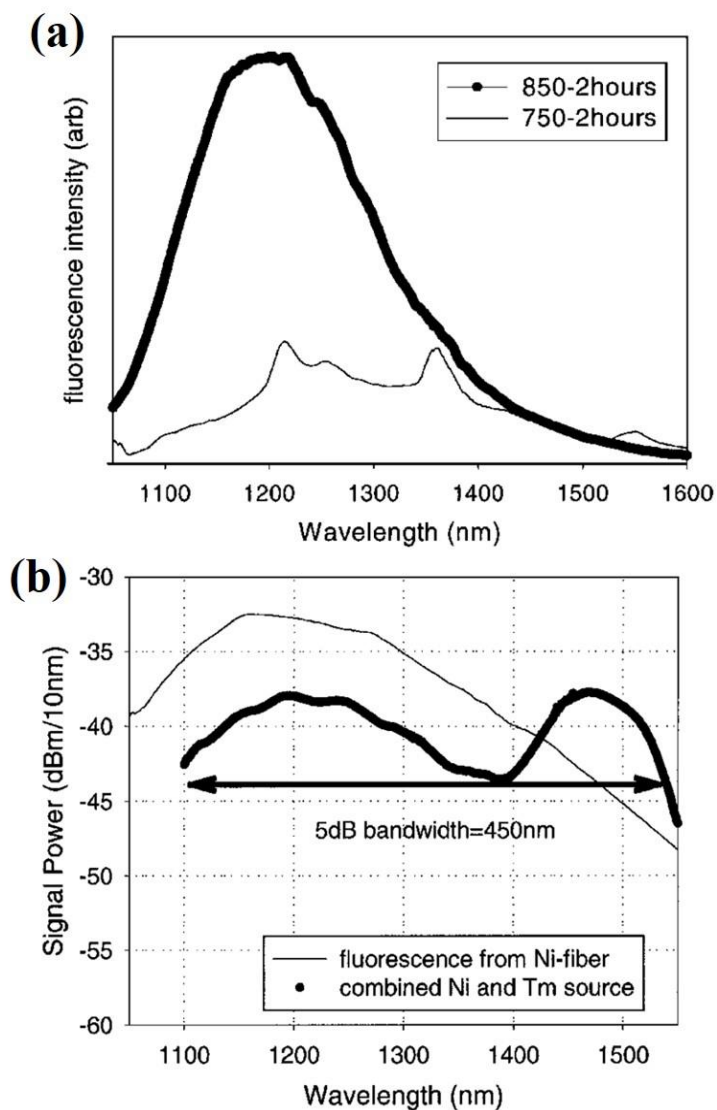


Figure 1.6 (a) Fluorescence spectra from Ni-doped optical fibers with diverse heat treatment. (b) Combined Ni- and Tm-doped optical fiber source pumped at 1060 nm. [Samson, 2002].

1.3.2 Bi-doped photonic materials with NIR luminescence

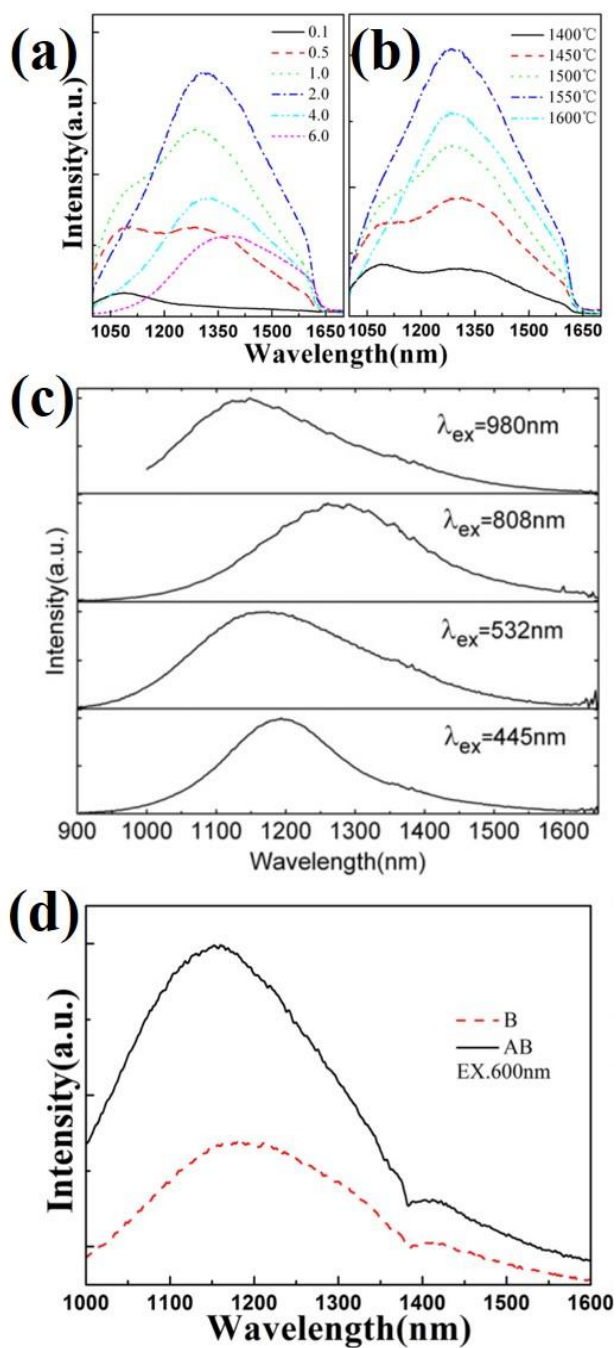


Figure 1.7 (a) NIR PL spectra of Bi-doped germanate glasses with various bismuth



concentrations melted in air at 1500 °C, under 880 nm excitation. (b) NIR PL spectra of 1.0 mol. % Bi-doped glasses melted in air at various temperatures. All the spectra are excited by 880 nm. [Xu, 2013] (c) Fluorescence spectra of Bi-doped phosphate glass excited by different lasers [Wang, 2012]. (d) NIR PL spectra of glasses B and AB excited by 600 nm [Xu, 2013].

Bi, of atomic number 83 and the electronic configuration $(\text{Xe})4f^{14}5d^{10}6s^26p^3$, is one of the most systematically studied main group elements, whose outer 6s and 6p electrons are valence electrons. Due to the outer valence electrons, Bi element possesses multiple oxidation states including 0, +1, +2, +3, and +5 [Peng, 2011; Yang, 2011]. One of the most significant characteristics of these ions, particularly for Bi^+ , Bi^{2+} , and Bi^{3+} , is their luminescence in NIR region under ultraviolet, visible or NIR light excitation, originating from their multiplex electronic structures [Xu, 2014; Zhou, 2008]. Compared with the traditional active centers such as lanthanide and transition metal ions, Bi-activated photonic materials present abundant luminescence characteristics [Romanov, 2011]. The photoluminescence of Bi-doped photonic materials are of great interest from scientific aspect, with the simultaneous development of novel materials with modulated attributes [Guo, 2011; Song, 2012; Sun, 2014]. In general, the absorption and emission bands of Bi ions are much broader than those of $f-f$ transitions of rare earth ions, due to the unsheltered outer electrons. This provides plenty of opportunities for further tailoring the spectroscopic features of Bi through rational selection of host materials, facile control of



preparation processes under suitable conditions [Bai, 2012; Dai, 2012; Yang, 2011]. To date, research activities have been gradually disclosed toward distinct purposes ranging from fundamental features of the Bi spectroscopy (e.g., controlling Bi valence states and explaining the related emission mechanism) to the materials include bulk glasses [Dai, 2012; Ruan, 2009; Zhou, 2009], crystalline materials [Ruan, 2009; Romanov, 2013], and molecular crystals [Sun, 2009; Sun, 2012]. For diverse host materials or synthesis process, Bi active centers present different NIR broadband luminescence. It is beneficial for controlling and processing light for active components of light sources, optical waveguides, and biomedicine. Hence, tunable luminescence Bi-doped photonic materials can be realized by the control of chemical compositions and preparation processes [Dai, 2012; Song, 2011]. For example, Bi-doped germanate glass samples with the compositions of $20\text{MgO}-5\text{Al}_2\text{O}_3-75\text{GeO}_2-x\text{Bi}_2\text{O}_3$ ($x=0.1-6.0$ mol %) were prepared by the melt-quenching method [Xu, 2013]. Tunable luminescence in the same host material with single dopant is achieved through modulating doping level, preparation temperature, and atmosphere. As shown in Figure 1.7 (a), only one peak around 1080 nm is detected for 0.1 mol % Bi-doped glass. When the doping concentration is raised up to 0.5 mol %, this peak red shifts to 1090 nm and another peak centered 1290 nm; moreover, FWHM of the NIR emission exceeds 500 nm showing overwhelming better than rare-earth doped materials for optical communication. As Bi content increases to 1.0 mol %, the emission peak presents a red shift to 1100 nm and a dominant peak at 1300 nm appears. With further increasing Bi content, the peak



around 1100 nm diminishes at last, while the peak around 1300 nm red-shifts to 1375 nm and becomes the main peak. In Figure 1.7 (b), when 1.0 mol % Bi-doped glass is melted at temperatures from 1400 to 1600 °C in air, the emission wavelength and relative intensity can also be modified. At 1400 °C, the emission intensity of the peaks around 1100 nm is relative strong. In contrast, the emission intensity around 1300 nm is stronger than that around 1100 nm at 1450 °C. Further rising the melting temperatures results in the dominant peak around 1300 nm and the increase of the intensity of both peaks reaching the maximum at 1550 °C. And then, the intensity of both peaks decreases at 1600 °C. The tunable luminescence is ascribed to the Bi species transformation. Zhang et al. fabricated Bi-doped phosphate glass, with FWHM of 312 nm and lifetime of 580 μ s [Wang, 2012]. As presented in Figure 1.7 (c), the NIR emission peaks vary from 1148 nm to 1260 nm under different pumping sources. Through codoping with Ag, enhanced broadband NIR luminescence has been observed in Bi-doped oxyfluoride glasses [Xu, 2013]. As shown in Figure 1.7 (d), compared with glass B (Bi-doped oxyfluoride glass), glass AB with Ag presents improved NIR emission, and the peak position shows a blue shift. The enhanced mechanism is considered depth combing the energy transfer from Ag^+ , molecular-like, nonplasmonic Ag species, Bi^{2+} and Bi^{3+} to NIR Bi active centers, and the redox reaction of Bi species with Ag species.

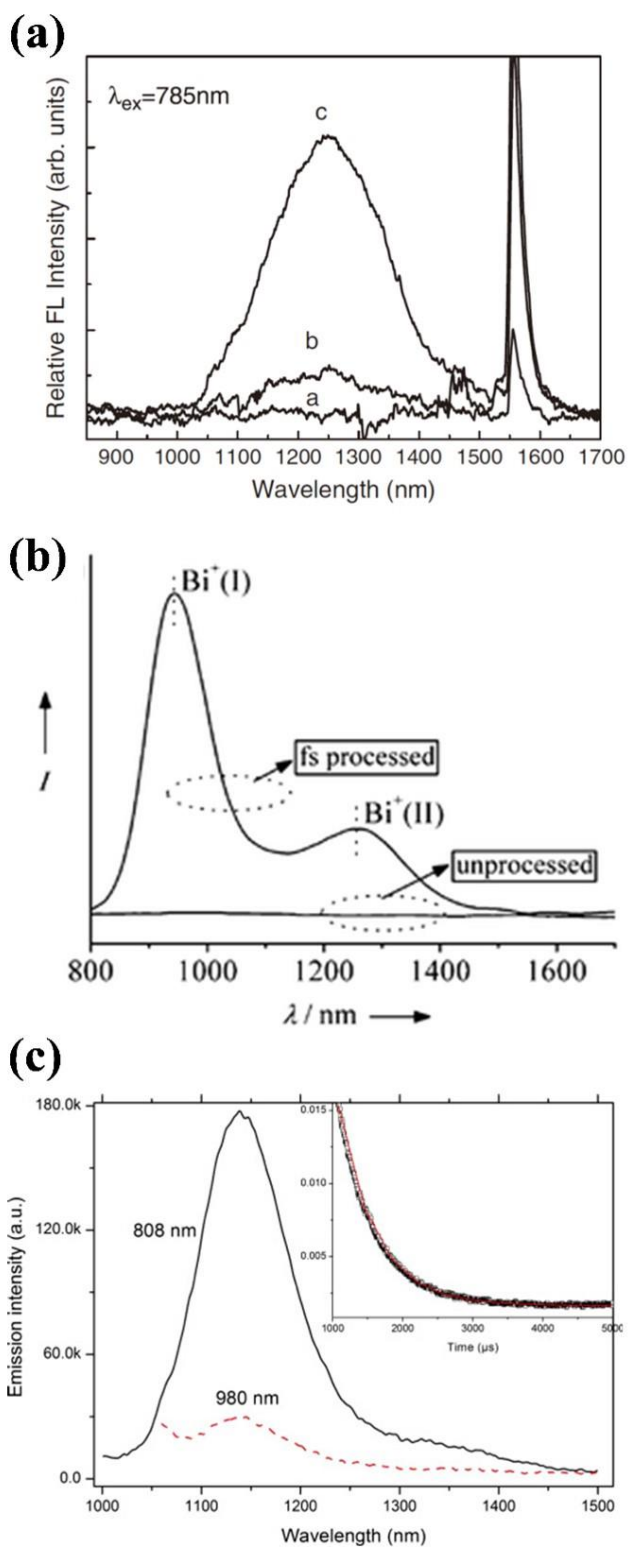


Figure 1.8 (a) The emission spectra of Bi doped glasses under femtosecond laser



irradiation with different energy. a: without irradiation; b: 1.0 μJ ; c: 2.5 μJ [Peng, 2009]; (b) The emission spectra of Bi doped glasses with and without femtosecond laser irradiation [Zhou, 2009]; (c) NIR emission spectra of the γ -irradiated α -BBO:Bi crystal upon 808 nm and 980 nm excitation, respectively. The inset is the decay curve of the 1139 nm emission [Su, 2009].

In addition, the luminescence of Bi-doped photonic materials can be modified by selected physical approaches, such as photon-assisted ionizing radiation [Bai, 2014]. For instance, absorption and emission spectra of Bi-doped glasses have been tuned via femtosecond laser irradiation [Peng, 2009; Usovich, 2012]. Through conventional melting and quenching method, bismuthate glass with composition $52\text{Bi}_2\text{O}_3\text{-}23\text{B}_2\text{O}_3\text{-}4\text{SiO}_2\text{-}17\text{PbO}\text{-}4\text{Sb}_2\text{O}_3$ (wt. %) were prepared. The prepared glass presented almost no absorption band in visible and NIR spectral ranges, and no NIR luminescence under 785 nm excitation. After femtosecond laser irradiation, a strong absorption band appeared at around 500 nm, and peak intensity increased as the laser pulse energy was increased from 1.0 to 2.5 μJ . Accordingly, broadband NIR emission peak arised, and the intensity was dramatically enhanced as increasing laser pulse energy (Figure 1.8 (a)). It is deduced that the observed change is resulted from fast photon-induced reduction of Bi^{3+} ions to Bi^+ ions. Under sufficiently high intensity laser irradiation, multiple photons are simultaneously absorbed by electrons that allow them to transfer from valence to conduction band. With increasing the pulse energy, the number of electrons increases and thereby the probability of



permanent reduction gets enhanced, leading to the increase in concentration of Bi^+ ions, and enhancement in NIR emission intensity. More interestingly, the focused ultrashort laser pulse was employed to induce multiple active centers of bismuth in the mesoporous silica glass [Zhou, 2009]. Through porous glasses soaked in solution of $\text{Bi}(\text{NO}_3)_3$, Bi^{3+} doped mesoporous glasses were fabricated, which was confirmed by typical blue emission from $^3\text{P}_1 \rightarrow ^1\text{S}_0$ transition of Bi^{3+} ions. After femtosecond laser irradiation, the processed area shows intense red emission which is visible by the naked eyes. The red emission can be attributed to the $^2\text{P}_{3/2} \rightarrow ^2\text{P}_{1/2}$ transition of Bi^{2+} ions, differing from the blue emission in the unprocessed area, indicating the fast photon-induced reduction from Bi^{3+} ions to Bi^{2+} ions. With an 808 nm laser diode as pump source, broadband NIR emission with two obvious bands around 950 and 1235 nm is resulted (Figure 1.8 (b)). The NIR luminescence is associated with the $^3\text{P}_1 \rightarrow ^3\text{P}_0$ transition of Bi^+ emission centers. In contrast, there is no NIR emission in the unprocessed area. Based on the observed emission spectra, some of Bi^{3+} ions should be photoreduced to the lower valence states, i.e. Bi^{2+} and Bi^+ ions, under femtosecond laser irradiation. It is suggested that multiphoton absorption process and photoreduction of Bi^{3+} ions are involved in the experimental phenomenon. Through Joule heating, multiphoton ionization, and collisional ionization, free electrons are created in the femtosecond laser focused area. After that, Bi^{3+} ions capture the free electrons and hence transform into Bi^{2+} , and even Bi^+ ions. The holes would be trapped at non-bridging oxygen in the SiO_4 polyhedrons. Note that $\text{Bi}^{3+} + e^- \rightarrow \text{Bi}^{2+}$ and $\text{Bi}^{2+} + e^- \rightarrow \text{Bi}^+$ are very similar to the conventional chemical



process. It is suggested that control of the laser parameters can tune the active centers for the luminescence tuning of main group metal ion-doped phosphors.

Apart from the tuning by femtosecond laser irradiation, luminescence of Bi-doped phosphors can be modulated by γ ray irradiation. Bi doped α -BaB₂O₄ (α -BBO) single crystals were prepared through Czochralski method in N₂ atmosphere [Su, 2009]. The absorption and emission spectra of as-grown crystals indicate that Bi²⁺ and Bi³⁺ centers are occurred in the hosts. There was no NIR luminescence in the as-grown Bi doped crystals under 808 nm and 980 nm laser diodes excitation. In contrast, intense NIR emission was observed in the γ ray irradiated Bi doped α -BBO (see Figure 1.8 (c)). Bi⁺ ions are considered as the NIR luminescent center. Under γ ray irradiation, the electrons can be easily released from the Ba vacancies (V_{Ba^+}), and would freely displace in the lattice. Then the Bi²⁺ and Bi³⁺ ions would capture the free electrons and transform to Bi⁺ centers. Interestingly, the γ ray irradiated Bi doped α -BBO can be bleached by heat annealing, due to the processes of $Bi^+ - 2e^- \rightarrow Bi^{3+}$ and $V_{Ba^+} + 2e^- \rightarrow V_{Ba^{2+}}$. Similarly, NIR luminescence from γ ray irradiated Bi doped Y₄GeO₈ crystals was investigated [Xu, 2011].

1.3.2.2 Bi-doped fiber NIR photonic materials

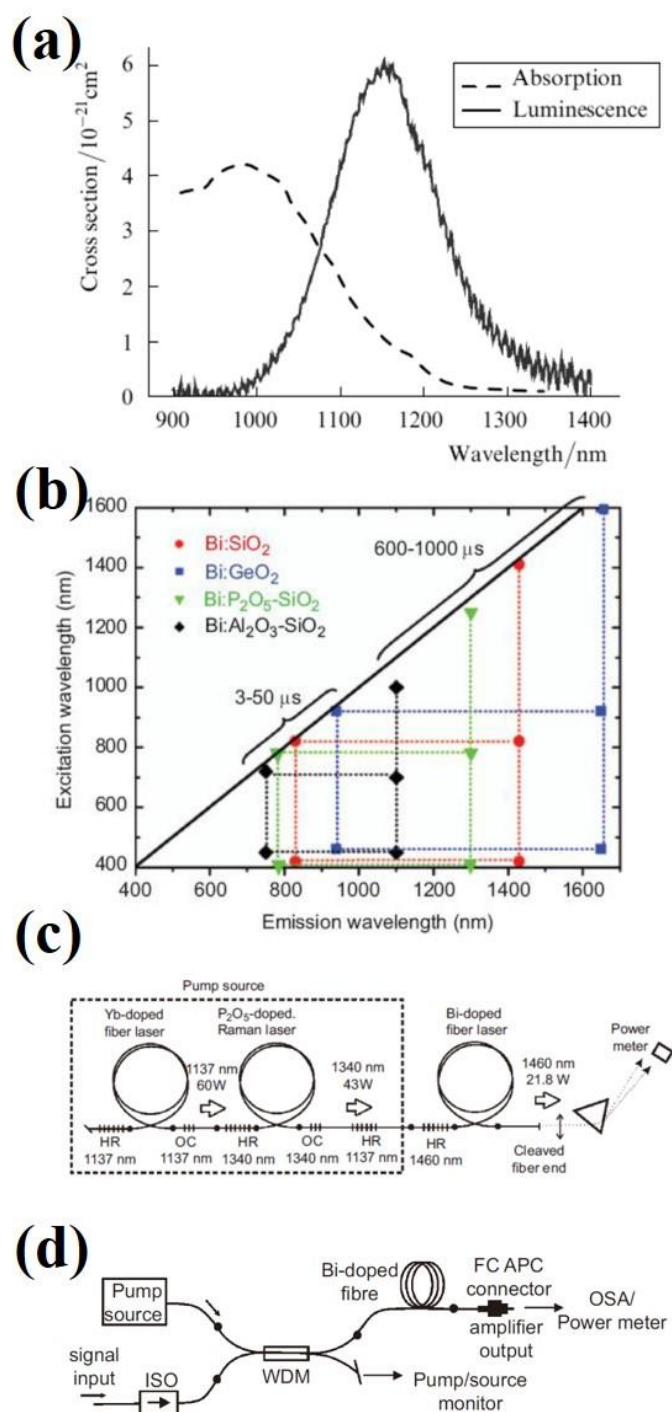


Figure 1.9 (a) Absorption and luminescence cross section spectra of a Bi-doped



aluminosilicate fibre [Haruna, 2005]. (b) A summary scheme of the main emission peaks for different fibers. The types of fibers and lifetime values for various luminescence bands are also indicated [Dianov, 2012]. (c) The 1460 nm Bi-doped fiber laser. HR, high reflectivity fiber Bragg grating; OC, output coupler. [Firstov, 2011] (d) A Bi-doped fiber amplifier. ISO, optical isolator; WDM, wavelength division multiplexing coupler; OSA, optical spectrum analyzer; FC APC connector, Fiber-optics connector for Angled Physical Contact [Melkumov, 2011].

In 2005, the Bi-doped optical fiber was first fabricated via the Modified Chemical Vapour Desposition (MCVD) technique [Dvoyrin, 2005; Haruna, 2005]. The fiber core consisted of Bi-doped $\text{Al}_2\text{O}_3\text{-SiO}_2$ glass. The core of performs was formed by CVD of Al_2O_3 and SiO_2 . Doping with bismuth oxide was performed by impregnating a porous layer of the core glass with the solution of bismuth salts. The molar concentration of bismuth oxide in the core glass did not exceed 0.1 %. Figure 1.9 (a) presents absorption and luminescence cross section spectra of a Bi-doped $\text{Al}_2\text{O}_3\text{-SiO}_2$ glass fiber. The emission cross section at 1150 nm reaches up to $6 \times 10^{-21} \text{ cm}^2$, which is more or less similar to that of Er-doped optical fiber at 1500 nm. Then several fiber lasers were reported using the fabricated Bi-doped fibers [Dvoyrin, 2008; Gao, 2012]. Subsequently, various kinds of Bi-doped optical fibers were developed, including fibers with cores consisting of Bi-doped SiO_2 , Bi-doped GeO_2 , Bi-doped $\text{P}_2\text{O}_5\text{-SiO}_2$, Bi-doped $\text{GeO}_2\text{-SiO}_2$ and Bi-doped $\text{P}_2\text{O}_5\text{-GeO}_2\text{-SiO}_2$ glasses. Figure 1.9 (b) summarizes luminescence properties of several Bi-doped optical fibers



[Dianov, 2012]. One can see that the luminescence of the Bi-doped fibers can cover 750 to 1700 nm (through the whole spectral region), under the excitation between 400 and 1600 nm. The photoluminescence properties are mainly affected by the composition. For instance, the longest emitting wavelength of Bi-doped $\text{Al}_2\text{O}_3\text{-SiO}_2$ is 1100 nm; the longest emitting wavelength of Bi-doped SiO_2 is 1430 nm; whereas the longest emitting wavelength of Bi-doped GeO_2 is 1660 nm. This figure also illustrates the lifetimes of the different luminescence bands. For the wavelengths longer than 1000 nm, the lifetime values are 600-1000 μs ; for shorter wavelengths, they are 3-50 μs . Recently, high-power, efficient Bi-doped fiber laser operating at 1460 nm is reported (see Figure 1.9 (c)) [Firstov, 2011]. A Yb-doped fiber laser operating at 1137 nm was utilized to pump the Raman laser. A phosphosilicate fiber Raman laser operating at 1340 nm was used as a pump source. For full absorption of the Raman laser radiation, the length of the Bi-doped fiber was fixed at 95 m. The maximum output power at 1460 nm is 21.8 W. The power conversion efficiency of the fiber laser was ~50 %. On the other hand, a fiber amplifier based on a Bi-doped $\text{GeO}_2\text{-SiO}_2$ fiber with a commercial laser diode for pumping was developed [Melkumov, 2011]. The design of Bi-doped fiber amplifier is shown in Figure 1.9 (d). The pump and the signal were launched through a wavelength division multiplexing coupler. The used active fiber length was 125 m. Two different pump sources were used: 1). a home-made Raman fiber laser operating at 1320 nm with output power of up to 500 mW; 2). a commercially available, single-mode laser diode operating at 1310 nm with output power of up to 80 mW (LPSC-1310-FC; Thorlabs (Newton,

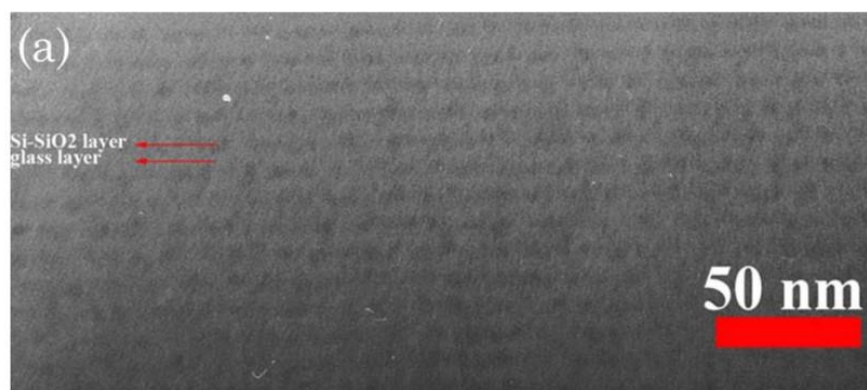


New Jersey, USA)). Two different types of light sources were used as signals: 1). a multiline signal source based on a supercontinuum fiber source and a set of high-reflectivity fiber Bragg grating (1330-1650 nm, FWHM \sim 0.7 nm); 2). a fiber Bragg grating-stabilized diode laser at 1427 nm. An optical isolator was used to suppress optical feedback and to prevent laser generation in the active fiber. The first signal source was used to measure the amplifier gain spectra and noise figure. The second source enabled us to examine the saturation characteristics of the amplifier. Finally, a 24 dB gain Bi-doped fiber amplifier at 1430 nm pumped by a 65 mW commercial laser diode at 1310 nm was achieved. The system had demonstrated a 3 dB bandwidth of about 40 nm, a noise figure of 6 dB, and a power conversion efficiency of about 60%. Compared with the previous results, these results gain considerable improvements of Bi-doped fiber amplifier characteristics.

1.3.2.3 Bi-doped thin film NIR photonic materials

Realizing ultrabroad photoluminescence in thin films doped with Bi ions is critical for their application in integrated photonics. In 2010, Sun et al. reported NIR luminescence in bismuth glass/Si nanocrystal superlattices [Sun, 2010]. The novel superlattices were fabricated by sputter deposition of thin Si rich SiO₂ (Si-SiO₂) and Bi-doped aluminosilicate glass layers alternatively on fused quartz substrates by using a multitarget sputtering system. The thickness of glass/Si-SiO₂ layers in the superlattices is 5 nm/3 nm, and the period was 100. The Si/O ratio in the SiO₂ layer is around 1.24. After deposition, the films were thermally treated in N₂ at 950 °C for

20 min. Figure 1.10 (a) presents the cross-sectional high-resolution transmission electron microscopy (HRTEM) image of the annealed superlattices, which obviously demonstrates well preserved layer upon layer structure and some dark regions appear. The dark region suggests the formation of Si nanocrystals in the superlattices. Figure 1.10 (b) and (c) show the photoluminescence spectra of the prepared Bi-doped glass film and superlattices. Obviously, the emission from the superlattices under 325 nm excitation is much stronger than that from the glass film. It is noted that these two samples exhibit quite different emission bands. The enhanced mechanism for the NIR emission in the superlattices is proposed that energy transfer from Si nanocrystals sensitizes excitation of Bi active centers. The sensitization effect leads to enhanced NIR emission intensity, broad and flat NIR emission from the superlattices [Miwa, 2011].



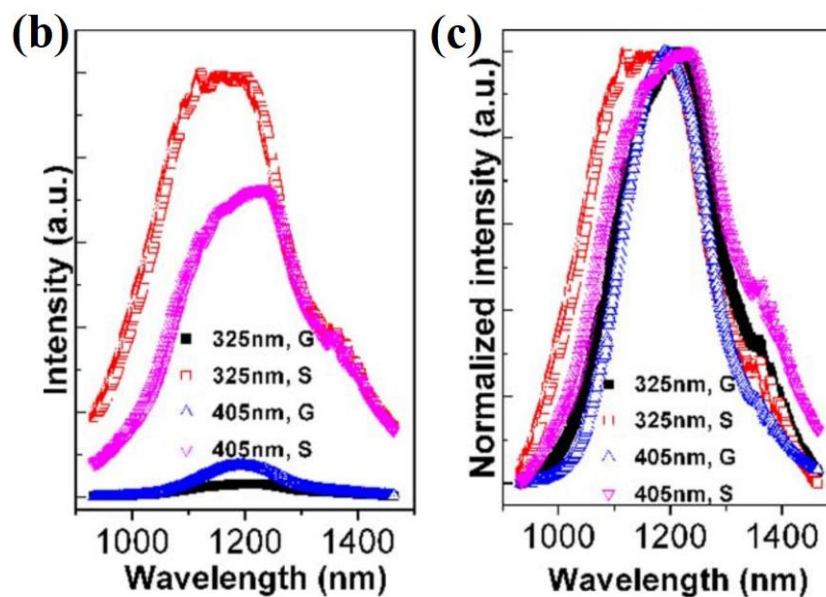


Figure 1.10 (a) Cross-sectional HRTEM image of the annealed superlattices. (b) NIR PL spectra of the annealed glass film (G) and superlattices (S) under the excitation of 325 and 405 nm. (c) The normalized NIR PL spectra of the samples G and S under the excitation. [Sun, 2010].



1.4 Motivation of research

Recently, ever-increasing demand in optical communication, biomedicine, light sources, and energy has raised the immediate need for multifunctional NIR photonic materials, such as broadband optical amplifiers, bioimaging probes and tunable lasers. However, these challenges are still ahead, and many requirements are not well met at present. Currently, non-rare-earth dopants including the transition metal Ni^{2+} ion and main-group element Bi present ultrabroadband NIR emission, which is very inspiring. Compared with the developed Er-doped photonic materials, non-rare-earth doped materials show unusual luminescence, due to the unsheltered outer electrons. Specifically, the NIR emission from Ni-doped photonic materials can be modulated by tailoring matrixes, as the transitions among d orbits of Ni^{2+} ion are very sensitive to the micro-environment. The NIR emission from Bi-doped photonic materials can be modulated by control the Bi clusters through rational selection of host materials, facile control of preparation processes under suitable conditions. These interesting performances provide plenty of opportunities for further tailoring the spectroscopic features of non-rare-earth photonic materials. Therefore, it is of great interest to research unusual luminescence of Ni- and Bi-doped photonic materials. In this thesis, ferroelectric oxides will be considered as the host of Ni-dopant to form multifunctional photonic materials. The influence of chemical composition, temperature on the NIR emission will be investigated. Bi-doped oxide glasses with different composition and processes will be fabricated and studied. The objective is



to achieve the desired NIR luminescence through understanding the emission mechanism of non-rare-earth.

Thin-film photonic materials are quite important for integrated photonic technology [Zhang, 2013]. Unfortunately, previous results on Ni- and Bi-doped luminescent materials are mostly limited to the studies on crystals and glasses. Further fundamental investigation and application of these materials are hindered owing to the lack of Ni- and Bi-doped thin-film photonic materials with ultrabroadband NIR emission. Following the works on Ni- and Bi-doped bulks, non-rare-earth doped materials in thin-film configuration will be designed, synthesized and characterized. The thin-film photonic materials will be prepared by pulsed laser deposition (PLD) methods. PLD has been demonstrated as a powerful technique of preparing complex oxide thin-films, which can realize stoichiometric transfer of compositions from the bulk target [Xu, 2013]. The micro-structures of thin-films can be precisely controlled using some unique growth technique, differing from the previously reported crystal and glass bulk fabrication. And then a series of measurements will be carried out to the characterization of structural and luminescent properties of the photonic films. The experimental emphasis will be put on the study of dependence of the controlled structure and crystallization of the films on their NIR emission characteristics. The prepared thin-films are expected to present much broader emission band in NIR spectral region in contrast with developed Er-doped materials. Moreover, considering the physical properties of thin-



film can be readily modulated by the external field, such as strain and electric field [Bai, 2015]. Hence tunable and electric control of luminescence will possibly be realized in these films. Ni- and Bi-doped thin-film materials in the study are promising broadband optical gain media for potential application in planar optical amplifiers and other integrated photonic technologies. Therefore, this study will be very helpful for deep understanding of ultrabroadband NIR luminescence in non-rare-earth doped photonic materials and the development of thin-film integrated photonic technology.



1.5 Structure of thesis

The main objective of present work is to study non-rare-earth doped thin-film photonic materials with ultrabroadband near-infrared luminescence. The thesis consists of six chapters:

Chapter 1: Introduction. In this chapter, the background of NIR luminescence is first introduced, followed by metal ions-doped photonic materials with NIR emission beyond rare earth ions. Then the motivation and objectives of this thesis are presented.

Chapter 2: Experimental Techniques. This chapter introduces the fabrication methods for Ni- and Bi-doped photonic materials, including bulk and thin film samples. The characterization instruments and techniques.

Chapter 3: Transition Metal Ni-doped Photonic Materials with Broadband NIR Luminescence. In this chapter, Ni-doped photonic materials with tunable broadband NIR luminescence will be presented, including chemical substitution-induced exceptional emitting-wavelength tuning in Ni²⁺-doped ferroelectric oxides with ultrabroadband NIR luminescence, temperature dependence of broadband NIR luminescence from Ni²⁺-doped Ba_{0.5}Sr_{0.5}TiO₃, and Ni²⁺-doped thin films.

Chapter 4: Strain-Induced Modification of NIR Luminescence of SrTiO₃:Ni²⁺ Thin Films. In this chapter, Tunable NIR luminescence of Ni²⁺ doped SrTiO₃



(STO:Ni) thin film grown on piezoelectric $\text{Pb}(\text{Mg}_{1/3}\text{Nb}_{2/3})_{0.7}\text{Ti}_{0.3}\text{O}_3$ (PMN-PT) substrate via strain engineering have been investigated.

Chapter 5: Broadband NIR Luminescence from Bi and Bi/Ho co-doped Thin Films. In this chapter, ultrabroadband near-infrared luminescence in the 1.0-2.4 μm range has been observed in Bi-doped oxyfluoride germanate thin films prepared by PLD. With the sensitization of Bi near-infrared active centers, enhanced broadband $\sim 2 \mu\text{m}$ luminescence of Ho^{3+} is realized in Bi/Ho codoped films, and a high energy transfer efficiency is obtained.

Chapter 6: Conclusions and Suggestions for Future Work. In this chapter, the results in this thesis are concluded. Meanwhile, future prospect of non-rare-earth doped thin-film photonic materials with ultrabroadband near-infrared luminescence is presented.



Chapter 2 Experimental Techniques

Ni-doped ceramics bulks as well as the polycrystalline targets for PLD were prepared by solid state chemical reaction synthesized method. Bi-doped glass targets were prepared by a melt-quenching approach. All thin films studied in this thesis were deposited by PLD method. Their structure characteristics were determined by X-ray diffraction, scanning electron microscope, Raman spectroscopy. The electric properties of samples were measured by an impedance analyse and a modified Sawyer-Tower circuit. The luminescent properties of samples were studied by fluorescence spectrometer.

2.1 Sample preparation

2.1.1 Fabrication of the bulk samples

The ceramics bulks are fabricated by the conventional solid state reaction method. The main processing flow is described in Figure 2.1. The starting raw chemicals are Ba_2CO_3 (99.9%), Sr_2CO_3 (99.9%), TiO_2 (99.9%), NiO (Reagent grade). These powders are weighed according to the stoichiometric ratio of the designed formulas using electronic scales. The mixing and grinding processes were accomplished by ball-milling using zirconia balls for 10 h with deionized water. And then the mixture was baked to remove moisture and calcined in an alumina crucible, in order to form a chemically and crystallographically uniform structure. After that,

the calcined powders were mixed thoroughly with a 5 wt. % polyvinyl alcohol (PVA) binder solution for shaping and strengthening the dry forms. Finally the ceramics disk samples were sintered after being pressed into disks under pressure.

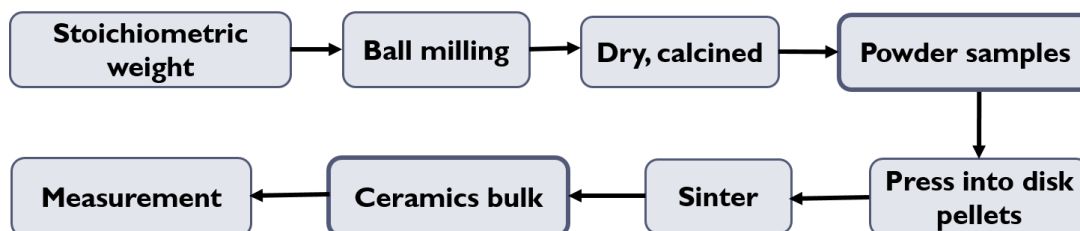


Figure 2.1. Flow diagram of the ceramics's preparation procedure.

The glass targets were prepared by a melt-quenching approach. Analytical grade reagents were used as raw materials. Based on the designed formulas, the mixed raw powders were melted in platinum crucibles above the melt temperature and then cast onto a stainless steel plate. The obtained glasses were annealed below the crystalline temperature and then cooled to room temperature. Finally the glasses were cut into pieces and then polished.

2.1.2 Pulsed laser deposition (PLD)

PLD is one of the generally used methods for the growth of thin films developed in the recent years [Kramer, 2003]. All the thin film samples used in the study are deposited by PLD. The thin film growth by PLD technique includes evaporation of a target to be deposited in the presence of a background gas or in an

ultra high vacuum. The typical PLD system is presented in Figure 2.2. A high energy pulsed laser is focused to strike the target, inducing sufficiently high flux densities. The atoms of the target material are rapidly evaporated, within the incident laser pulse penetration depth. Then the emitted materials from the target surface travel as a plasma. The plasma density can be described by a $\cos^n(x)$ law with a Gaussian curve shape. The high energetic species ablated from the bulk target are bombarding the substrate surface and may cause some damage to the surface. They may sputter off some atoms from the substrate surface, and also form a collision region. This thermalized region serves as a source for condensation of particles. When the condensation rate is higher than the rate of particles from the sputtering, once thermal equilibrium reaches, the film begins to grow on the substrate surface. The critical growth parameters for the nucleation process and growth kinetics of the film comprise laser parameters, substrate temperature, substrate surface conditions, deposition rate, and background pressure.

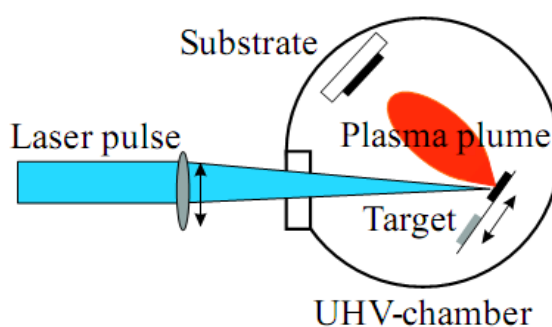


Figure 2.2. Schematic view of a typical PLD system [Kramer, 2003].



2.2 Structure characterization

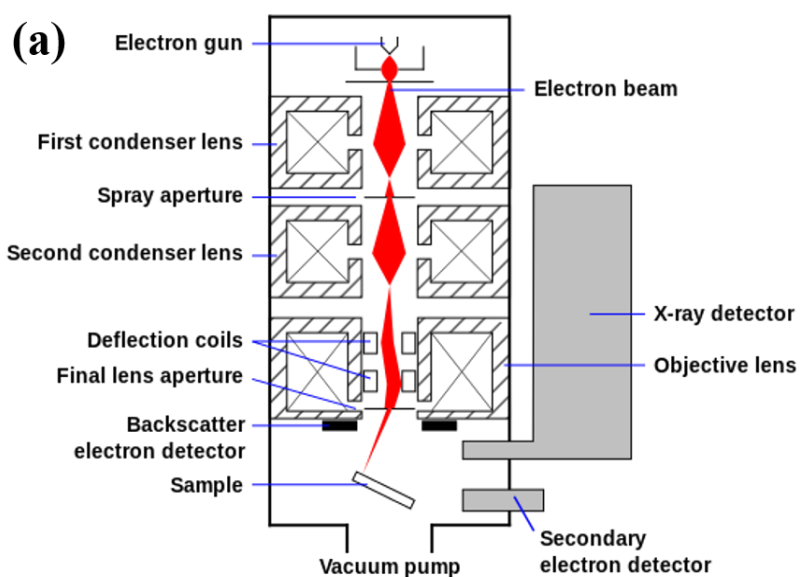
2.2.1 X-ray diffraction (XRD)

XRD can be utilized to investigate the crystalline structure of the bulk and thin film samples. A beam of incident X rays is scattered by the electron clouds of the individual the crystalline atoms, forming a diffraction pattern. By measuring the diffraction pattern, numerous information about the atomic and molecular structure materials and thin films can be obtained. In 1913, William Lawrence Bragg first used XRD to investigate the three-dimensional atomic arrangement information in a crystalline solid. A crystal is a solid material whose constituents, including atoms, molecules or ions, have an order repeating pattern in three spatial dimensions. Considering the atomic arrangement, crystals are divided into seven crystal systems (triclinic, tetragonal, trigonal/rhombohedral, monoclinic, orthorhombic, hexagonal, and cubic), combined with four crystal lattice types (primitive, single-face-centered, face-centered, and body-centered) to give 14 Bravais lattices. These Bravais lattices combined with symmetry elements cause 230 space groups. All crystals belong to one kind of 230 space groups. In general, the interatomic distance in a crystal is of the order of 0.1 nm to 1 nm. To investigate the fine crystal structure, a radiation source with a wavelength comparable to or smaller than the dimensions of the interatomic distances should be considered. X rays have high energies ranging from about 100 eV to 10 MeV, responding to wavelength ranging from about 10 to 10^{-3} nm. When a parallel beam of X-rays is incident on the testing sample, the incident

X-ray beam will be reflected by the crystal planes. The incident X-ray, the plane normal, and the diffracted X-ray are coplanar. The angle between the incident X-ray and the normal to the reflection plane is equal to the angle of reflection. When the Bragg equation derived by Bragg is fulfilled, as a result the diffraction maxima occur.

$$n\lambda = 2d_{hkl} \sin \theta \quad (2.1)$$

Here, n is the order of reflection, λ is the wavelength of X rays, d_{hkl} is the perpendicular spacing between the lattice plane in the crystal, h , k , and l are the Miller index, and θ is the complement ($90-\theta$) of the angle of incident of the X ray beam.



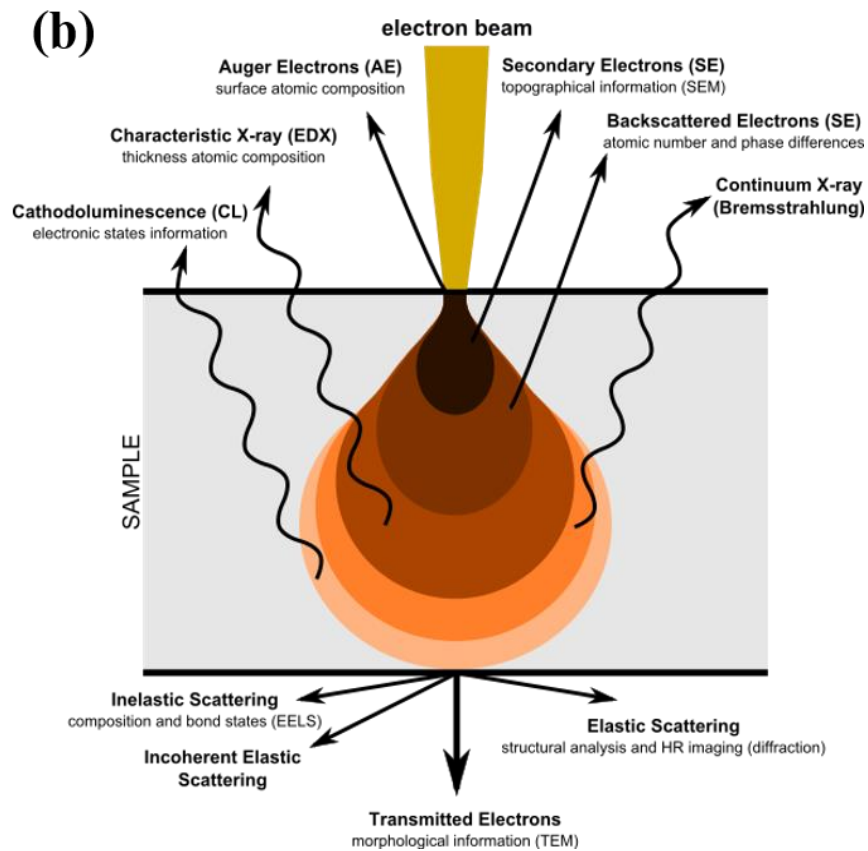


Figure 2.3 (a) Schematic of a typical SEM. (b) The schematic diagram of interactions between electron beam and a sample [Claudionico, 2013].

2.2.2 Scanning electron microscopy (SEM)

A SEM is a kind of electron microscope that uses electrons instead of light to image a sample. The SEM utilizes a focused high-energy beam of electrons produce a variety of information about the sample's surface topography and composition. An electron gun generates the electron beam, as shown in Figure 2.3 (a). The electron



beam travels through electromagnetic fields and lenses, which focus the beam down toward the sample's surface. Once the high-energy electrons hit the sample, a number of signals derive from electron-sample interaction as presented in Figure 2.3 (b). These signals contain backscattered electrons, characteristic X-ray, secondary electrons, diffracted backscattered electrons, transmitted electrons and visible light. Backscattered electrons and secondary electrons are generally used for scanning samples. Secondary electrons can be used to image the morphology and topography of samples. Backscattered electrons can be used for illustrating differences in composition of samples. The characteristic X-ray can be used to recognize the composition of elements in the samples. Compared with traditional optical microscope, the SEM takes many advantages. The wavelength of the electrons depends on the spatial resolution of the SEM, and the scanning beam is controlled by the electron-optical system. Because the wavelength of the electrons is much smaller than that of visible light used in optical microscope. The SEM has much higher resolution, which can fall somewhere between less than 1 nm and 20 nm depending on the instrument. Moreover, the SEM can provide a variety of information that contains the sample's surface topography, composition, and other properties in one time. All of these advantages make the SEM become one of the most useful instruments in research work.

2.2.3 Raman spectroscopy

Raman spectroscopy is one of the most widely used analytical techniques in the



chemical and physical sciences. In 1921, Sir Raman C. V. discovered Raman scattering effect [Raman, 1928]. The Raman spectroscopy allows the observation of vibrational, rotational and other low-frequency spectra providing information of molecules in a system. Raman spectroscopy originates from the inelastic scattering effect. Normally, when we light a sample, both the elastic and inelastic scattering will be observed. The elastic scattering is named Rayleigh scattering, where the frequency of the scattered photons is the same as that of the incident light. With regard to the Raman radiation, it is associated with the inelastic scattering, where the frequency of the scattered photons is shifted compared to that of the incident radiation. As illustrated in Figure 2.4, Raman scattering includes transitions between the vibrational and rotation levels. The Raman shift represents the energy loss of the scattered photons. For a Stokes Raman scattering, Raman shift is positive, whereas negative for an anti-Stokes Raman scattering process. Raman shift is normally stated in wavenumbers as the following equation,

$$\bar{\nu}(cm^{-1}) = \left(\frac{1}{\lambda_0(nm)} - \frac{1}{\lambda_1(nm)} \right) \quad (2.2)$$

Compared to the Rayleigh scattering, the Raman scattering process is normally very weak. In contrast, considering the Boltzmann's distribution, molecules in their vibrational ground states are much more than that in the vibrational excited states, at ambient temperature. As a result, The Stokes Raman scattering process possesses a much larger probability than the Anti-Stokes Raman scattering. Therefore, Raman

spectroscopy is usually accorded to the Stokes Raman scattering.

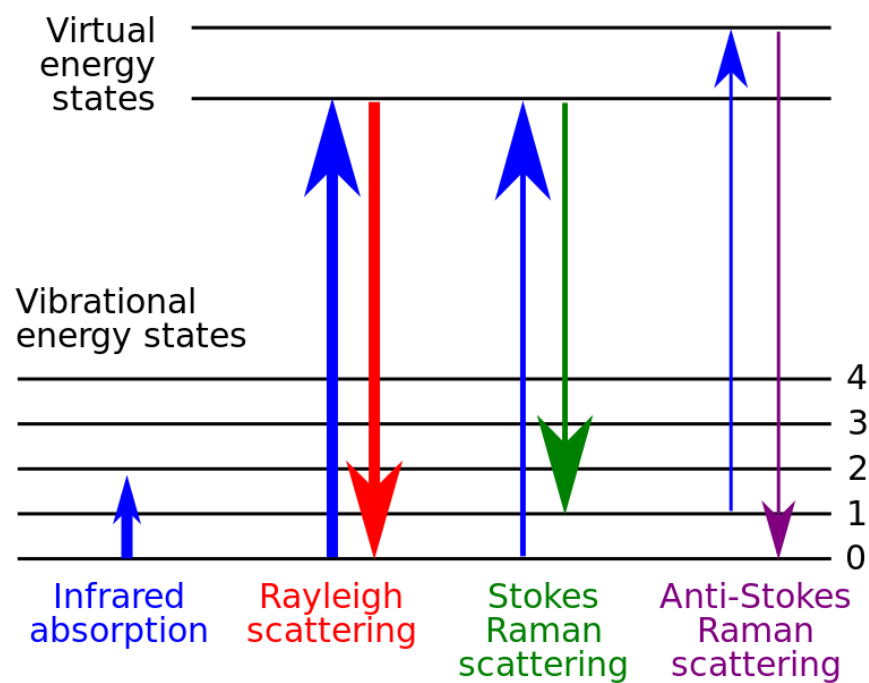


Figure 2.4 Simplified Jablonski diagram illustrating Rayleigh, Stokes, and anti-Stokes Raman scattering.

Compared to the widely used fluorescence analysis technique, Raman spectroscopy possesses its own advantages. The most fascinating feature of Raman spectroscopy is its high specificity, given that a unique fingerprint of the measured sample. Another attracting aspect of Raman spectroscopy is that it has involved a region much more extended application scope. For instance, fluorescence need there being fluorophore, whereas Raman spectroscopy can be applied any molecule.

Moreover, Raman spectroscopy can be in principle radiated under any excitation wavelength. A significant difference between fluorescence and Raman spectroscopy is that Raman scattering is an instantaneous process which means that Raman scattering can take place without a direct absorption of the photon, while this step is essential for fluorescence. The weakness of the Raman Effect is the main difficulty of Raman spectroscopy. The development of the laser together with the sensitive detectors substantially enhances the sensitivity of the Raman spectroscopy.

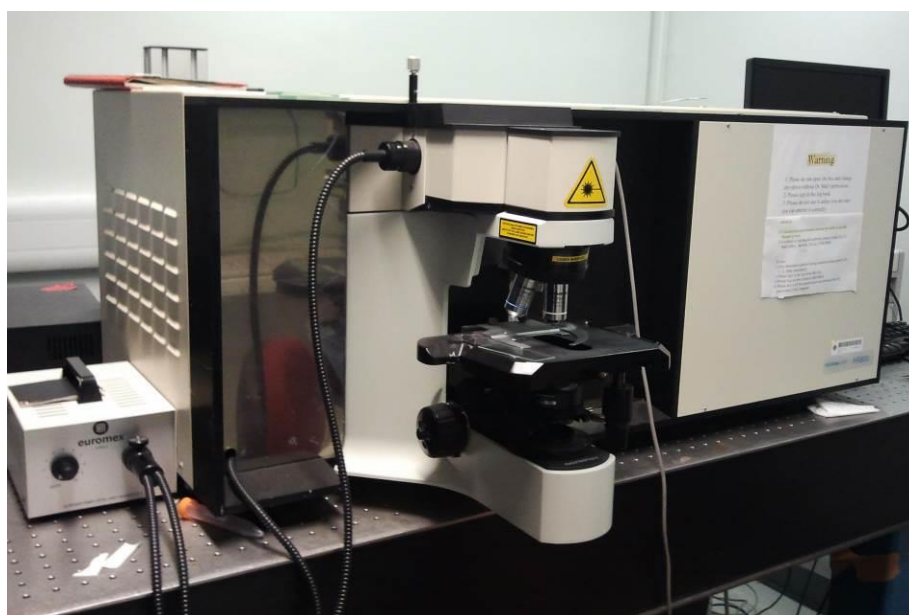


Figure 2.5 Photograph of LabRAM HR 800 Raman spectrometer in our laboratory.

In this thesis, Raman spectra were recorded utilizing a Horiba Jobin Yvon LabRAM HR800 Raman spectrometer manufactured by Horiba Jobin Yvon. The



LabRAM HR800 Raman spectrometer equipped with a 488 nm laser excitation source is shown in Figure 2.5, which is a much powerful optical instrument for material research and characterization.

2.3 Luminescence characterization

2.3.1 Steady-state photoluminescence (PL)



Figure 2.6 Photography of Edinburgh FLSP920 spectrometer used in our laboratory.

Steady-state PL spectra consist of both emission and excitation measurements. An emission spectrum is the wavelength distribution of photons emitted by atoms or molecules measured at a single constant excitation wavelength. An excitation spectrum is in opposition, whereby the emission is recorded at a single emission wavelength, upon scanning the excitation wavelength. All the PL spectra in the thesis are recorded by an Edinburgh FLSP920 spectrometer as presented in Figure 2.6. The FLSP 920 is a modular, computer controlled spectrometer for measuring steady-state and time resolved luminescence spectra in the ultraviolet-visible-NIR

spectra range.

The individual functional components (Figure 2.7) of the Edinburgh FLSP920 spectrometer system in our laboratory can be briefly described as follow.

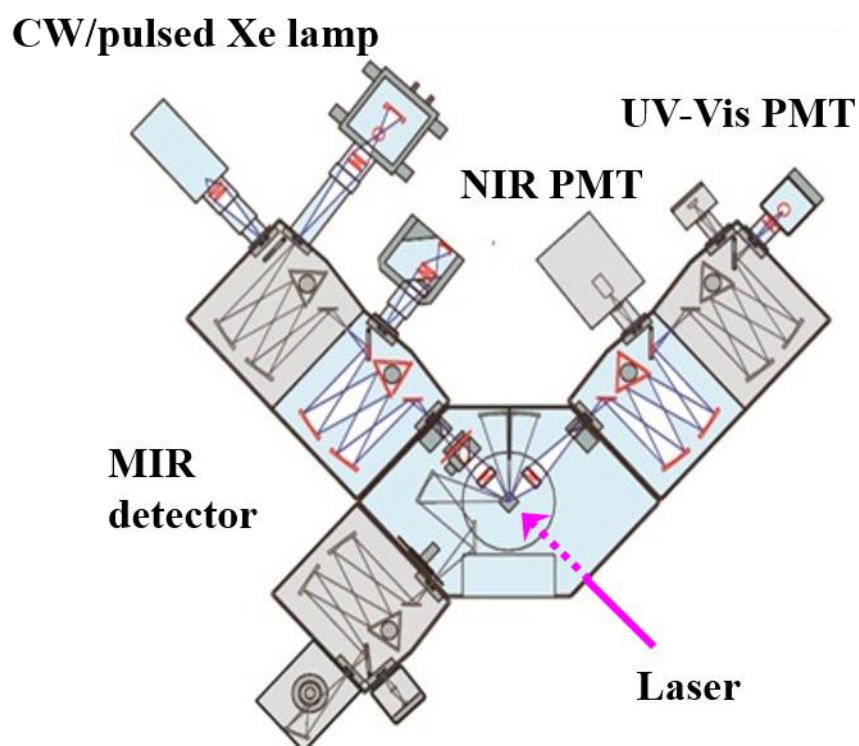


Figure 2.7 Schematic diagram of Edinburgh FLSP920 spectrometer.

Light Sources:

- Xe900 is a 450W ozone free xenon arc lamp that emits continuous radiation. The optimal spectral range extends from below 250nm to more than 1000nm.



- Continuous 325 nm He-Cd laser and 980 nm laser diode are mainly used as excitation source for NIR PL measurement.
- Nanosecond Flashlamp nF900 is a thyatron triggered, all metal, pulsed flashlamp. And provide sub-nanosecond pulses over the vacuum ultraviolet to NIR spectra range, 110-850 nm at repetition rates to 100 kHz.
- Microsecond Flashlamp μ F900 is a pulsed xenon microsecond flashlamp producing short, typically a few μ s to s, irradiance optical pulses at repetition rates of between 0.1Hz and 100Hz. It can be utilized as an excitation source for luminescence decay measurement.

Detectors:

- Red sensitive Photomultiplier (PMT) can respond to the range from 200 to 870 nm at -20 °C.
- NIR PMT operated at -80 °C is available spanning the spectral range from 300 to 1700 nm.

Grating:

- Type: Plane holographic or ruled grating
- Standard: 250/500 nm blaze, 1800 grooves/mm
- Resolution: 0.05-18 nm
- Wavelength Accuracy: 0.2 nm

2.3.2 Time-resolved PL

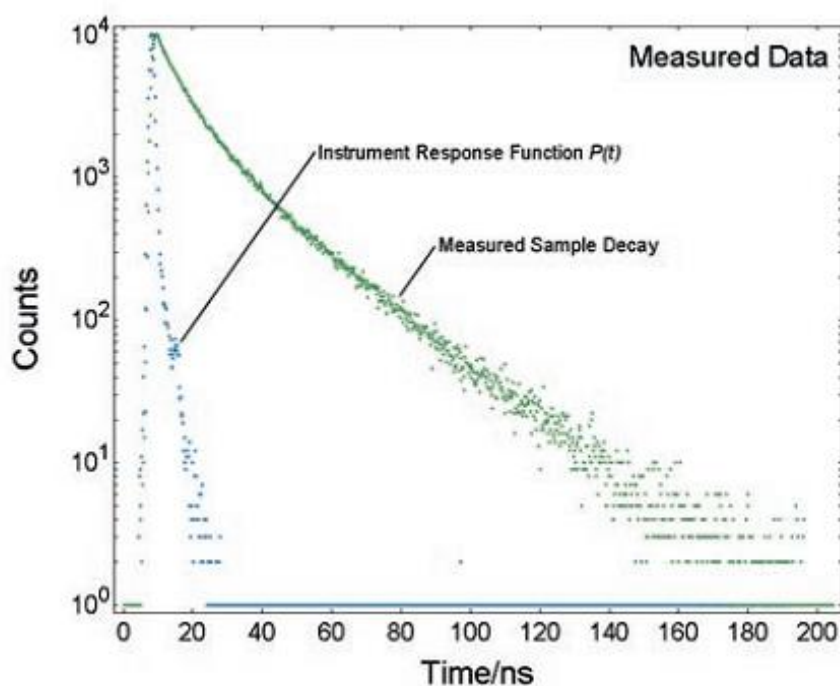


Figure 2.8 Sample of fluorescence decay curve [Zhang, 2012].

Time-resolved PL is commonly used in the research of physics, chemistry, and biology. Compared with the steady-state PL, more dynamic information can be obtained from time-resolved measurements. For example, luminescence decay kinetics provide a comprehensive picture of the phosphor and its interactions within the microenvironment. From the luminescence decay kinetics, the researcher can get a deep understanding of the electronic structure and transition mechanisms of the excited states of both organic and inorganic molecules. For luminescence decay



experiment, the sample is pumped by a pulsed of light, the time-dependent intensity of PL is recorded following the excitation pulse. The excitation sources can be used μ F900 microsecond flashlamp, and EPL-series picosecond pulsed semiconductor diode lasers. The detectors and monochromator used for time-resolved PL is the same as that of steady-state PL. A typical example of fluorescence decays recorded using FLS920 is presented in Figure 2.8.

The luminescence decay curve can be fitted into a sum of exponential terms as follow and a constant background A ,

$$I = A + \sum_i B_i \exp\left\{-\frac{t}{\tau_i}\right\} \quad (2.3)$$

and the average lifetime is given by,

$$\langle \tau \rangle = \frac{\sum_i B_i \tau_i^2}{\sum_i B_i \tau_i} \quad (2.4)$$

2.4 Electrical characterization

2.4.1 Ferroelectric measurement

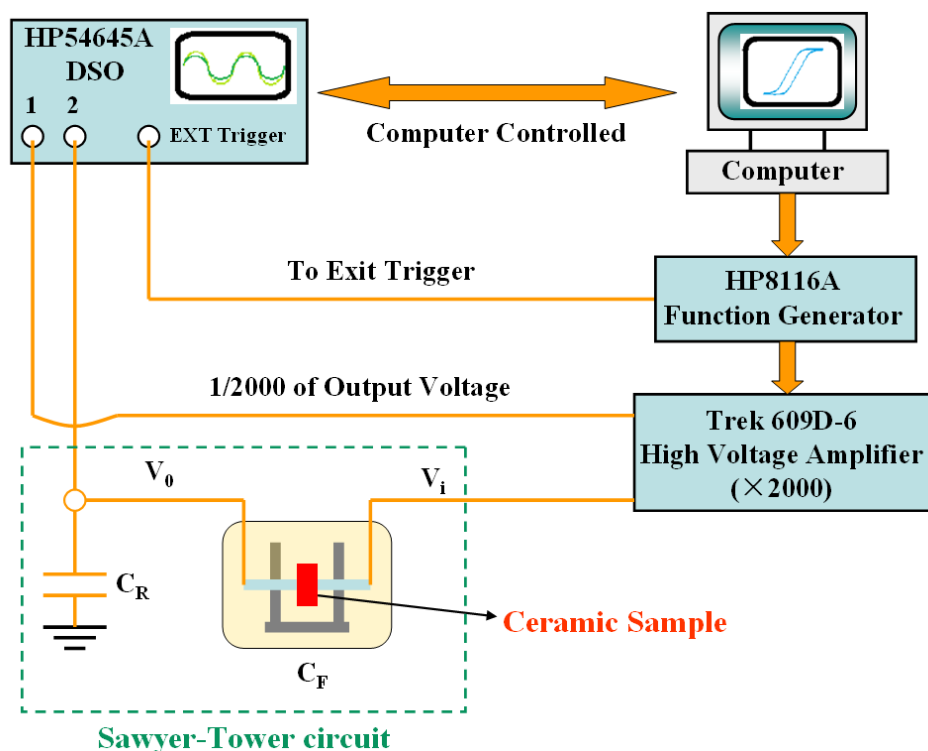


Figure 2.9 Experimental setup of typical P - E loop measurement [Wu, 2014].

The ferroelectric polarization-electric field hysteresis (P - E) loops illustrates the relationship between the applied electric field and the net macroscopic polarization of a ferroelectric material. According to the P - E loop, ferroelectric parameters including spontaneous polarization (P_s), remnant polarization (P_r), saturation polarization (P_{sat}) and electric coercive field (E_c) can be determined. In this thesis, a



revised Sawyer-Tower circuit was utilized to record the P - E loops at 100 Hz (Sawyer, 1930). Figure 2.9 displays the experimental setup for a P - E loop experiment. There are two capacitors in the Sawyer-Tower circuit: ferroelectric capacitor (CF) of measured sample and reference capacitor (CR). The CR value should be much larger (over 1000 times) than that of CF so that the voltage drop at CR can be neglected. The measured sample with electrodes is immersed in a silicone oil bath for avoiding electrical breakdown in the air. An alternating current (ac) voltage signal is produced by a HP8116A function generator, and then amplified by a high voltage amplifier (Trek 609D-6) and applied to the measured sample. A digital oscilloscope (HP54645A) is utilized to record the output voltage V_0 across CR and input voltage V_i applied to the sample. The data are collected by a computer, and the polarization P can be given as:

$$P = \frac{C_R V_0}{A} \quad (2.5)$$

where A is the area of electrode.

2.4.2 Dielectric measurement

The dielectric properties of the measured samples (with top and bottom electrodes), including the capacitance (C) and the dielectric loss ($\tan \delta$), can be measured as a function of temperature using an impedance analyzer (HP 4194A; Agilent Technologies Inc., Palo Alto, CA). The dielectric constant (ϵ_r) is given as:



$$C = \frac{\epsilon_0 \epsilon_r A}{d} \quad (2.6)$$

where ϵ_0 is the permittivity of the vacuum, A represents the electrode area of sample, and d is the thickness of sample. ϵ_r can be expressed as $\epsilon_r = \epsilon' - \epsilon''$, where ϵ' is the real part of the dielectric constant and ϵ'' the imaginary part. The dielectric loss is defined as:

$$\tan \delta = \frac{\epsilon''}{\epsilon'} \quad (2.7)$$

The measured ceramic sample connected to the impedance analyzer is placed inside a chamber, in which the temperature could be varied from 80 K to 400 K, through liquid nitrogen cooling and electric heat. The exact temperature in the chamber is measured by a thermocouple connected to a Keithley multimeter. The data from both the impedance analyzer and the multimeter were recorded and analyzed by a computer.



Chapter 3 Ni-doped Photonic Materials with Broadband NIR Luminescence

3.1 Chemical substitution-induced emission modulation in Ni²⁺-doped ferroelectric oxides

In this section, perovskite Ba_xSr_{1-x}TiO₃ oxides were utilized as host of Ni²⁺ dopant to achieve simultaneous ferroelectric and optical properties. Both exceptional tunable luminescence and ferroelectric properties were realized through chemical substitution. The mechanism behind the observation is discussed, and the interestingly tunable luminescence originates from the change in the specific structure of ferroelectric matrix.

3.1.1 Introduction of tunable NIR PL and Ni²⁺-doped ferroelectric oxides

NIR photonic materials have drawn great attention, as they have potential applications in processing and controlling light for active components of biomedicine, optical telecommunication devices, and light sources [Eliseeva, 2010; Smith, 2009; Sun, 2009]. For example, extensive effort has been made to acquire rare-earth (RE) ions doped optical amplifiers (e.g., Er³⁺-, Tm³⁺-, or Pr³⁺-doped optical fiber amplifiers) [Li, 2011; Tian, 2011], to meet the enormous demands for huge information transmission of the increasing growth of internet industry.



However, limited by the inherent narrow $f-f$ transitions of RE ions, the emission bandwidth of RE activated amplifier is typically less than 100 nm [Xu, 2013]. For expanded the bandwidth of the phosphors, the electronic vibration principle have been introduced to phosphors to broaden the electronic transitions involving simultaneous absorption or emission of both phonons and photons. Since radiation transitions among d orbitals of transition metal ions are very sensitive to matrixes, the luminescence should be closely related to the emitting electronic transitions and vibrational excitations of the lattice simultaneously, instead of purely electronic lines detected in most RE ions. In particular, Ni^{2+} ions seem to be a promising active center because of its ultrabroadband emitting band located in the low-loss optical communication windows [Zhou, 2009; Zhou, 2011].

On the other hand, active optical materials with tunable emitting-wavelength have a wide range of applications, such as display systems, biological labeling, and laser devices [Sargent, 2005; Won, 2012]. At present, one of convenient methods in tuning NIR emission is to develop quantum dots (QDs), such as CdTeSe, PbS, PbSe, and HgTe [Steckel, 2003; Tessler, 2002]. In this routine, the emitting-wavelength of QDs can be modified by altering their particle size owing to the variation of their band gap [Tessler, 2002]. Nevertheless, the solution process of NIR QDs cannot effectively eliminate the optical loss caused by hydroxyl species, and they have difficulty in large-scale applications, comparing to the solid state preparation. Furthermore, some QDs containing Cd, Pb, or Hg are seen as unfriendly to the



environment. Fortunately, modification of NIR emission corresponding to Ni^{2+} electron transition can be in theory realized through adjusting the nature of the metal-ligand interaction. Considering some parameters of material's structure such as averaged inter-nuclear distance, it is possible to design and find a suitable type of Ni^{2+} -doped hosts, resulting in a large tuning of emission wavelength.

It is noteworthy that the ferroelectric perovskite oxides with a general formula of ABO_3 formed by $[\text{BO}]_6$ octahedron [Ang, 2001; Hao, 2000; Huang, 2009], are most important type of dielectric materials extensively used for ferroelectric memory, smart sensor, and piezoelectric transducer. It is known that chemical substitution is capable of adjusting crystal structure and symmetry of perovskite oxides, and thus dramatically modify material's physical properties. In fact, RE doped ferroelectric oxides owning perovskite structure have been fabricated by Bao et al. [Gao, 2011; Zhou, 2012], and ferroelectric and optical properties were simultaneously observed, which is promising for the applications in multifunctional devices. Our recent work shows that adjustable and enhanced upconversion luminescence can be achieved in RE doped ferroelectric BaTiO_3 (BTO) materials because of the unique benefits of crystal structure in ferroelectric perovskites [Hao, 2011; Zhang, 2013]. Differing from RE ions, the electron configuration of shell layer in transition metal Ni^{2+} ion is $3d^84s^0$, consequently the emissions owing to the radiation transitions among d orbits of Ni^{2+} ion should be more sensitive to hosts compared with the previously reported RE doped ferroelectric phosphors [Zhou, 2010]. Therefore, it inspires us to study



whether ultrabroadband emission ascribing to Ni^{2+} electron transition could be largely modified through adjusting the nature of the transition metal-ligand interaction. In this section, we have selected ferroelectric $\text{Ba}_x\text{Sr}_{1-x}\text{TiO}_3$ (BST- x) compound as a host which can provide specific environment around Ni^{2+} dopant, causing strong coupling between electronic transitions in Ni^{2+} ion and vibrational transitions of the ferroelectric hosts. Most importantly, exceptional tunable and ultrabroadband NIR luminescence has been detected in Ni^{2+} -doped ferroelectric by changing the composition and crystal field.

3.1.2 Samples preparation and measurements of Ni^{2+} -doped BST- x

Ni^{2+} -doped BST- x samples were synthesized through solid state chemical reaction technique using analytical grade BaCO_3 , SrCO_3 , TiO_2 and NiO powders as raw materials. These starting powders were weighted in accordance with the molecular formula of $\text{Ba}_x\text{Sr}_{1-x}\text{Ni}_{0.005}\text{Ti}_{0.995}\text{O}_{2.995}$, where $x=0, 0.5, 0.7, \text{ and } 1$, namely STO, B0.5S0.5T, B0.7S0.3T, and BTO, respectively. Here, the Ti^{4+} site was replaced by Ni^{2+} , and the charge neutrality could be maintained by the construction of oxygen vacancies. The preliminary powders with designed stoichiometric amounts were ball milled for 24 h, then dried and calcined in air at $1100\text{ }^\circ\text{C}$ for 8 h. After the calcination, the resulting powders were pressed into disks and sintered at $1350\text{ }^\circ\text{C}$ in air for 4 h.

To determine the crystal structure, X-ray diffractometer (Rigaku, SmartLab) was utilized to record XRD patterns of the prepared samples. The PL and PLE



spectra were measured using an Edinburgh FLSP920 spectrophotometer equipped with a 450 W steady-state xenon lamp. In the meantime, the PL spectra were also recorded under the excitation of commercial 808 and 980 nm laser diodes. The decay curves were measured with a pulsed 60 W Xe flashlamp. Moreover, the polarization hysteresis loops were recorded with a conventional Sawyer-Tower circuit at 100 Hz. All the measurements were performed at room temperature.

3.1.3 Results and discussion of Ni²⁺-doped BST-*x*

Figure 3.1 (a) displays the XRD patterns of Ni²⁺-doped BST-*x* samples. As presented in Figure 3.1 (b), with the increment of Ba concentration in BST-*x*, apparent shifts of the 2θ diffraction peaks were obvious at $\sim 32^\circ$, suggesting the gradual increase in lattice constants. Such a gradual increment in lattices originates from the replacement of smaller Sr²⁺ ion with larger Ba²⁺ ion. Figure 3.1 (c) displays the 2θ diffraction peaks at $\sim 46^\circ$ for all prepared samples. Apparent splitting of the cubic diffraction (200) peak into tetragonal (200) peak and (002) peak at $\sim 45^\circ$ can be perceived when *x* value is smaller than 0.3, indicating the phases of Ni²⁺-doped BST-*x* samples changing from cubic to tetragonal with reducing Sr²⁺ content.

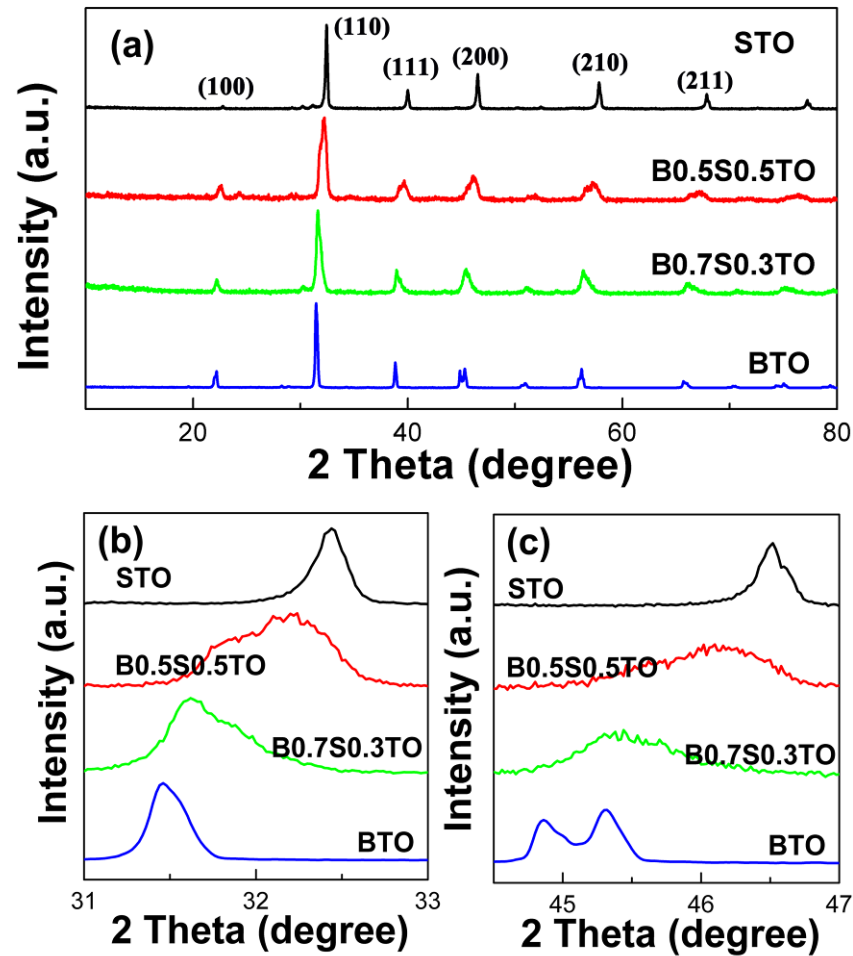


Figure 3.1 (a) XRD patterns of Ni^{2+} -doped $\text{BST-}x$ samples in the 2θ scan range of 10 to 80°. (b) 2θ diffraction peaks around 32° for the Ni^{2+} -doped $\text{BST-}x$ samples. (c) 2θ diffraction peaks around 46° for the Ni^{2+} -doped $\text{BST-}x$ samples.

The polarization hysteresis loop of Ni^{2+} -doped $\text{BST-}x$ ceramics disks is presented in Figure 3.2. Ni^{2+} -doped STO and B0.5S0.5T display linear P-E lines, signifying that they are paraelectric at room temperature. With the increment of Ba

concentration, Ni^{2+} -doped $\text{BST-}x$ displays ferroelectric property. As presented in Figure 3.2, Ni^{2+} -doped B0.7S0.3T displays a slender hysteresis loop, while Ni^{2+} -doped BTO appearances a well-defined hysteresis loop. The remanent polarization ($2P_r$) of Ni^{2+} -doped BTO is measured to be $4.41 \mu\text{C}/\text{cm}^2$. These results are constant with the XRD data. When growing Ba concentration in $\text{BST-}x$ samples, the symmetry difference from cubic to tetragonal can lead to a change in electrical property of the samples from paraelectric to ferroelectric. Activator Ni^{2+} seems to appearance little effect on the ferroelectric property of hosts, which is similar to the earlier reports on the metal-ion doped ferroelectric oxides by other research groups [Gao, 2011; Zhou, 2012].

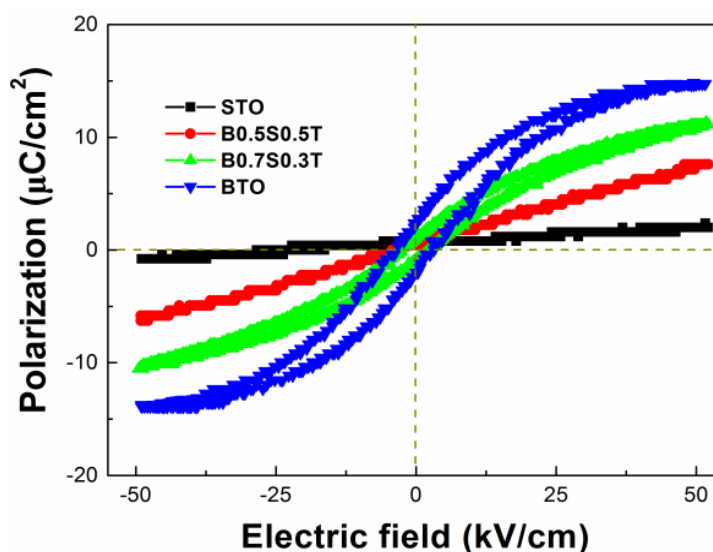


Figure 3.2 Polarization hysteresis loop of Ni^{2+} -doped $\text{BST-}x$, measured at room temperature.

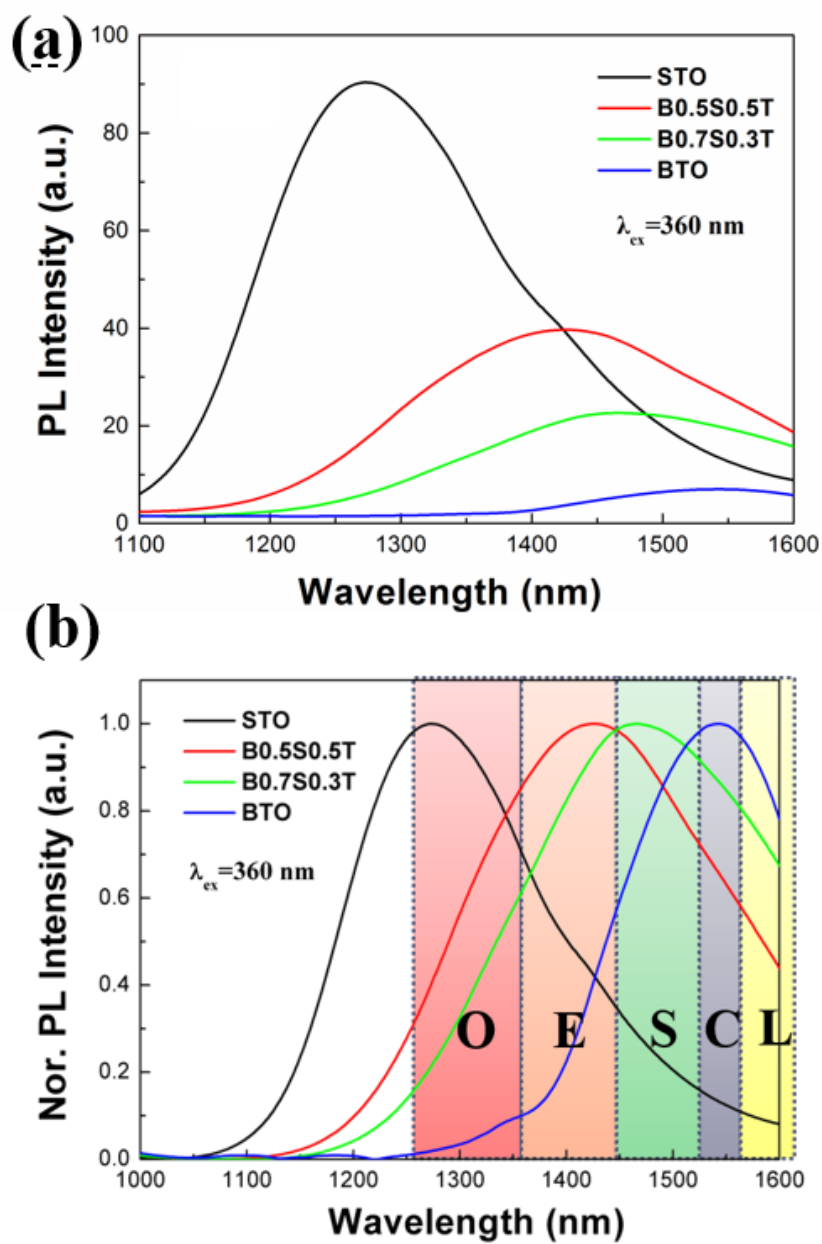


Figure 3.3 (a) PL and (b) normalized PL spectra of Ni²⁺-doped BST samples when pumped at 360 nm.

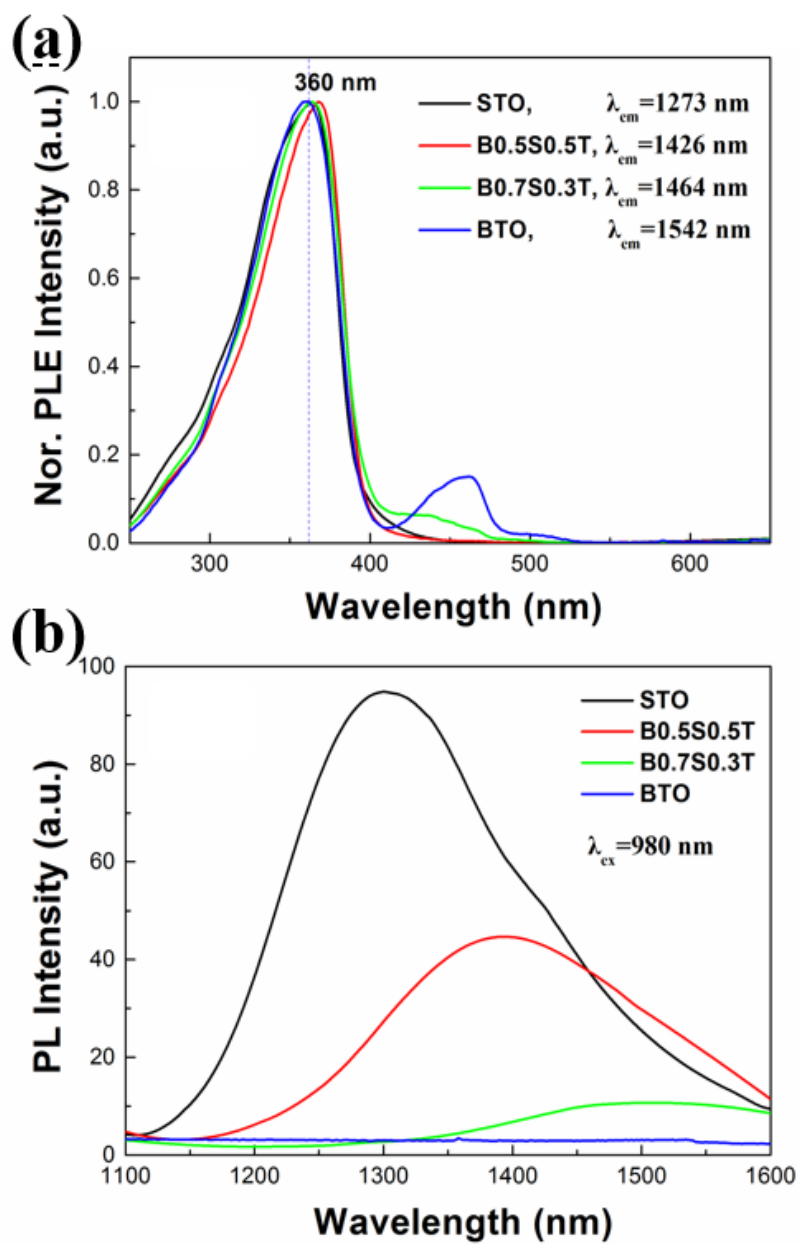


Figure 3.4 (a) PLE spectra of Ni²⁺-doped BST-*x* samples. (b) PL spectra of Ni²⁺-doped BST-*x* samples when pumped at 980 nm.



NIR PL spectra of Ni²⁺-doped BST disks under 360 nm excitation are shown in Figure 3.3. As can be clearly obtained from Figure 3.3, with x value in Ni²⁺-doped BST- x samples growing from 0 to 1, the emission peaks appearance obvious red-shifts from 1273 nm to 1542 nm bands, representing that NIR luminescence from Ni²⁺-doped BST- x can be finely adjusted by modifying the ratio of Ba/Sr. With the increment of Ba concentration, the NIR PL intensity becomes weak (see Figure 3.3 (a)). It is worth notable that the effectively tunable luminescence expands the whole optical communication window, as shown in Figure 3.3 (b). In particular, when pump at 360 nm, the FWHM of Ni²⁺-doped B0.5Sr0.5T can extent as broaden as 295 nm expanding optical communication bands between the emitting-wavelength of 1300 and 1550 nm. Figure 3.4 (a) displays PLE spectra of Ni²⁺-doped BST- x disks. PLE spectra were recorded by monitoring PL at emission peak-wavelength as presented in Figure 3.3 (a). The most intensive excitation bands of all the prepared samples are placed at about 360 nm, which can be ascribed to spin-allowed ^{VI}Ni²⁺: ³A₂(³F)→³T₁(³P). Apparent excitation bands placed at around 450 nm found in Ni²⁺-doped BTO and B0.7S0.3T, are not obvious in the other samples, which can be ascribed to spin-allowed ^{VI}Ni²⁺: ³A₂(³F)→¹T₂(¹D) [Gao, 2012]. As discussed above, Ni²⁺-doped BTO and B0.7S0.3T with tetragonal structure is dissimilar from cubic, causing the variation in PLE spectra. It is well known that commercial 980 nm diode lasers are extensively used as excitation sources for NIR optical amplifiers. Figure 3.4 (b) displays PL spectra of Ni²⁺-doped BST- x samples under excitation at 980 nm. The PL spectra are pretty similar to the results of the samples pumped at 360 nm,

suggesting that the tunable and broadband NIR luminescence from the prepared photonic materials can be also obtained with a 980 nm diode laser.

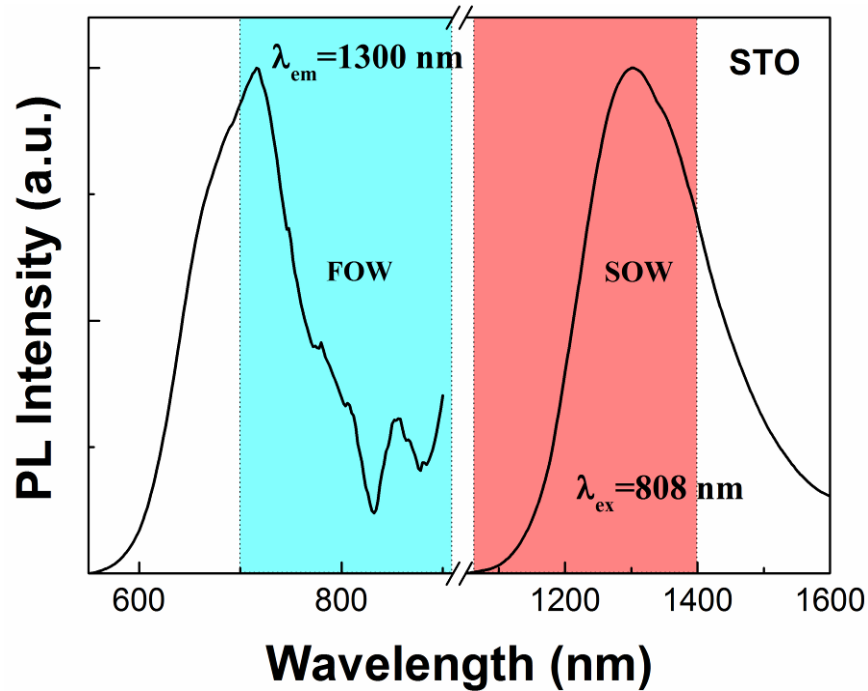


Figure 3.5 PLE spectrum of Ni²⁺-doped STO and PL spectrum of Ni²⁺-doped STO when pumped at 808 nm.

Besides the aforementioned potential optical amplifier application, NIR phosphors are acknowledged for *in vivo* bioimaging for the reason that biological tissues such as blood and skin imaging needs the utilization of NIR light within some special optical windows to avoid absorption and scattering from tissues. For this application, the NIR optical window can be divided into two special windows, named as the first optical window (FOW: 700-900 nm) and the second optical NIR

window (SOW: 1000-1400 nm), respectively [Won, 2012]. It is known that the SOW has more benefits for bioimaging compared with FOW by contemplating the lower scattering level. Nevertheless, the lack of active photonic material emitting in SOW has prohibited the practice of this highly sensitive spectral range for *in vivo* imaging [Smith, 2009]. To prove the potential application of Ni²⁺ doped phosphors applied to this area, Figure 3.5 shows PLE spectrum of Ni²⁺-doped STO when emission at 1300 nm, and PL spectrum of Ni²⁺-doped STO under excitation at 808 nm. It is notably that the excitation band of Ni²⁺-doped STO expands FOW, and the emission band shields the SOW. The recorded results suggest that Ni²⁺-doped STO is a promising candidate which could be applied in NIR imaging area.

Table 3.1 Comparison of NIR PL from Ni²⁺-doped materials.

Material	Peak shift	Method
Ni ²⁺ doped high-Ga nanocrystals	40 nm	Controlling crystal size
Ni ²⁺ doped β -Ga ₂ O ₃ glass ceramics	40 nm	Tailoring Ni ²⁺ concentration
Ni ²⁺ doped GGO and BASO	130 nm	Tuning types of nanocrystal
Ni ²⁺ doped nanocrystal-composites	150 nm	Ions impurities
Ni ²⁺ -doped ferroelectric BST (This work)	269 nm	Tailoring the ratio of Ba/Sr

In comparison to the previous results reported in Ni²⁺ doped in other hosts (as shown in Table 3.1) [Wu, 2007; Zhou, 2008; Zhou, 2009; Zhou, 2013], it is obvious

that the emitting-peak shift of Ni^{2+} -doped BST can go up to the value of 269 nm in this work, which is particularly larger than the previously reported. The remarkable tunable emission peak of Ni^{2+} -doped BST can be ascribed to the control of crystal field around Ni^{2+} and lattice relaxation, and the details will be discussed in later.

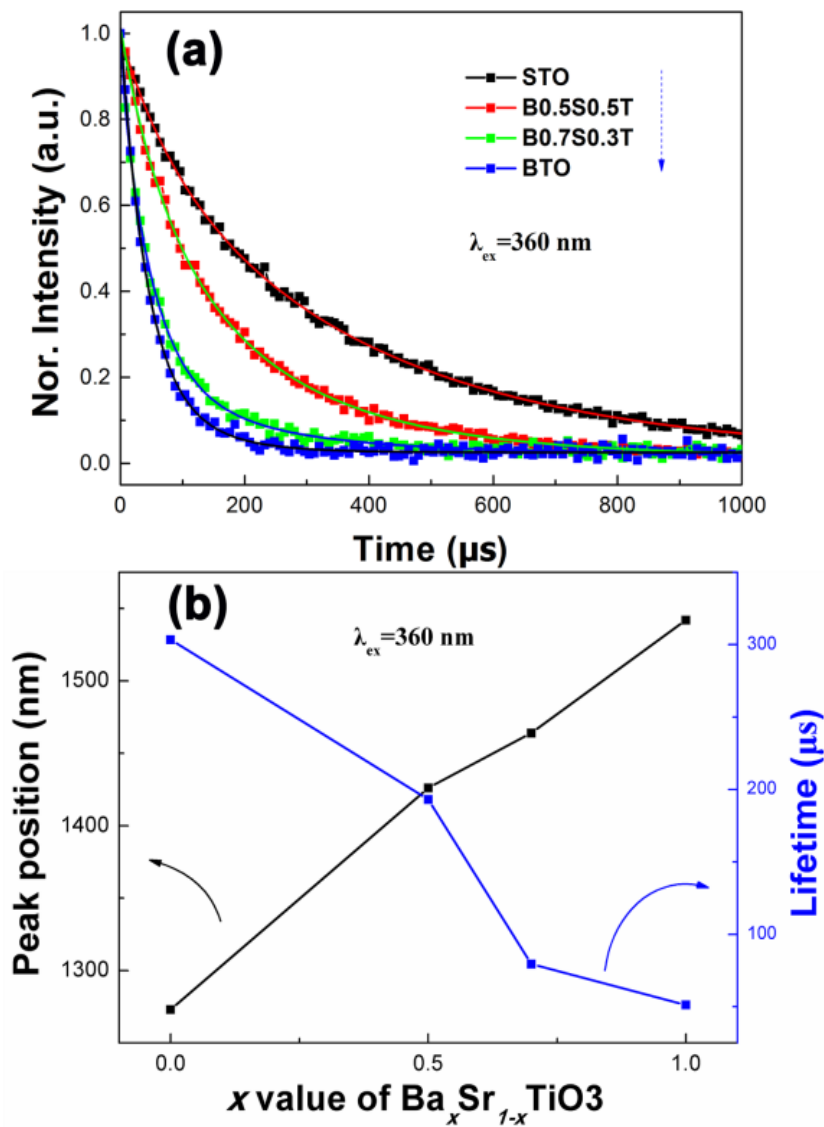


Figure 3.6 (a) PL decay curves of Ni^{2+} -doped BST samples. (b) Peak position and

lifetime of NIR PL from Ni^{2+} -doped BST.

In addition to the observed large modification of peak wavelength, the normalized NIR PL decay curves are offered in Figure 3.6 (a), recording PL intensity at emitting-wavelength under the excitation at 360 nm. With the increment of x value in BST samples, the PL decay gradually gets rapid. The effective lifetime τ is acquired from Figure 3.6 (a) when the emission intensity drops to $1/e$ of its initial value. Data on τ and λ_{em} peak of as-prepared Ni^{2+} -doped BST disks when pump at 360 nm are potted in Figure 3.6 (b). With x value in BST samples growing from 0 to 1, the emission peak position appearances a redshift from 1273 nm to 1542 nm, as well as the shift reaches as large as 269 nm, whereas the effective lifetime τ falls from 303.5 μs to 51.31 μs .

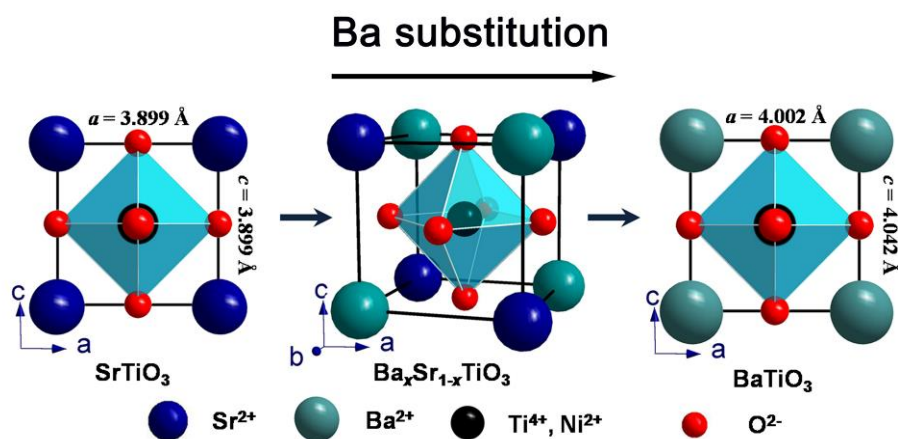


Figure 3.7 Crystal structures of perovskite BST. With the increase of barium atoms,



the crystal parameter gradually expands.

To explain the mechanism of the observed tunable luminescence, some factors, including crystal field effect, electron-phonon interaction [Brik, 2006] and the specific structure of the prepared materials should be considered. Obviously, the distribution characteristics of various energy levels play a key role in tuning luminescent properties of transition metal ions. From the well-known Tanabe-Sugano diagram [Tanabe, 1954], larger splitting energy benefits to an increase in the transition energy from the excited state levels to the ground state level.

Considering the exchange charge model of crystal field [Malkin, 1987], the energy level distribution of Ni^{2+} in this work can be characterized by the eigenvalues of the following crystal field Hamiltonian:

$$H = \sum_{p=2,4} \sum_{k=-p}^p B_p^k O_p^k \quad (3.1)$$

Here, O_p^k denote the linear combinations of irreducible tensor operators which act on angular parts of the Ni^{2+} ion wave functions. B_p^k represent crystal field parameters comprising all information about geometrical structure of an impurity center [Brik, 2006]. B_p^k contains all effects of the covalent bond formation and exchange interaction. As shown in Figure 3.1, with the rise in Ba concentration in Ni^{2+} -doped BST samples, the lattice parameter gradually enlarges, causing the longer distance of



$\text{Ni}^{2+}\text{-O}^{2-}$ bond. As presented in Figure 3.7, As $\text{Ni}^{2+}\text{-O}^{2-}$ bond distance increases from 1.95 Å (Ni^{2+} -doped STO) to 2.001 Å (axis a , b of Ni^{2+} -doped BTO), and 2.021 Å (axis c of Ni^{2+} -doped BTO), owing to the substitution of smaller Sr^{2+} ion with larger Ba^{2+} ion, the crystal field parameters B_p^k become smaller, leading to a decrease of the splitting energy and a redshift of the corresponding luminescence. Furthermore, with increasing Ba, the lattice gradually enlarges and becomes distortion, resulting in the large lattice relaxation and intensive electron-phonon coupling. According to electron-phonon interaction [Brik, 2006], the non-radiative transitions would play a key role in declining an emission intensity and bringing luminescent center redshift.

According to Mott and Gurney model [Mott, 1964], strong correlation is happened between the crystal field splitting and decay rate. Generally, the radiative transition of Ni^{2+} is usually quenched due to the mutiphonon relaxation process, and the effect can be presented by a single Arrhenius factor on the probability of the electrons occupying in the vibration excited state:

$$\tau = A \exp(-\Delta E/kT) \quad (3.2)$$

Here, A is a constant, ΔE represents the activation energy, k is the Boltzmann constant and T denotes the temperature. It suggests that the decay lifetime is affected by ΔE , which equals to the energy separation between the vibration excited state and the ground state. In general, the enhancement in the crystal field for a specific site distribution will result in the increase of the activation energy, thus leading to an



extension of the decay lifetime. As discussed above, with the increment of x value in BST- x samples, the lattice parameters gradually enlarges and the crystal field becomes smaller. And then the radiative transition of Ni^{2+} is quenched by the more intensive multiphonon relaxation. For this reason, the reduction of the decay lifetime in Ni^{2+} -doped BST- x samples is in accordance with the increment in Ba concentration. Interestingly, by facilely modifying the composition of Ni^{2+} -doped BST- x , both broadband luminescent position and effective lifetime can be modulated owing to change of the crystal field.

3.1.4 Conclusion of Ni^{2+} -doped ferroelectric oxides

In conclusion, ultrabroadband and tunable NIR luminescence from Ni^{2+} -doped ferroelectric perovskites is realized. Ultrabroadband NIR luminescence of the prepared photonic materials expands optical communication band from 1100 nm to over 1600 nm, with the largest FWHM of 295 nm. With the increment of Ba concentration of Ni^{2+} -doped BST- x , the crystal field gets weaker, as well as the peak position of NIR emission is greatly altered from 1273 nm to 1542 nm, while the effective lifetime τ falls from 303.5 μs to 51.31 μs . Remarkable peak shift extent up to 269 nm is much bigger than that of other previously recorded Ni^{2+} -doped materials. The results in this section suggest that the promise of Ni^{2+} -doped ferroelectric perovskites as a new kind of multifunctional materials for biomedicine, optical amplifiers, and tunable light sources.



3.2 Temperature dependence of broadband NIR

luminescence from Ni²⁺-doped Ba_{0.5}Sr_{0.5}TiO₃

In this section, the dielectric and photoluminescence properties of Ni²⁺-doped Ba_{0.5}Sr_{0.5}TiO₃ (BST) were studied at different temperature. The crystal structure of Ni-doped BST changes from rhombohedral to cubic when the temperature rises from 100 to 300 K. The luminescence properties are tightly associated with the crystal structure of the host BST. The luminescence variations are mainly affected by phase evolution induced crystal field change and nonradiative relaxation.

3.2.1 Introduction of Ni²⁺-doped BST

In the former section, the FWHM of Ni²⁺-doped Ba_{0.5}Sr_{0.5}TO₃ (BST) reached as large as 295 nm at room temperature. It is known that dielectric properties of BST depend on the temperature, ascribed to the change of crystal structure. Though the temperature dependent electrical and structural properties of these BST have been extensively studied for applications in tunable electrical devices [Lemanov, 1996]. Studies about temperature dependent PL from luminescent BST have been seldom reported up till now. Since the electron transitions among *d* orbits of Ni²⁺ ion are very sensitive to the matrixes [Bai, 2014], the luminescence should be strongly affected by the phase transition. Therefore it is interesting to examine the relationship between the luminescent properties of Ni²⁺-doped BST and temperature.



In this section, temperature dependent PL from Ni²⁺-doped BST will be presented.

3.2.2 Ni²⁺-doped BST Samples preparation and measurements

The Ni²⁺-doped BST powder was fabricated by solid state chemical reaction method. Analytical grade NiO, BaCO₃, SrCO₃, and TiO₂ powders were used as starting materials. These raw powders were weighted according to the molecular formula of Ba_{0.5}Sr_{0.5}Ti_{0.995}Ni_{0.005}O₃. Here, the Ti⁴⁺ site was substituted by Ni²⁺, and the charge neutrality could be maintained by the construction of oxygen vacancies. The preliminary powders with designed stoichiometric amounts were ball milled for 24 h, then dried and calcined at 1100 °C for 8 h in air. The resultant powders were pressed into disc samples with 10 mm diameter×0.5 mm thick, and sintered at 1350 °C in air for 4 h. Based the prepared disc as target, Ni²⁺-doped BST thin films were deposited on (100) LaAlO₃ (LAO) single crystal substrates by PLD. The BST film was deposited with the growth temperature of 700 °C and oxygen pressure of 20 Pa.

The XRD patterns of the prepared BST powder and thin film were measured by an X-ray diffractometer (Rigaku, SmartLab). The dielectric properties of BST disc were recorded by using an HP 4294A impedance analyzer coupled to an Oxford temperature controlled chamber (80 K to 300 K). Temperature-dependent PL analyses (5 to 300 K) were executed in a closed-cycle liquid helium cryostat. The PL and PLE spectra were recorded using an Edinburgh FLSP920 spectrophotometer



equipped with a nitrogen-cooled NIR photomultiplier tube (Hamamatsu C9940-02) and a 450 W steady-state xenon lamp. Meanwhile, the decay curves were measured with a pulsed 60 W Xe flashlamp.

3.2.3 Results and discussion of Ni²⁺-doped BST

Figure 3.8 (a) shows the XRD pattern of Ni²⁺-doped BST powder at room temperature. A standard BST ceramic pattern was detected without any secondary impurity phases, representing that Ni²⁺ ions were efficiently doped into the BST host lattice. Figure 3.8 (b) displays the temperature dependent dielectric constant of Ni²⁺-doped BST disc at the frequency of 1 kHz. One can detect three local maximum dielectric constants matching to three phase transitions: a weak peak places at about 144 K which matches up to the phase evolution from rhombohedral (3m) to orthorhombic (mm2). The weak peak locates around 178 K representing the phase evolution from orthorhombic (mm2) to tetragonal (4mm). A notable peak around 216 K is consistent to the phase evolution from tetragonal (4mm) to cubic (m3m). Thus the Curie temperature (T_c) of Ni²⁺-doped BST is measured as 216 K. These behaviours are similar with the previous reports of undoped BST bulk sample [Cao, 2006], indicating that activator Ni²⁺ ions seem to have little effect on the dielectric property of BST host.

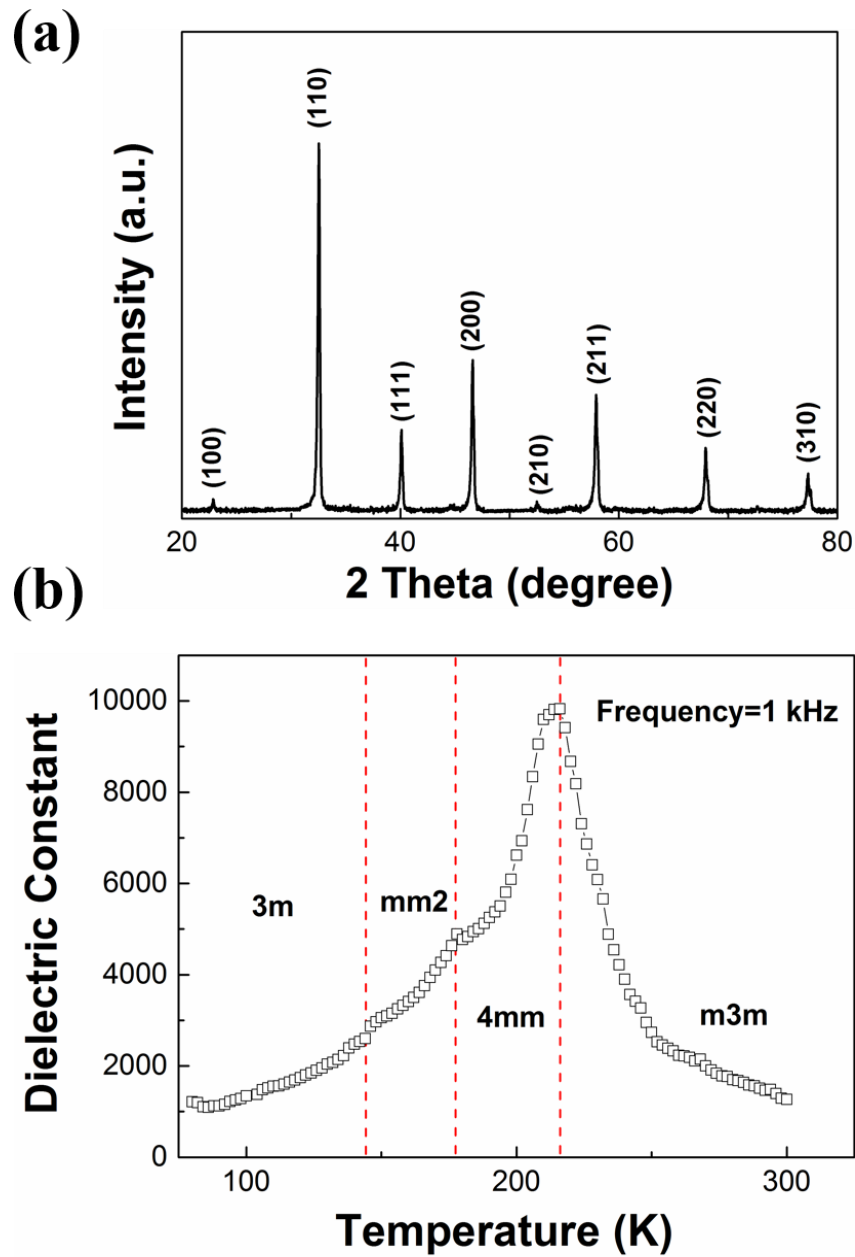


Figure 3.8 (a) XRD pattern of Ni²⁺-doped BST powder in the 2θ scan range of 20 to 80°. (b) Temperature dependent dielectric constant of Ni²⁺-doped BST disc.

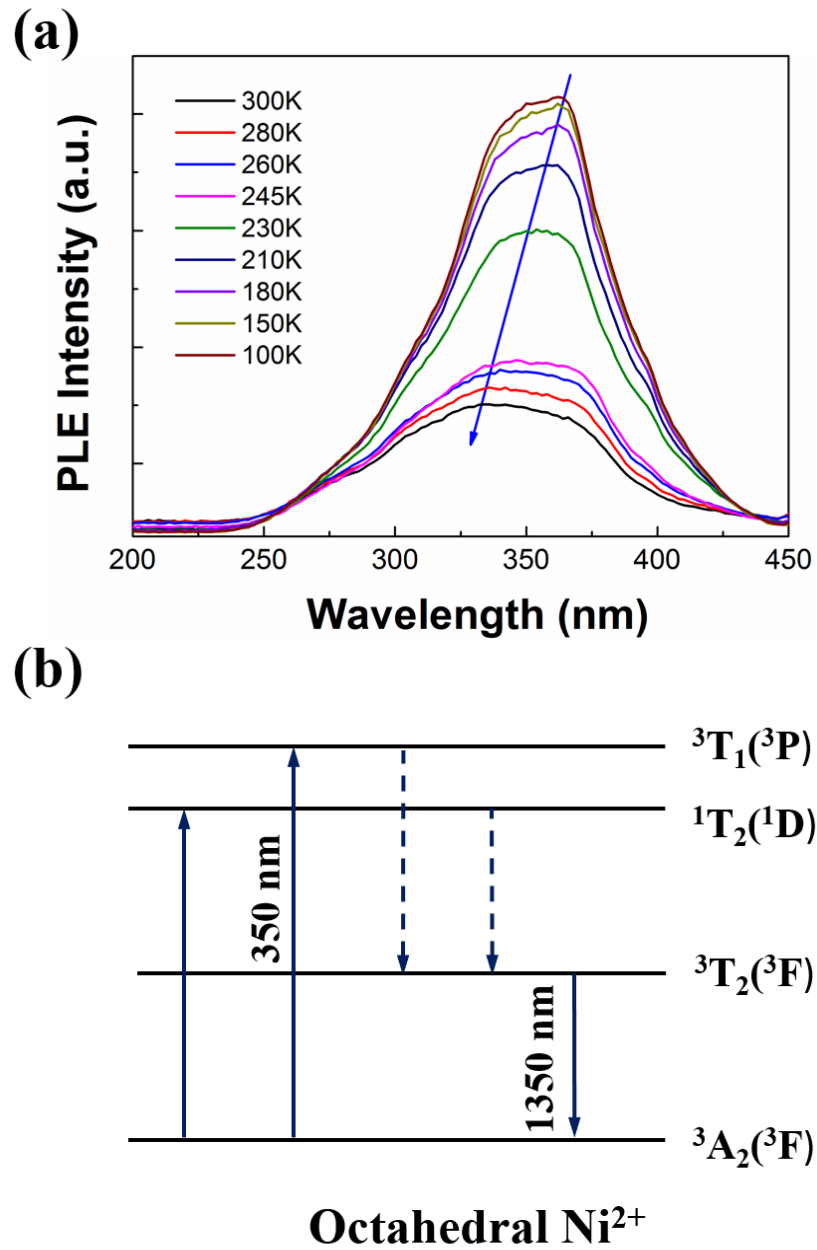


Figure 3.9 (a) Temperature dependent PLE spectra of Ni²⁺-doped BST disc, $\lambda_{em}=1350$ nm. (b) Energy levels and transitions of Ni²⁺ in octahedral sites.

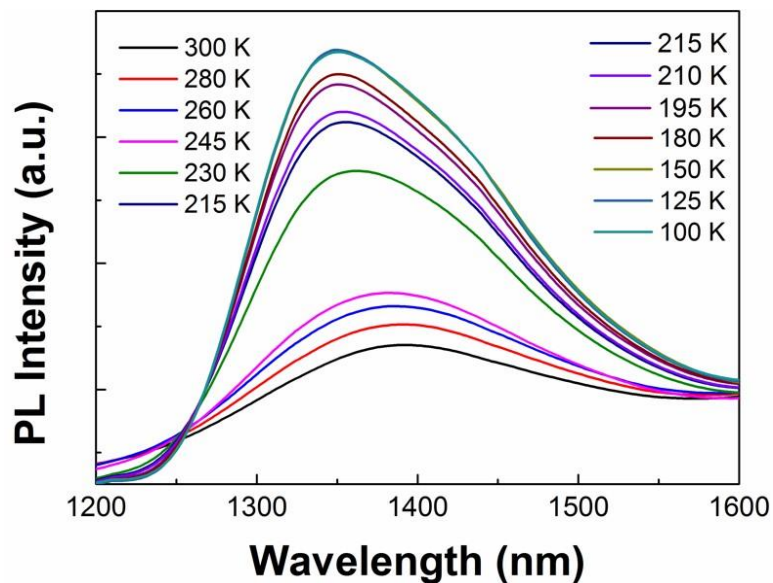


Figure 3.10 Temperature dependent PL spectra of Ni^{2+} -doped BST disc, $\lambda_{\text{ex}}=350$ nm.

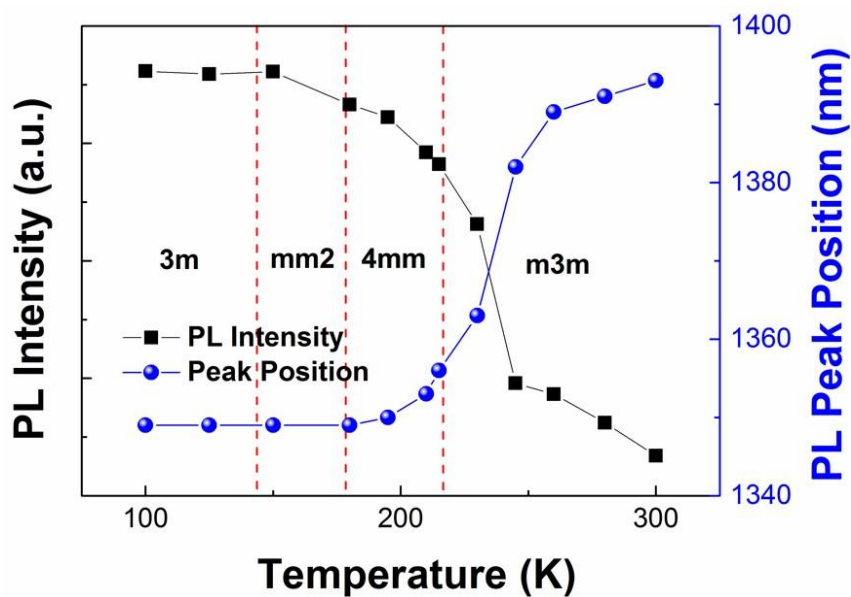


Figure 3.11 PL intensity and peak position of Ni^{2+} -doped BST disc as a function of

temperature changed from 100 K to 300 K.

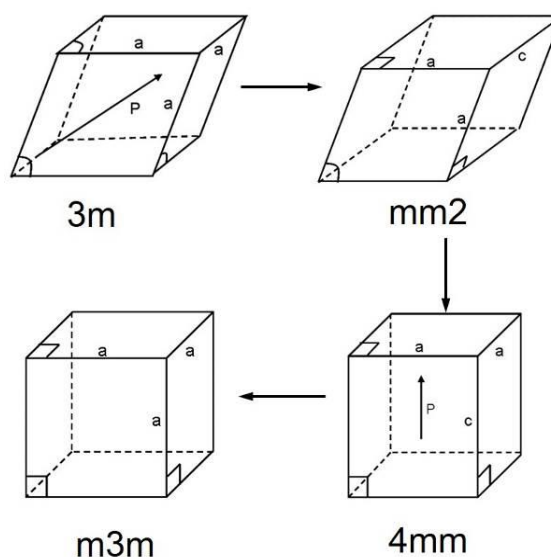


Figure 3.12 Phase transition of Ni^{2+} -doped BST.

Temperature dependent NIR PLE spectra of Ni^{2+} -doped BST sample are shown in Figure 3.9 (a). The PLE spectra were measured by monitoring emission peak at 1350 nm. The most intensive excitation band of BST sample is placed at about 350 nm, which can be ascribed to spin-allowed ${}^{\text{VI}}\text{Ni}^{2+}: {}^3\text{T}_1({}^3\text{P}) \rightarrow {}^3\text{A}_2({}^3\text{F})$ [Figure 3.9 (b)]. With the increment of temperature, the excitation peak displays a slight blue shift, expanding the spectral range of 250 to 450 nm. It matches well emission band of UV LEDs (250-400 nm). For that reason commercial UV LED can be used as potential excitation sources. Temperature dependent NIR PL spectra were measured when pumped at 350 nm [Figure 3.10]. The resultant emission spectra are dominated by



broaden bands (1200 to > 1600 nm) which place at about 1350 nm. In particular, FWHM of these bands goes beyond 200 nm. The PL results do not appear beyond 1600 nm due to the low spectral response of the InGaAs detector at around 1600 nm. NIR PL originates from the spin-allowed relaxation of ${}^VI\text{Ni}^{2+}:{}^3\text{A}_{2g}({}^3\text{F})\rightarrow{}^3\text{T}_{1g}({}^3\text{P})$ [Figure 3.9 (b)] and expands the whole optical communication window (O-L bands). As presented in Figure 3.11, integrated intensity and position of PL bands stay unchanged when temperature is below 150 K. The variations of PL intensity and peak position are very minor when temperature is below 180 K. With increasing temperature from 180 K to 210 K, the PL intensity gradually drops and the emission peak displays a visible redshift. Around 230 K, both PL intensity and position existent a remarkable change. And then the emission intensity declines continually and the PL peak red shifts gradually by raising temperature progressively. Meanwhile, FWHM apparently becomes broaden when temperature rises above 230 K [Figure 3.10]. Remarkably, unlike the significant decrease in the emission intensity previously reported in Ni^{2+} -doped glass [Suzuki, 2004], the PL intensity of our samples at 300 K is still about 50 % as intense as that at 100 K, suggesting less thermal quenching in Ni-doped BST ceramics at room temperature. Differing from Ni^{2+} -doped glass ceramics [Gao, 2012], a redshift occurs as the increment of temperature, namely from 1350 nm at 100 K to 1393 nm at 300 K. Considering the above discussion in Figure 3.8 (b), the NIR PL revolution could be finely explained by the phase evolutions of Ni^{2+} -doped BST under dissimilar temperature. As presented in Figure 3.12, under 144 K, the phase of Ni^{2+} -doped BST sample retains

rhombohedral (3m), without PL variation. With raising temperature from 144 K to 178 K, the phase preserving orthorhombic (mm2), the PL intensity slightly shrinkages and emission peak position almost unchanges. The slight PL change below 178 K can be ascribed to little crystal field revolution when phase change from rhombohedral (3m) to orthorhombic (mm2). When growing temperature from 178 K to 300 K, the PL peak position shows a red shift, owing to the weaken crystal field around Ni^{2+} ions [Bai, 2014]. The shrinking PL intensity could be attributed to the enhanced temperature dependent nonradiative relaxation [brik, 2006]. In particular, significant emission variation around T_c is owing to the phase transition from tetragonal (4mm) to cubic (m3m). Consequently, the luminescence behaviours of Ni^{2+} ions could be used to indicate the phase transition of BST.

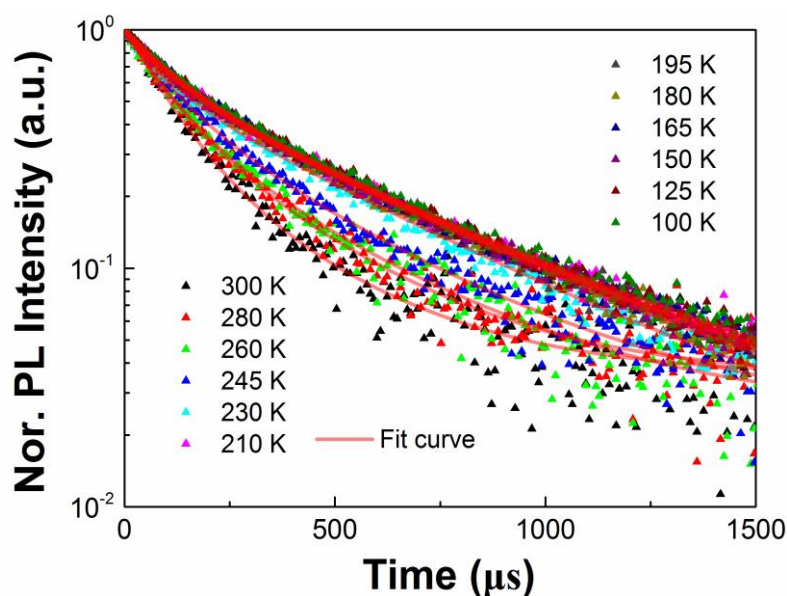


Figure 3.13 PL decay curves of Ni^{2+} -doped BST disc at different temperature,



$\lambda_{\text{ex}}=350$ nm and $\lambda_{\text{em}}= 1350$ nm.

The temperature dependent on normalized NIR PL decay curves are shown in Figure 3.13, measuring emission intensity at 1350 nm under the excitation at 350 nm. Here, none of the decay curves seem to follow a single exponential equation. It is deduced that non-exponential characteristic of the decay curve of Ni^{2+} -doped BST might attribute to the difference of environment surrounding Ni^{2+} ions since the BST micro crystal sizes generally not the same [Wu, 2008]. When the temperature is below 230 K, the PL decay slightly differs. It can be deduced to the weak electron-phonon coupling [Brik, 2006] and nonradiative relaxation when temperature below T_c . The PL decay gradually gets rapid when temperature raising from 230 K to 300 K. This suggests that decay of Ni^{2+} -doped BST is more sensitive to temperature in cubic (m3m) phase. Internal quantum efficiency η of the NIR PL process at temperature $T = x$ can be obtained from $\eta_{T=x} = (\tau_x / \tau_{5\text{K}}) \times 100$, where τ_x is the experimental lifetime as obtained at temperature x and $\tau_{5\text{K}}$ is the extrapolated lifetime at 5 K [Gao, 2012]. For the prepared sample at ambient temperature ($x = 300$ K), a value of $\eta = 49\%$ was obtained. The effective lifetime τ can be acquired from Figure 3.13 when the emission intensity falls to $1/e$ of its initial value. τ at 100 K was found about 327 μs . Its value decreases to 160 μs at 300 K, due to temperature dependent nonradiative relaxation in ${}^{\text{VI}}\text{Ni}^{2+}: {}^3\text{A}_{2\text{g}}({}^3\text{F}) \rightarrow {}^3\text{T}_{1\text{g}}({}^3\text{P})$. The measured lifetime (160 μs) at 300 K is much longer than that of Ni^{2+} -doped Ba-Al titanate glass ceramics (39 μs) [Gao, 2012]. The longer lifetime is beneficial for application

in mode locked lasers.

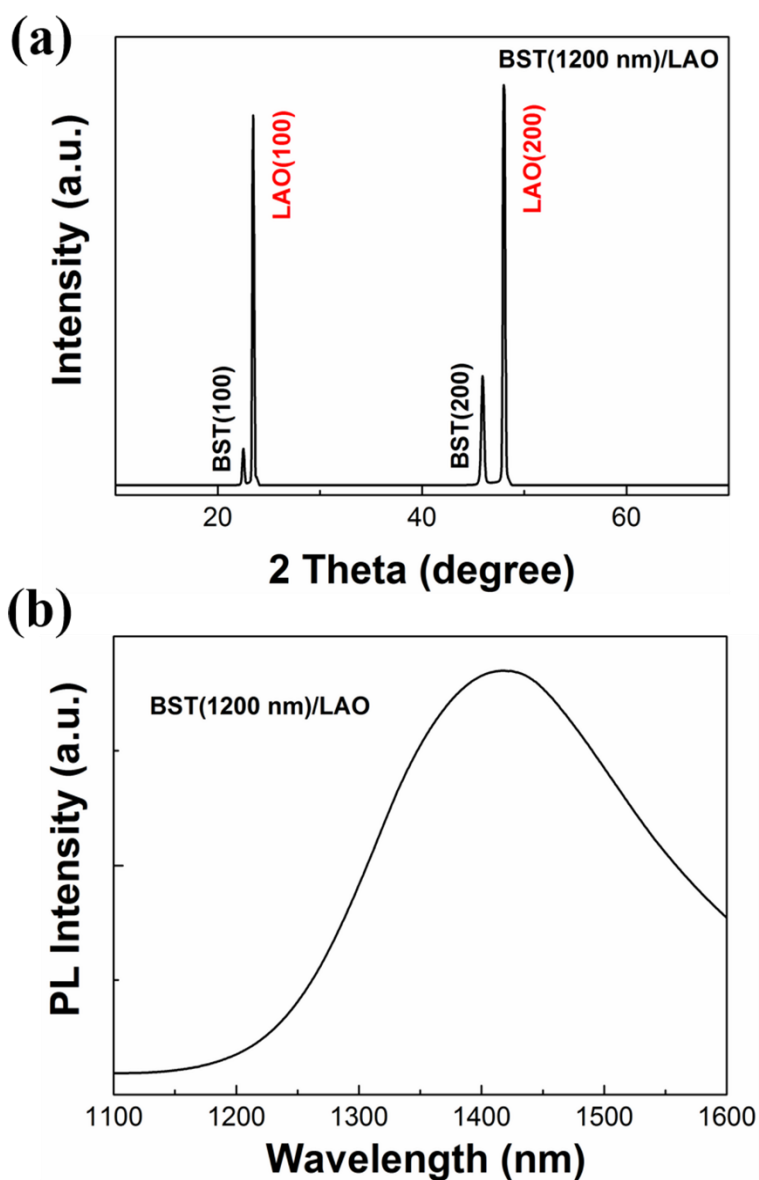


Figure 3.14 (a) XRD pattern of Ni^{2+} -doped BST(1200 nm)/LAO sample. (b) PL spectrum of Ni^{2+} -doped BST(1200 nm)/LAO sample.



In the above experiments, ultrabroadband NIR PL is demonstrated in BST ceramics. Compared with bulk materials, the utilization of a thin film structure facilitates the fabrication and integration of photonic devices.²² Figure 3.14 (a) shows XRD pattern of as-prepared Ni²⁺-doped BST thin film (1200 nm) grown on LAO substrate. It is known that LAO can be widely utilized as substrate to fabricate dielectric and ferroelectric thin films.²³ In the θ - 2θ scan, only BST (100), (200) and LAO (100), (200) peaks were observed. No other peaks were present. This indicates that the Ni²⁺-doped BST thin film is highly oriented grown on (100) LAO substrate. Figure 3.14 (b) presents the NIR PL spectrum of Ni²⁺-doped BST(1200 nm)/LAO sample at room temperature, under 350 nm excitation. The NIR emission band peaks locate at about 1418 nm, with a broad width (FWHM) exceeding 260 nm. The ultrabroadband NIR emission covers the whole telecommunication window. The result suggests that the developed Ni²⁺-doped BST/LAO is potentially promising for various applications as a broadband gain medium for optical amplifier and optoelectronic integrated devices.

3.2.4 Conclusion of Ni²⁺-doped BST

In conclusion, ultrabroadband NIR luminescence from Ni²⁺-doped BST is observed. With the increment of temperature, the luminescence properties are affected by phase transition induced crystal field change as well as temperature dependent nonradiative relaxation. Ni²⁺ ions can be a potential probe for the crystal structure at low temperature (below 230 K). The broadband NIR PL expands optical



communication band from 1200 nm to > 1600 nm, with a bandwidth greater than 200 nm. The excited state lifetime of $^1\text{Ni}^{2+}:^3\text{T}_2(^3\text{F})$ was found to be 327 μs at 100 K and 160 μs at 300 K. In addition, ultrabroadband NIR luminescence was also observed in Ni^{2+} -doped BST thin film at ambient temperature. The presented results suggest that Ni^{2+} -doped BST is promising for widespread applications in broadband optical amplifier and optoelectronic integrated devices.



3.3 Ni²⁺-doped barium strontium titanate thin films with broadband NIR luminescence

In this section, Ni²⁺-doped perovskite thin films have been prepared by PLD. The prepared materials show ultrabroadband NIR luminescence from 1100 nm to over 1600 nm, covering the whole optical telecommunication. The peak position of the NIR emission can be finely tuned and the total shift of 282 nm was observed. On the other hand, fixed the chemical composition, tunable PL can be achieved by depositing on different wafers.

3.3.1 Background of barium strontium titanate thin films

Recently, Ba_{1-x}Sr_xTiO₃ (BST-*x*) thin films have received great attention for their applications such as room-temperature pyroelectric infrared detectors, phase shifters, and high-density dynamic random access memories [Cao, 2006]. In such devices, the chemical composition significantly influence the dielectric and optical properties of the films. Particularly, active ions doped barium strontium titanate has drawn great attention for its simultaneous ferroelectric and optical properties [Gao, 2011; Zhou, 2012], suggesting attractive applications in multifunctional optoelectronic devices [Ang, 2001; Hao, 2000]. Recently, our research group reported tunable and ultrabroadband NIR luminescence from Ni²⁺-doped ferroelectric perovskites [Bai, 2014]. Chemical substitution-induced exceptional emitting-wavelength tuning has been demonstrated. In this section, Ni²⁺-doped BST-



x thin films grown on different wafers will be studied.

3.3.2 Ni-doped thin-film sample preparation and measurements

The BST- x :Ni ceramic targets were prepared by solid state chemical reaction method. Analytical grade BaCO₃, SrCO₃, TiO₂ and NiO powders were used as starting materials. The ceramic bulk was prepared according to the molecular formula Ba _{x} Sr_{1- x} Ti_{0.995}Ni_{0.005}O₃, $x=0, 0.5, 0.7$ and 1. Here the Ni²⁺ ions were substituted at the Ti⁴⁺ sites, and the charge neutrality could be maintained by the formation of oxygen vacancies. The starting powders with designed stoichiometric amounts were ball milled for 24 h, then dried and calcined at 1100 °C for 8 h in air. After the calcination, the resulting powders were pressed into disk samples and sintered at 1350 °C for 4 h in air. The as-prepared targets were used for depositing BST:Ni thin films. The BST:Ni films were grown on (001)-oriented Si wafer with a (111)-oriented Pt buffered layer (Pt-Si substrate) by pulsed laser deposition (PLD). The SrTiO₃:Ni (STO:Ni) films were grown on SrTiO₃ (001), LaAlO₃ (001), and MgO (001) substrates. Figure 15 presents the photographs of the target and the prepared films. The film thickness is determined from cross-section of the specimen using scanning electron microscope. The targets were ablated by a KrF excimer laser (wavelength 248 nm) with a frequency of 5 Hz and a laser pulse energy density of 5 J•cm⁻². The growth temperature and oxygen pressure were fixed at 700 °C and 20 Pa.

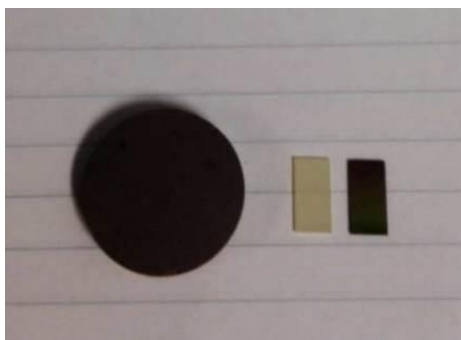


Figure 3.15 Photographs of STO bulk target (Left), Ni^{2+} -doped STO thin films grown on LAO and Pt-Si wafer (Right).

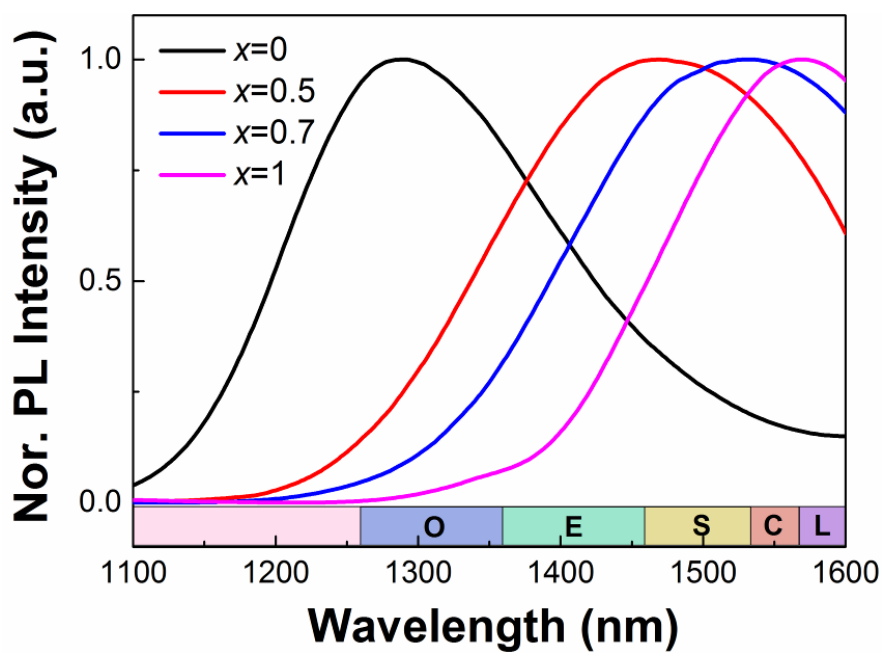


Figure 3.16 Normalized PL spectra of Ni^{2+} -doped BST- x thin films grown on Pt-Si wafer, $\lambda_{\text{ex}}=325$ nm.

The PL emission and PLE spectra were recorded using an Edinburgh FLSP920 spectrophotometer equipped with a He-Cd laser and a Xe lamp. The decay curves were recorded with a pulsed 60 W Xe flashlamp. The crystal structures of the obtained films were examined by a Bruker D8 Discover X-ray diffractometer. All the measurements were carried out at room temperature.

3.3.3 Ni²⁺-doped ferroelectric thin films with broadband NIR luminescence

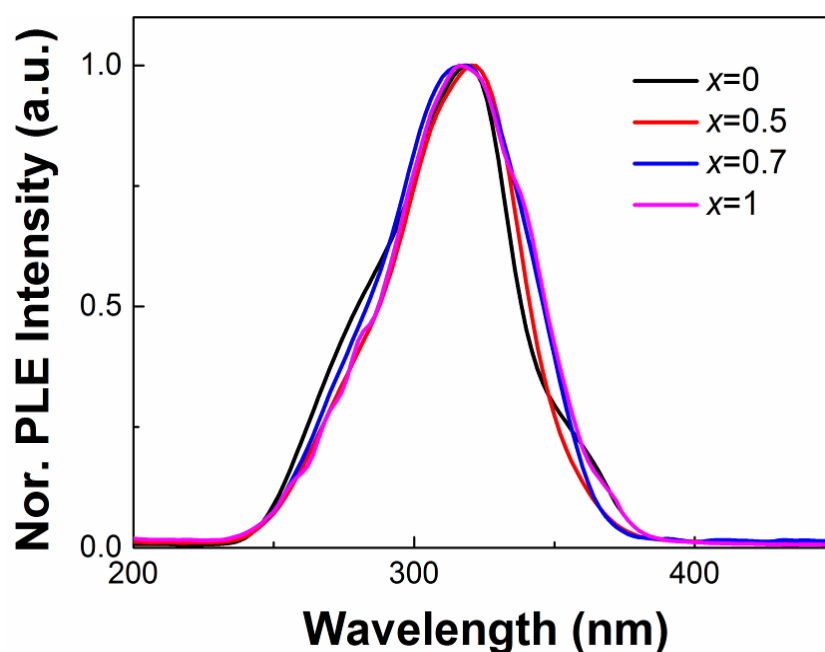


Figure 3.17 PLE spectra of Ni²⁺-doped BST-*x* thin films grown on Pt-Si wafer.

Figure 3.16 displays normalized NIR PL spectra of BST-*x*:Ni (*x*=0, 0.5, 0.7 and 1) thin films with 300 nm thickness grown on Pt-Si substrates under 325 nm excitation. Compared with traditional Er-doped perovskite oxide film [Zhang, 2000],



all the BST- x :Ni film samples exhibit ultrabroadband NIR emission with FWHM over 200 nm, covering the whole optical communication window including O, E, S, C, and L bands, implying that BST- x :Ni film is promising for NIR integrated optics. The observed NIR PL can be assigned to spin-allowed $\text{Ni}^{2+}:^3\text{T}_2(^3\text{P}) \rightarrow ^3\text{A}_2(^3\text{F})$. Notably, with the increment of x value increasing from 0 to 1, the NIR emission bands from BST- x :Ni thin films show an obvious red shift, the luminescent peak shifts from 1287 nm to 1569 nm. The tunable range can reach 282 nm, which is larger than that in bulk ceramics. The exceptional tunable emission can be explained by the crystal field change induced by chemical composition, as discussed in section 3.1. The PLE spectra of the BST- x :Ni thin films measured by monitoring PL at emission peak are presented in Figure 3.17. All the excitation bands are located at around 325 nm, which is consistent with the pumping wavelength of He-Cd laser used in our PL measurement.

The normalized NIR PL decay curves of the BST- x :Ni film samples are presented in Figure 3.18, where PL intensity at the emission peak was recorded under the excitation at 325 nm. With increasing x value, the PL decay gradually becomes rapid. The effective lifetime τ can be derived from Figure 3.18 when the emission intensity decreases to $1/e$ of its initial value. The τ decreases from 910 μs to 30 μs , corresponding to the film samples from STO to BTO film.

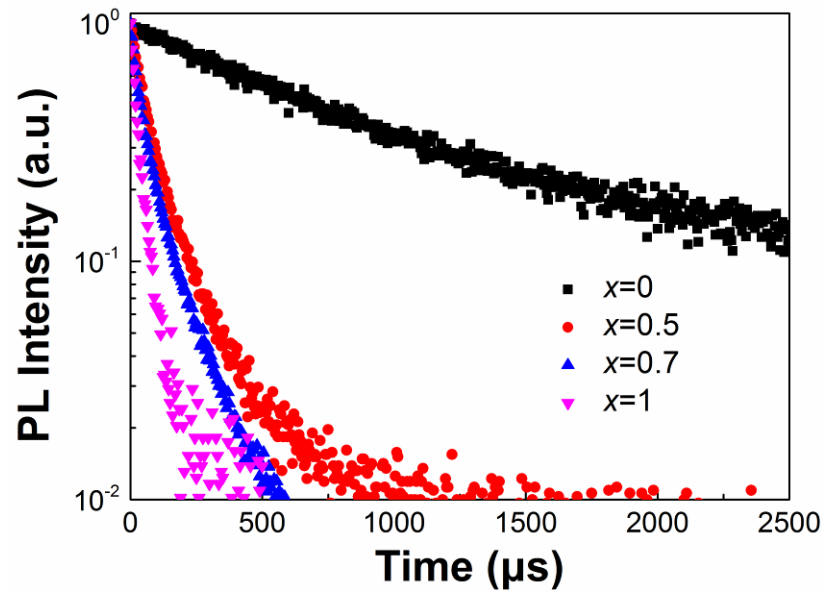


Figure 3.18 Decay curves of Ni²⁺-doped BST-*x* thin films.

Raman spectra of BST-*x*:Ni thin films are presented in Figure 3.19. The Raman spectrum in SrTiO₃ film is completely second-order in the cubic perovskite structure. The appearance of first-order Raman lines of 174, 540 and 793 cm⁻¹ in STO:Ni thin film, indicates a lower crystal symmetry induced by doping Ni²⁺ and defects and the Raman selection rule was relaxed in comparison with SrTiO₃ bulk [Lee, 2005]. As *x* increases from 0 to 1, all the modes at 237, 337, (540, 614) and 793 cm⁻¹ downshift to 234, 305, 519 and 720 cm⁻¹, respectively. In single crystal SrTiO₃, the second-order Raman lines at 243, 283 and 615 cm⁻¹ shift downward when the temperature approaches T_C. We attributed the mode softening in BST-*x*:Ni thin films to enhancement of the tetragonality *c/a* with increasing Ba concentration.

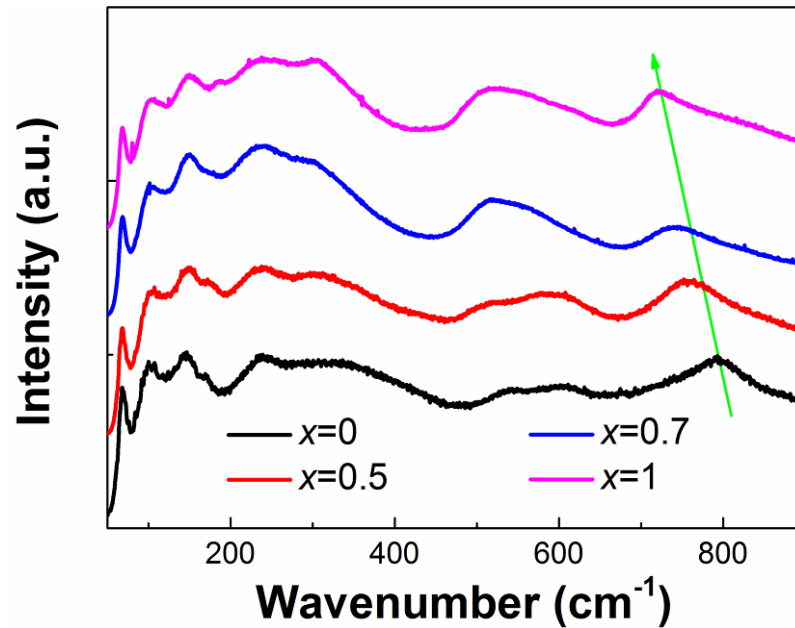


Figure 3.19 Raman spectra of Ni²⁺-doped BST-*x* thin films.

3.3.4 Ni²⁺-doped SrTiO₃ thin films with broadband NIR luminescence

According to the former results, STO:Ni sample possesses the longest effective lifetime, the strongest emission intensity, and the shortest emitting-wavelength (telecommunication O band), among Ni²⁺-doped BST samples. Hence the STO:Ni films were grown on STO (001), LAO (001), and MgO (001) substrates by PLD. Figure 3.20 shows XRD pattern of as-prepared Ni²⁺-doped STO thin film (600 nm) grown on LAO substrate. In the θ - 2θ scan, only STO (100), (200) and LAO (100), (200) peaks were observed. No other peaks were present. This indicates that the Ni²⁺-doped STO thin film is highly oriented grown on (100) LAO substrate.

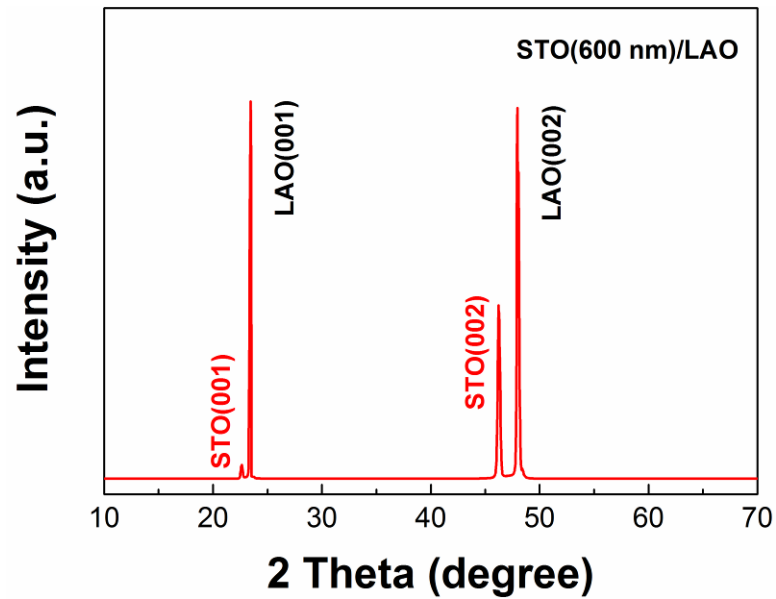


Figure 3.20 XRD pattern of Ni^{2+} -doped STO grown on LAO in the 2θ scan range of 20 to 80°.

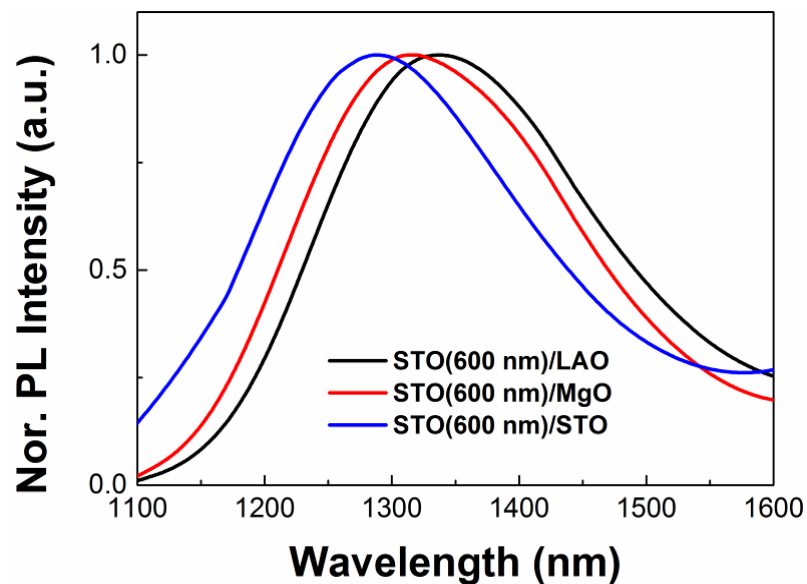


Figure 3.21 PL spectra of Ni^{2+} -doped STO thin films grown on different substrates,



$\lambda_{ex}=325$ nm.

Figure 3.21 presents the normalized NIR PL spectra of STO:Ni thin film (600 nm) grown on different substrates, including (001)-oriented STO, LAO and MgO wafers, under 325 nm excitation at room temperature. All the STO:Ni film samples exhibit ultra-broadband NIR emission with FWHM exceeding 260 nm, covering the optical communication window between 1260 nm and 1600 nm, implying that STO:Ni film is promising for NIR integrated optics. The observed NIR PL can be assigned to spin-allowed $Ni^{2+}:^3T_2(^3P) \rightarrow ^3A_2(^3F)$. Notably, the emission peaks are different as well as the variation in substrates. The luminescent centers at 1288 nm of STO:Ni thin film grown on STO (001) wafer downshift to 1315 (grown on MgO (001) wafer) and 1338 nm (grown on LAO (001) wafer), respectively. Considering the different lattice constants of the used wafers, misfit strain induced by the substrate leads to the change in the crystal field around Ni^{2+} . The detail mechanism will be discussed in the following chapter.

3.3.5 Conclusion of Ni^{2+} -doped barium strontium titanate thin films

In conclusion, tunable and ultrabroadband NIR luminescence from Ni^{2+} -doped ferroelectric perovskites oxides thin films is demonstrated. Ultrabroadband NIR luminescence of the prepared materials covers optical communication band from 1100 nm to over 1600 nm, with FWHM exceeding 200 nm. With the increase in Ba concentration of Ni^{2+} -doped BST-*x* thin films, the crystal field becomes weaker, and



the peak position of NIR emission is greatly changed from 1287 nm to 1569 nm, while the effective lifetime τ decreases from 910 μs to 30 μs . In addition, fixed the composition of STO:Ni thin film, tunable NIR luminescence is demonstrated through change the deposited wafer. The luminescence properties are affected by the misfit substrate induced crystal field change. The presented results make Ni²⁺-doped BST-*x* promising for widespread applications in broadband optical amplifier and optoelectronic integrated devices.



Chapter 4 Strain-Induced Modification of NIR Luminescence of SrTiO₃:Ni²⁺ Thin Films

In chapter 3, chemical substitution-induced emission modulation in Ni²⁺-doped ferroelectric oxides BST-*x* has been observed. Ni²⁺ doped SrTiO₃ (STO:Ni) possesses cubic structure, the most intensive NIR emission, and longest effective lifetime. In this chapter, differing from conventional chemical approach, tunable NIR luminescence of STO:Ni thin film grown on piezoelectric Pb(Mg_{1/3}Nb_{2/3})_{0.7}Ti_{0.3}O₃ (PMN-PT) substrate via strain engineering will be studied. Through controlling the thickness of STO:Ni film, the misfit strain dependent emission has been studied. Moreover, the modulation of strain can be controlled under an external electric field via converse piezoelectric effect of PMN-PT used in this work.

4.1 Introduction of tunable luminescence

Luminescent materials with tunable ability are highly desirable, since they have potential applications in controlling and processing light for active components of light sources, optical waveguides, and biomedicine [Blasse, 1994; Wang, 2012; Zhang, 2013]. In principle, optically active materials with tunable emission are usually achieved through chemical approaches, namely changing doping ions [Wang, 2008] or compositions of host materials [Hao, 2005]. However, the tuning of PL by



chemical way is essentially an *ex-situ* and irreversible process. Therefore, it is unlikely to know the kinetic process how the luminescence changes with structural symmetry and crystal field through the conventional approach. Moreover, it is almost impossible to isolate the pure crystal field effect from the other extrinsic effects present in different samples, such as chemical inhomogeneities and defects. Therefore, it is interesting to investigate whether the tuning of luminescence can be achieved by various external stimuli, such as magnetic-field [Liu, 2013], electric-field [Hao, 2011], and strain [Chen, 2011]. Particularly, large misfit strain can exist in thin films when one material is deposited on another, resulting from differences in crystal lattice parameters and thermal expansion coefficients between the grown film and underlying substrate or arising from defects formed during film deposition [Choi, 2004; Schlom, 2007]. Therefore, the available configurational space for luminescent thin films includes additional degree of freedom, i.e. strain which can be considered to tune luminescence. In earlier reports, misfit strain induced tunable luminescence has been observed in some material systems, such as semiconductor thin films grown on various substrates [Aumer, 2000; Ohkawa, 1988]. The strain has an influence on the bound-exciton and band-edge related photoluminescence in these semiconductor thin films such as ZnO film [Zheng, 2012]. Note that a large group of commonly used luminescent material is so-called metal-ion doped phosphor. Differing from the semiconductors, optical and luminescent characteristics of metal-ion doped phosphors are mainly dominated by the energy transitions of metal-ion dopants (lanthanide, transition metal, etc.), and crystal field to some extent. Unfortunately,

there is lack of research on the metal-ion doped thin film structures with tunable luminescence under strain. Therefore, it is very interesting to investigate the strain effects on the luminescent properties of the metal-ion doped thin films.

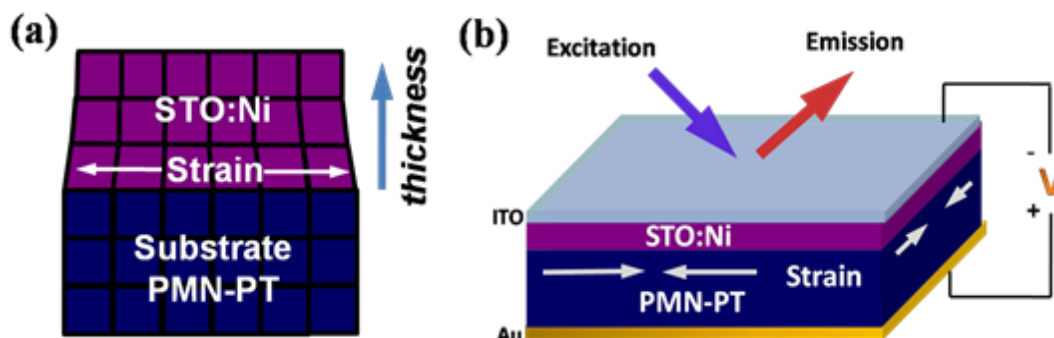


Figure 4.1 (a) Schematic of strained thin film of STO:Ni grown on PMN-PT. (b) The setup used for measuring the NIR emission of STO:Ni/PMN-PT under an external electric field.

In this chapter, transition metal Ni^{2+} ion has been chosen as dopant in the studied luminescent thin films since the fluctuation of crystal-field strength may result in the modulation of the energy level between the ${}^3\text{T}_2$ and ${}^3\text{A}_2$ levels of Ni^{2+} ion [Brik, 2006]. Therefore, one expects that the luminescence of Ni^{2+} ions can be tuned by fine-tuning the crystal field strength under strain stimulus. Furthermore, in the view of applications, Ni^{2+} -doped phosphors are considered as one of promising candidates for tunable laser and broadband NIR optical amplifiers because of their promising ultra-broadband NIR emission [Zhou, 2009]. On the other hand, the host



of SrTiO₃ (STO) here is known as an incipient ferroelectric and foundational material of oxide-based heterostructures [Jiang, 2003]. STO thin films with tunable dielectric properties associated with structural phase transition under strain have been systematically studied [Hao, 2006, Zhai, 2006]. Our recent work indicates that STO is also a suitable NIR phosphor matrix for Ni²⁺ ions [Bai, 2014]. To prove the concept of tunable luminescence in STO:Ni under strain, we have proposed a strategy for tuning NIR luminescence of STO:Ni thin films as shown in Figure 4.1. Here single-crystal piezoelectric Pb(Mg_{1/3}Nb_{2/3})_{0.7}Ti_{0.3}O₃ (PMN-PT) is used as a substrate due to its large piezoelectric coefficients ($d_{33} > 2000$ pC/N) and high electromechanical coupling factors ($k_{33} > 0.9$), enabling one to apply large strains to the grown STO:Ni films. Therefore, two methods can be performed to investigate the strain effects on the luminescence of STO:Ni films. First, misfit strain can be controlled by depositing STO:Ni films with different thickness on PMN-PT substrate as shown in Figure 4.1 (a). Secondly, strain modulation can be carried out by external electric field via converse piezoelectric effect of PMN-PT as shown in Figure 4.1 (b). In contrast to conventional approach of applying strain, the latter one can offer an effective and precise way to control over a range of strain state of the thin films in real-time and *in situ* manner. Owing to the unique strain engineering of coupling between piezoelectric and luminescence, we have observed the controllable and reversible tuning of luminescence under strain in this report. Physical mechanism behind the novel observation is discussed. These results will aid further investigations of luminescence of metal-doped phosphors and optoelectronic



applications because the strain engineering provides an additional degree of freedom in the design of NIR luminescent materials.

4.2 Preparation and measurements of STO:Ni thin films

The STO:Ni ceramic target was synthesized by solid state chemical reaction method using analytical grade SrCO_3 , TiO_2 and NiO powders as starting materials. The ceramic bulk was prepared according to the molecular formula $\text{SrTi}_{0.995}\text{Ni}_{0.005}\text{O}_3$. Here the Ni^{2+} ions were substituted at the Ti^{4+} sites, and the charge neutrality could be maintained by the formation of oxygen vacancies. The prepared process of the target can be found in section 3.3.2. The prepared target showed a prominent SrTiO_3 crystalline phase in the XRD pattern. The STO:Ni films were grown on single crystalline $5\text{ mm} \times 3\text{ mm} \times 0.5\text{ mm}$ wafers of PMN-PT (001) by pulsed laser deposition. The film thickness is determined from cross-section of the specimen using scanning electron microscope. The target was ablated by a KrF excimer laser (wavelength 248 nm) with a frequency of 5 Hz and a laser pulse energy density of $5\text{ J}\cdot\text{cm}^{-2}$. The growth temperature and oxygen pressure were fixed at $700\text{ }^\circ\text{C}$ and 20 Pa. After the deposition, the STO:Ni films were *in situ* post-annealed at the growth temperature in 0.5 atm oxygen pressure for 10 min before they were cooled to room temperature. Conductive electrode of ITO transparent layer with 300 nm thickness was grown on the STO:Ni film at $300\text{ }^\circ\text{C}$ under 2.5 Pa oxygen pressure. Electrode of Au film was coated on the back of PMN-PT substrate.

The polarization of the PMN-PT substrate was performed using a Keithley 2410 Source Meter. The DC bias voltage applied on the samples was produced by the source meter. A Bruker D8 Discover X-ray diffractometer was used to record the crystal structures of the obtained films. The PL emission and PLE spectra were recorded using an Edinburgh FLSP920 spectrophotometer equipped with a He-Cd laser. The decay curves were recorded with a pulsed 60 W Xe flashlamp. All the measurements were carried out at room temperature.

4.3 Misfit strain induced tunable NIR luminescence

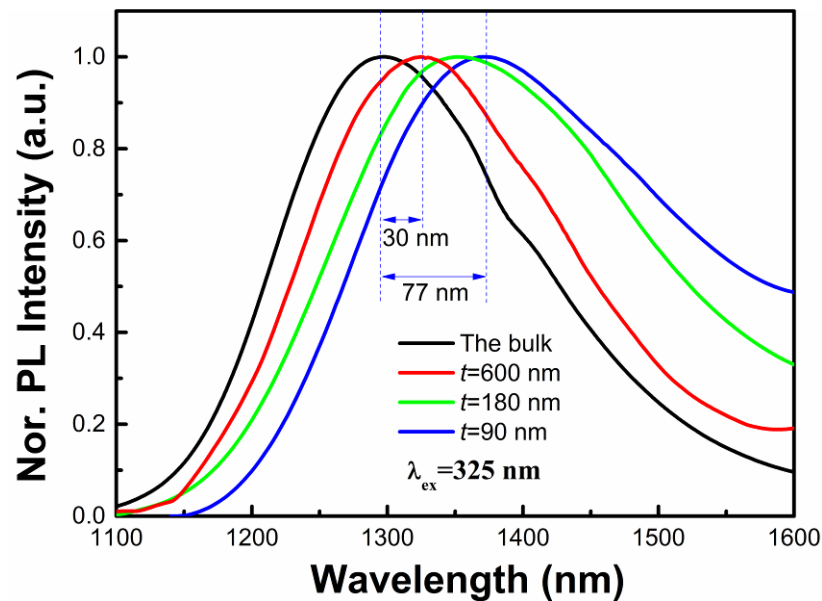


Figure 4.2 NIR PL spectra of STO:Ni thin films with different thickness (t) and ceramic bulk under 325 nm excitation.

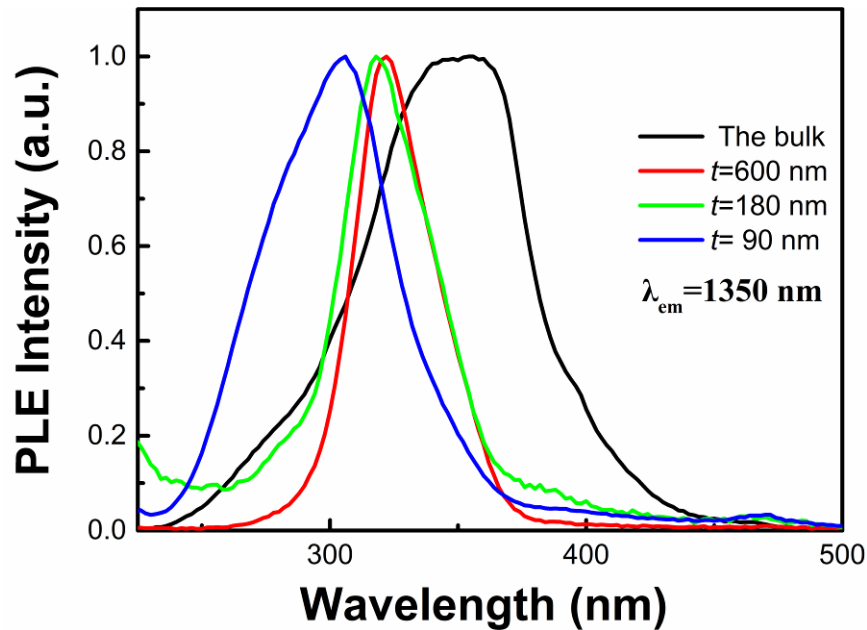


Figure 4.3 The PLE spectra of the STO:Ni samples.

Figure 4.2 shows NIR PL spectra of STO:Ni thin films and ceramic bulk target under 325 nm excitation. Compared with traditional Er-doped perovskite oxide film [Zhang, 2000], all the STO:Ni film samples exhibit ultra-broadband NIR emission, covering the optical communication window between 1260 nm and 1600 nm, implying that STO:Ni film is promising for NIR integrated optics. The observed NIR PL can be assigned to spin-allowed $\text{Ni}^{2+}:^3\text{T}_2(^3\text{P}) \rightarrow ^3\text{A}_2(^3\text{F})$. Notably, the luminescent FWHM of STO:Ni thin films under 325 nm excitation increases when decreasing film thickness. In addition, with the thickness of STO:Ni thin films increasing from 90 nm to 600 nm, the NIR emission bands from STO:Ni thin films show an obvious blue shift, the luminescent peak shifts from 1372 nm to 1325 nm. Compared with the

emission band from the ceramic bulk, the tunable range of luminescent peak can reach up to 77 nm, namely from 1372 nm to 1295 nm. The PL excitation (PLE) spectra of the STO:Ni samples measured by monitoring PL at emission 1350 nm are presented in Figure 4.3. All the excitation bands are located at around 325 nm, which is consistent with the pumping wavelength of He-Cd laser used in our PL measurement. Compared with the bulk, PLE bands of the STO:Ni thin films on PMN-PT are blue-shifted and narrow. With an increase in the film thickness, the excitation band of the films shifts towards that of the bulk.

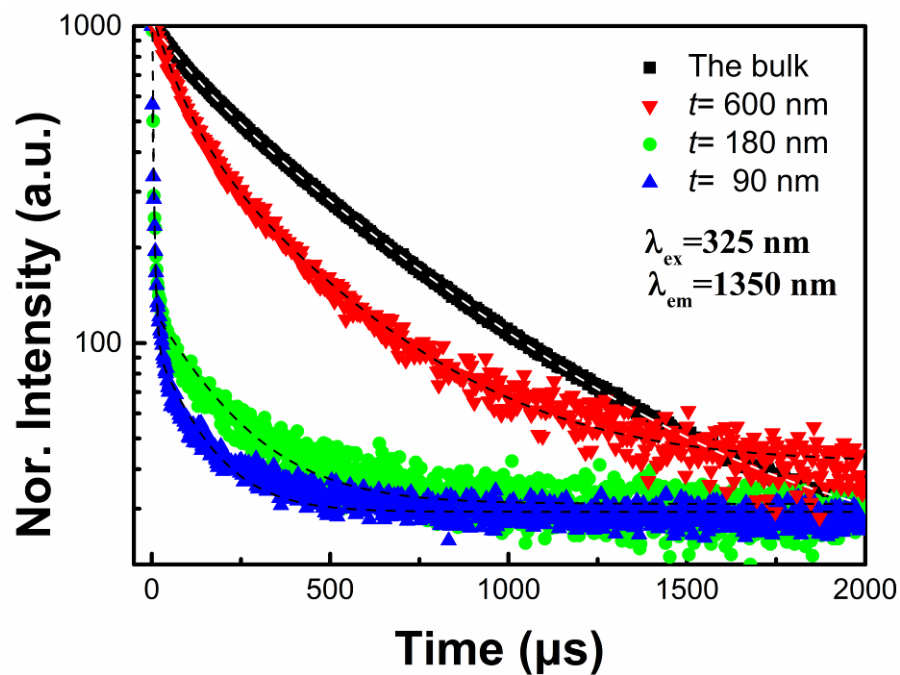


Figure 4.4 The normalized NIR PL decay curves of the STO:Ni samples.

The normalized NIR PL decay curves of the STO:Ni samples are presented in



Figure 4.4, where PL intensity at the emission of 1350 nm was recorded under the excitation at 325 nm. Compared to the bulk, the films show the fast decay of PL intensity. With decreasing the film thickness, the PL decay gradually becomes rapid. The effective lifetime τ can be derived from Figure 4.4 when the emission intensity decreases to $1/e$ of its initial value. Luminescent characteristics of the STO:Ni samples under 325 nm excitation, including τ , emission peak λ_{em} , and FWHM are summarized in Table 4.1. As film thickness increasing from 90 to 600 nm, the λ_{em} position shows a blue shift from 1372 nm to 1327 nm, while the λ_{em} of the bulk is located at 1295 nm. The τ decreases from 381 μ s to 4.5 μ s, corresponding to the samples from the ceramic bulk to the 90 nm thick film. Meanwhile, the value of FWHM increases from 220 nm to 315 nm accordingly.

Table 4.1 PL comparison of STO:Ni on PMN-PT and the ceramic bulk

Samples	Emission peak λ_{em} (nm)	τ (μ s)	FWHM (nm)
Ceramic bulk	1295	381	220
600 nm film	1327	194	228
180 nm film	1350	6	277
90 nm film	1372	4.5	315

To explain the observed PL results of STO:Ni film with different thickness and the corresponding bulk, some factors, such as substrate-induced strain, crystal field, and electron-phonon interaction of the prepared samples should be considered. As we know, bulk STO has a cubic structure with a lattice constant of $a=3.905 \text{ \AA}$ at 300



K, which is nearly 3.1 % smaller than that of PMN-PT. Therefore, the in-plane lattice constants in STO:Ni films are subject to lateral restraint from the PMN-PT substrate and hence do not have the freedom to change as bulk. As shown in Figure 1a, due to the mismatch lattice constant, one expects that the misfit strain in STO:Ni thin films to be tensile on PMN-PT. The lattice constant of STO:Ni thin film grown on PMN-PT is larger than the target. With increasing the thickness of STO:Ni thin film, the in-plane tensile strain decreases, the lattice constant of STO:Ni decreases as well according to the ligand field theory [Zhou, 2009; Tanabe, 1954], the splitting energies (Δ) of 3d orbitals of Ni²⁺ in octahedral (*o*) coordination can be derived from the following equation:

$$\Delta_o = 10Dq = Q \langle r^4 \rangle / R^5 \quad (4.1)$$

where Q is a constant, r represents the radius of the 3d orbital, and R is the distance between transition metal ions and ligands. Therefore, with the increase in film thickness, the lattice constant of STO:Ni gradually decreases, leading the shorten of Ni²⁺-O²⁻ bond distance R . The enhanced crystal field leads to the increase in splitting energy and therefore causes a blue shift of the corresponding luminescence. In addition, by considering the electron-phonon interaction, the coordinate configurational model in harmonic approximation can be used [Struck, 1974]. As shown in Figure 4.5, with increasing film thickness, the decrease of lattice parameter and distortion may lead to the reduction of E_{dis} and electron-phonon coupling.¹⁴ If the electron-phonon interaction is weak, the reduced non-radiative

transitions will result in the long emission lifetime as well as the narrow FWHM. Consequently, with the increase in film thickness, the luminescent performance of STO:Ni thin film approaches to that of the bulk. Additionally, the τ value of 600 nm film and bulk is much larger than that of 180 nm and 90 nm films. The thickness effect in the thin films is similar to the STO thin films reported by other group [Bao, 2001].

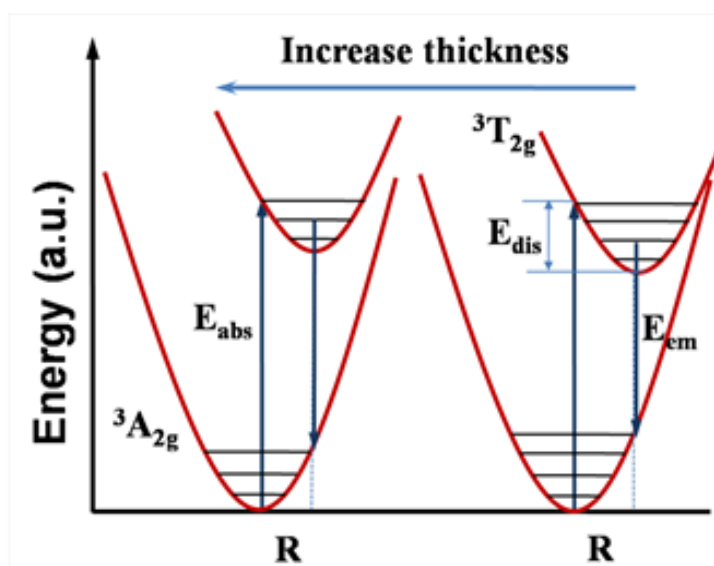


Figure 4.5 Configurational coordinate diagrams for STO:Ni samples. The lowest electronic states $^3A_{2g}$ are shown; Horizontal lines represent vibrational energy levels. The upward and downward arrows indicate absorption and emission transitions, respectively. R is the distance between Ni^{2+} ions and ligands. E_{dis} represents the difference between the excited state vibrational level reached in the absorption transition and the minimum level of the same state.

4.4 Piezoelectric-induced tunable NIR luminescence

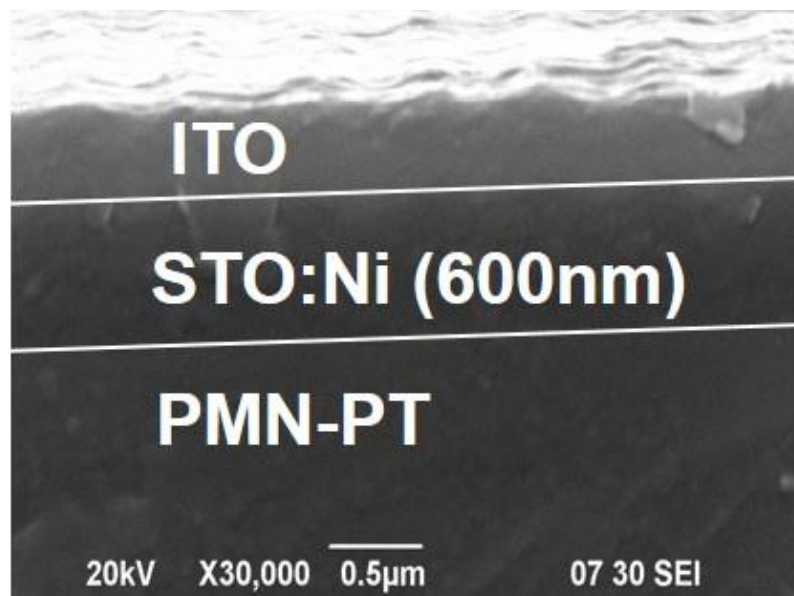


Figure 4.6 The SEM image of ITO/STO:Ni (600 nm)/PMN-PT.

Apart from the above misfit strain due to lattice mismatch between STO:Ni film and PMN-PT substrate, PMN-PT is capable of providing strain arising from converse piezoelectric effect. The recently developed method of electric-field controlled strain has previously been applied to modulate transport, magnetic, and optical behaviors of various material systems [Hui, 2013; Jie, 2013; Zhang, 2012]. Here, such a strategy can provide us a unique opportunity to *in situ* modulate the NIR PL of STO:Ni thin film in a real-time and reversible way. As discussed above, with the increase of thickness, the thickness dependent misfit strain in STO:Ni thin film gradually gets relaxed. The sample of STO:Ni (600 nm)/PMN-PT was

employed in this experiment, due to the smallest misfit strain existed in the thick STO:Ni film as a phosphor layer. The setup used for detecting the NIR emission of STO:Ni (600 nm)/PMN-PT under control of an external electric field is presented in Figure 4.1 (b). Light excitation and emission as well as applied electric field are denoted. Figure 4.6 presents the SEM image of ITO/STO:Ni (600 nm)/PMN-PT. The deposited thin films are dense and the surface is smooth.

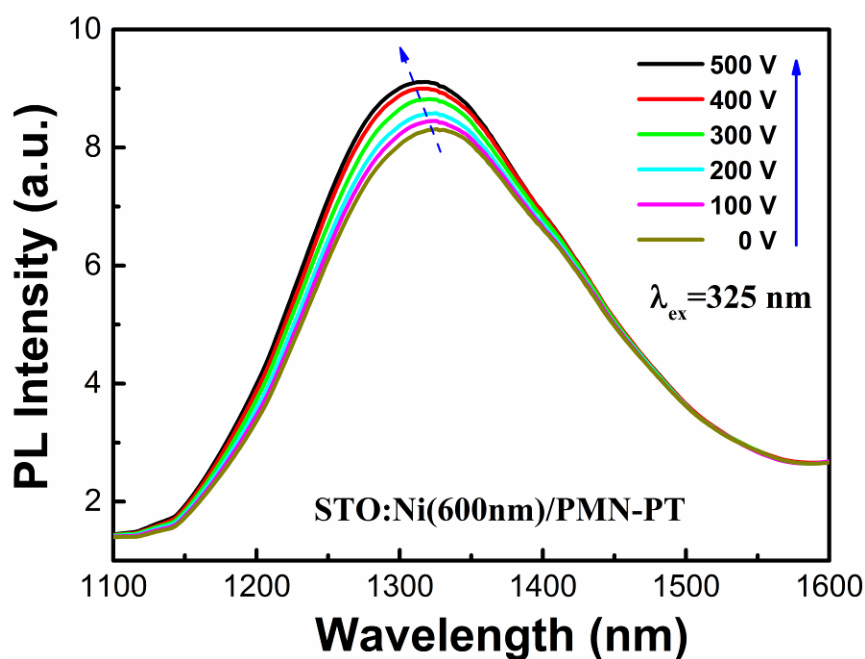


Figure 4.7 The PL spectra of STO:Ni (600 nm)/PMN-PT under 325 nm excitation, when DC bias voltage is applied from 0 to 500 V.

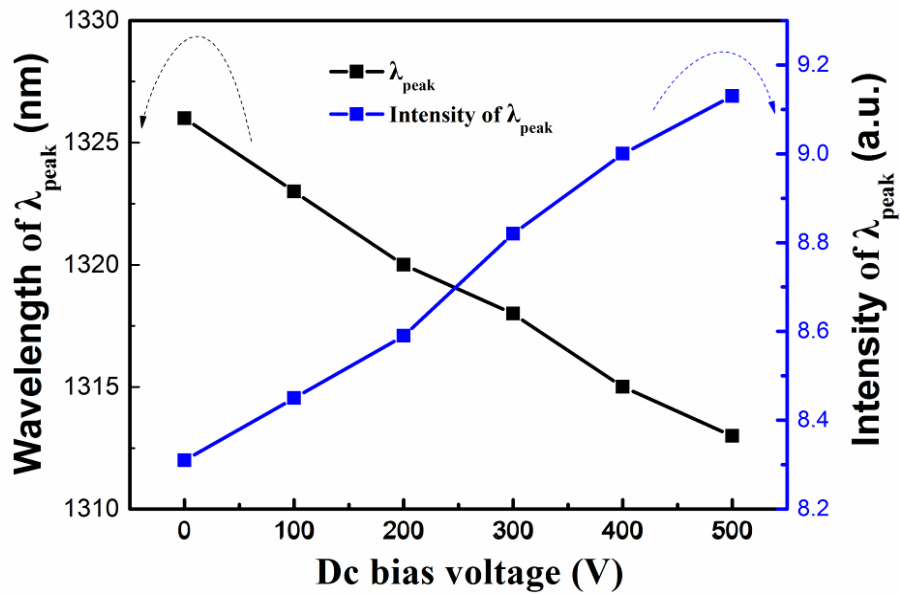


Figure 4.8 The summarized PL results of STO:Ni (600 nm)/PMN-PT.

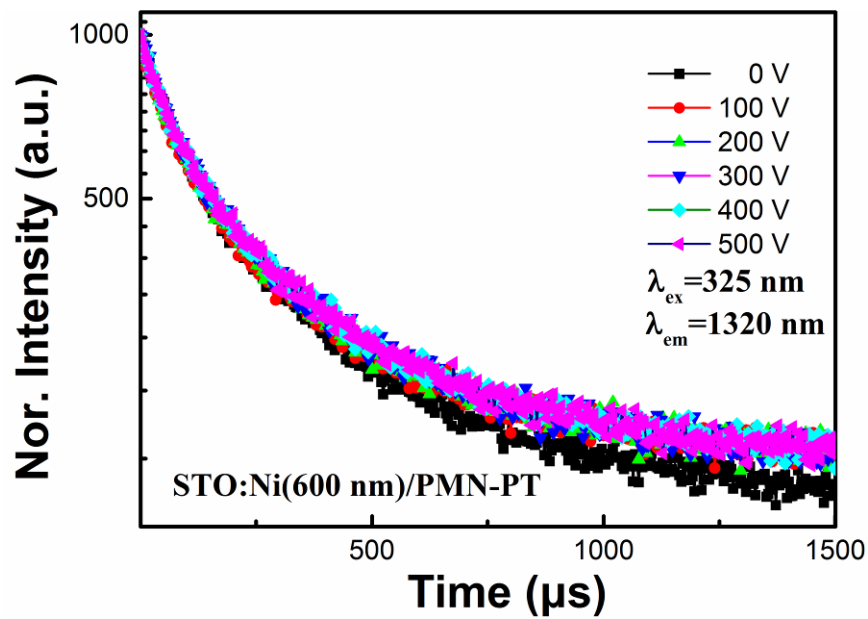


Figure 4.9 The NIR PL decay curves of STO:Ni (600 nm)/PMN-PT.

As shown in Figure 4.7, when increasing DC bias voltage from 0 V to 500 V, the emission peak position shows a blue shift from 1326 nm to 1313 nm, meanwhile the value of PL intensity gradually increases from 8.3 to 9.13. Interestingly, as summarized in Figure 4.8, with an increase in the applied voltage, both emission peak position and PL intensity change steadily. In addition, the NIR PL decay curves of STO:Ni (600 nm)/PMN-PT under 325 nm excitation are recorded, when DC bias voltage is applied. According to Figure 4.9, the PL decay slightly becomes slow as the voltage is increased from zero-bias state to 500 V.

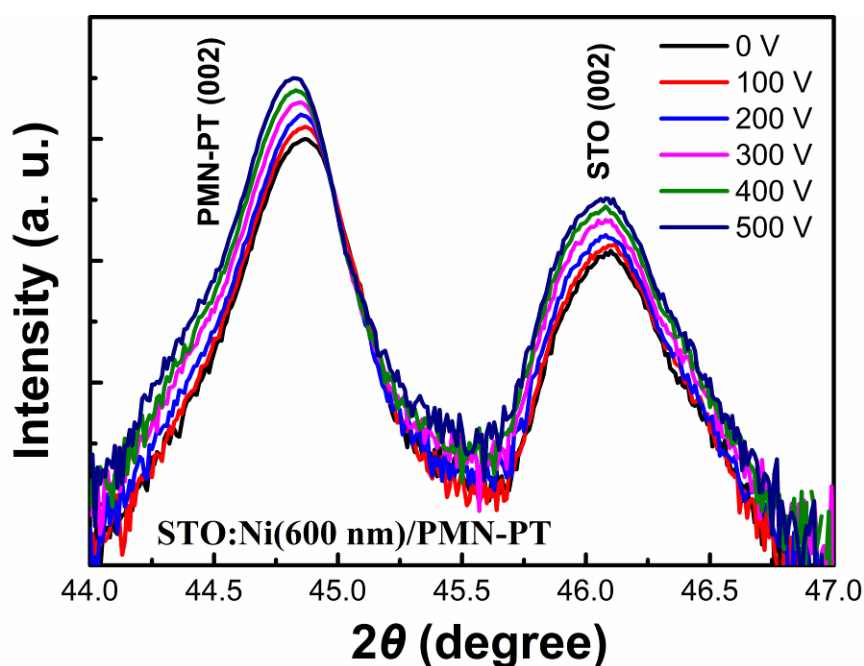


Figure 4.10 XRD patterns of STO:Ni (600 nm)/PMN-PT under DC bias voltage ranging from 0 to 500 V.

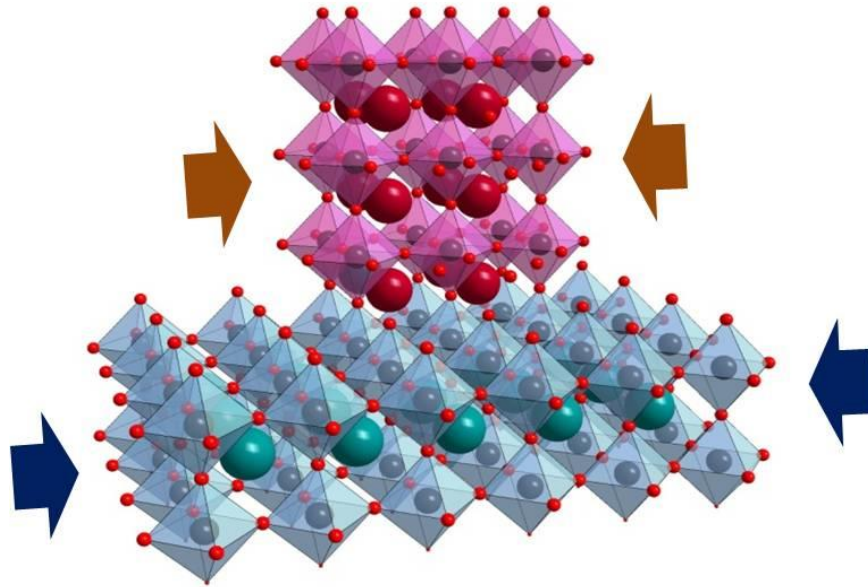


Figure 4.11 Schematic of the compressive STO:Ni thin film biaxially strained to match the substrate PMN-PT.

To explain the mechanism of the observed controllable luminescence, the lattice deformation of STO:Ni (600 nm)/PMN-PT under dc bias voltage should be considered. Figure 4.10 presents the XRD patterns of STO:Ni (600 nm)/PMN-PT under dc bias voltage ranging from 0 to 500 V. Obviously, the (002) diffraction peak of PMN-PT shows a shift to lower angles when increasing the applied voltage. According to the Bragg's law and Poisson ratio of PMN-PT, the out-of-plane and in-plane strains can be calculated. It is evident that the PMN-PT substrate produces out-of-plane tensile strain, resulting in in-plane compressive strain. Compared with the zero-biased condition, the application of 500 V along the [001] direction induces an out-of-plane tensile strain about 0.106 %, while the in-plane compressive strain is



about 0.07 %. Meanwhile, with increasing the voltage, the (002) diffraction peak of STO also shows a slight shift to lower angles. It implies that the c lattice constant of STO:Ni (600 nm) film under 500 V is increased up to about 0.016 %, while the in-plane lattice constants decrease about 0.012 % when the applied voltage is increased from 0 V to 500 V. Obviously, the changes in STO:Ni film lattice are smaller than those of PMN-PT. Such difference originates from the different elastic responses and interface PMN-PT and STO. Hence, as shown in Figure 4.11, it is confirmed that the in-plane compressive strain produced by the PMN-PT substrate has been transferred to the STO:Ni (600 nm) thin film. The strain makes the $[\text{NiO}]_6$ octahedron to become compressive. The change in crystal field around Ni^{2+} ion leads to the observed modulation of NIR emission as shown in Figure 4. The results are agreed with our earlier study on the chemical substitution-induced tuning of luminescence, in which enhanced crystal field around Ni^{2+} ion can induce intense PL intensity, blue-shift in emission peak, and long effective lifetime [Bai, 2014]. Since the Ni^{2+} - O^{2-} bond distance decreases as the applied bias voltage increasing, the crystal field around Ni^{2+} ion will get enhanced and lattice relaxation will become weaker. Then larger splitting energy benefits to an increase in the transition energy from the excited state levels to the ground state level, resulting in the luminescent peak blue-shifted. On the other hand, the reduced non-radiative transition enhances the emission intensity and modifying the effective lifetime.

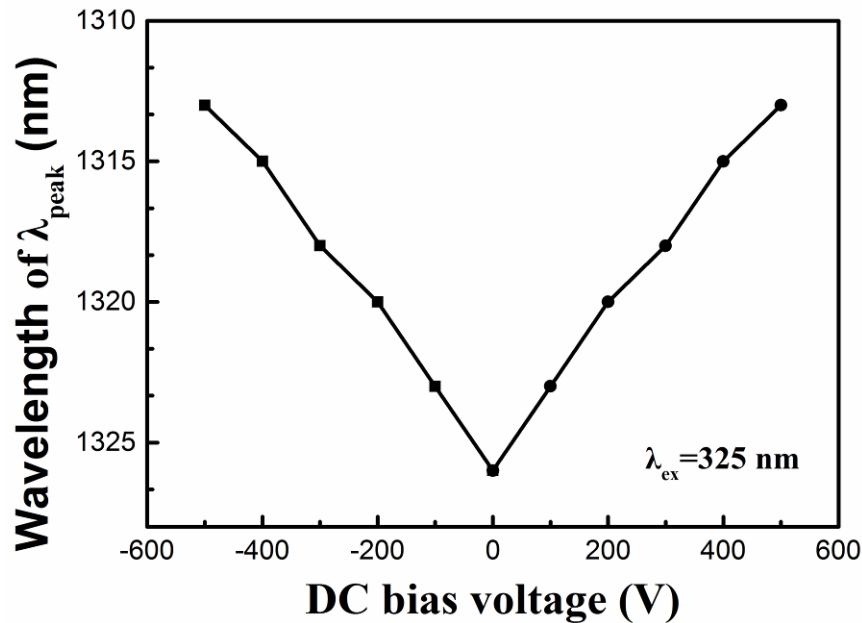


Figure 4.12 The PL emission peak position of STO:Ni (600 nm)/PMN-PT as a function of the applied voltage from -500 V to 500 V.

In our experiment, the NIR PL peak of STO:Ni (600 nm) thin film shows blue-shifted characteristics under positive DC bias voltages. The NIR PL peak of STO:Ni (600 nm) thin film also presents blue-shifted characteristics under negative DC bias voltages, indicating a similar strain is produced by the PMN-PT substrate. Notably, the PL emission peak position of STO:Ni (600 nm)/PMN-PT shows a fine V-shaped curve as a function of the applied bias voltage as shown in Figure 4.12, which is similar to the our recent report [Jie, 2013]. The PL results of STO:Ni (600 nm)/PMN-PT demonstrate that controllable NIR emission can be tuned in *in situ* and real-time way by applying external electric field controlled strain.



4.5 Conclusions of strain induced tunable PL in STO:Ni

thin film

In summary, strain induced tunable NIR luminescence of STO:Ni thin film grown on piezoelectric PMN-PT substrate has been demonstrated using two approaches of strain engineering. Film thickness dependent misfit strain can greatly affect the luminescent properties, including emission peak position, FWHM, and effective lifetime, due to the variation in crystal field and lattice relaxation around Ni^{2+} ion. Moreover, the emission characteristics of STO:Ni thin film grown on PMN-PT can be tuned under the control of an external electric field in reversible and real-time manner. The reported tuning of NIR luminescence by coupling of photonic and piezoelectric characteristics in the work is contrast to conventional chemical ways, i.e. changes in formula and/or synthesis condition of phosphors. The results may provide a promise to develop novel planar NIR light sources based on strain-controllable luminescent STO:Ni thin films.



Chapter 5 Broadband NIR Luminescence from Bi and Bi/Ho co-doped Thin Films

In Chapter 3 and 4, Ni-doped photonic materials with ultrabroadband NIR emission have been studied. In this chapter, Bi and Bi/Ho co-doped thin films prepared by PLD will be studied.

5.1 Introduction

Currently, Bi-doped photonic materials have attracted much attention due to their ultrabroadband NIR luminescence covering the entire optical fiber communication windows [Khonthon, 2009; Ruan, 2009; Peng, 2011; Sun, 2012]. To date, numerous kinds of Bi-doped fiber lasers operating in 1140-1550 nm have been developed showing prospective applications in optical fiber communication, medical and astrophysics [Dianov, 2012; Shubin, 2012]. In addition, light sources in the wavelength region of $\sim 2 \mu\text{m}$ have many desirable properties, such as low absorption by the atmosphere and strong absorption by human tissue. Moreover, several atmospheric components, such as H_2O , CO_2 and NO_2 , show strong absorption around $2 \mu\text{m}$ [Cornacchia, 2009; Godard, 2009; Jha, 2012]. Thus, Ho^{3+} -doped lasers at $\sim 2 \mu\text{m}$ have potential applications in medical, materials processing, remote atmosphere sensing, optical communication, coherent light detection and ranging, molecular spectroscopy, military, optical parametric oscillator operating in the mid-



infrared region [Godard, 2009; Richards, 2007]. At present, various types of lasers at $\sim 2 \mu\text{m}$ have been developed by using Ho^{3+} -doped glass fibers, single-crystals and bulk glass waveguides [Fusari, 2010; Wang, 2013]. Planar waveguide lasers are capable of combining the advantages of both solid-state bulk lasers and fiber lasers, such as high optical gain, guided spatial-mode control, considerable immunity to both external environment conditions and thermal effects, conveniently to be integrated with other devices on chips [Mackenzie, 2007; Zhang, 2013]. However, due to the lack of high quality and efficient NIR luminescent films, development and application of planar waveguide lasers have been met with limited success. Thus, it is expected that development of Bi and/or Ho-doped planar waveguide lasers may open broad prospects of applications.

Due to the lack of commercial available laser diode for the direct excitation of Ho^{3+} , traditionally, Er^{3+} , Tm^{3+} , Yb^{3+} , Nb^{3+} have been used as sensitizers to enhance the $\sim 2 \mu\text{m}$ luminescence of Ho^{3+} . However, the energy transfer efficiency has proven to be low [Bai, 2011; He, 2012]. As Ho^{3+} shows the absorption at around 1160 and 1950 nm, arising from the transition of $^5\text{I}_8$ to $^5\text{I}_6$ and $^5\text{I}_7$ energy levels, respectively. Thus, if a sensitizer has broad and efficient luminescence in these regions and no absorption in $\sim 2 \mu\text{m}$, high energy transfer efficiency may be realized. Germanate glasses have low phonon energy, high refractive index and high transparency in 0.38-5 μm [Jha, 2012]. The partial substitution of fluoride for oxide in glasses can further reduce the optical basicity and enhance the near-infrared luminescence of Bi



[Bai, 2013]. In this work, we have performed pulsed laser deposition (PLD) to prepare Bi-doped oxyfluoride germanate thin films with broadband near-infrared luminescence. Importantly, by the sensitization of Bi near-infrared active centers (BNAC), the luminescence of Ho^{3+} around 2 μm is significantly enhanced, presenting promising applications in planar waveguide lasers. The mechanisms behind the observed phenomena are discussed.

5.2 Preparation and measurements of Bi doped thin films

Glass targets with a nominal composition (in mol%) of $5\text{Na}_2\text{O}-20\text{MgF}_2-20\text{Al}_2\text{O}_3-55\text{GeO}_2-x\text{BiF}_3-y\text{HoF}_3$ ($x = 2, y = 0, 1; x = 0, y = 1$) were prepared by melt-quenching approach. Analytical grade reagents Na_2CO_3 , MgF_2 , Al_2O_3 , GeO_2 , BiF_3 , HoF_3 were used as raw materials. The batches were melted in platinum crucibles at 1430 °C for 30 min and then casted onto a stainless steel plate. The obtained glasses were annealed at 400 °C for 10 h and then cooled to room temperature at a rate of 0.5 °C/min. The glasses were cut into the size of 30×30×4 mm and then polished. PLD technique with KrF excimer laser ($\lambda = 248$ nm) was used to prepare the films. The distance between the glass targets and the substrates was kept at 5 cm. All the films were deposited on silica substrate at 450 °C without post-annealing. The oxygen partial pressure (P_{O_2}) during deposition was kept to be 1.0, 3.5 and 6.0 Pa, respectively.

XRD (Rigaku D/max 2550PC, 3 kW) was used to measure the 2θ scanning



patterns of the films at a step of 0.02° . Scanning electron microscopy (SEM) (HITACHI S-4800) was used to study the morphology of the films. FLS920 fluorescence spectrophotometer (Edinburgh Instrument Ltd.) with 450 W Xe lamp and 200 mW 808 nm laser diodes was used to measure the emission (PL) and excitation (PLE) spectra, and the fluorescence decay curves. The pulse laser at 808 nm with a repetition rate of 90 Hz was generated with the assistance of a signal generator. The spectral resolution was 1 nm. X-ray photoelectron spectroscopy (XPS) measurements were performed on Physical Electronics 5600 multi-technique system. Achromatic 150 W Al $K\alpha$ X-ray was used as the excitation source. The pressure inside the analyzer chamber was kept at about 10^{-9} Torr. C1s peak was shifted to 285.0 eV for the binding energy calibration. The resolution was 0.05 eV. Raman spectra were characterized by Horiba Jobin Yvon HR800 Raman spectrometer. The excitation source was a 488 nm laser and the diameter of laser spot size was 1 μm . Absorption spectra were taken on UV3600 UV-Vis-NIR spectrophotometer (Shimadzu Corp.). The change of grating slit was at 835 nm. The resolution was 1 nm.

5.3 Results and discussion of Bi-doped thin films

5.3.1 Bi and Bi/Ho codoped germanate glass thin films

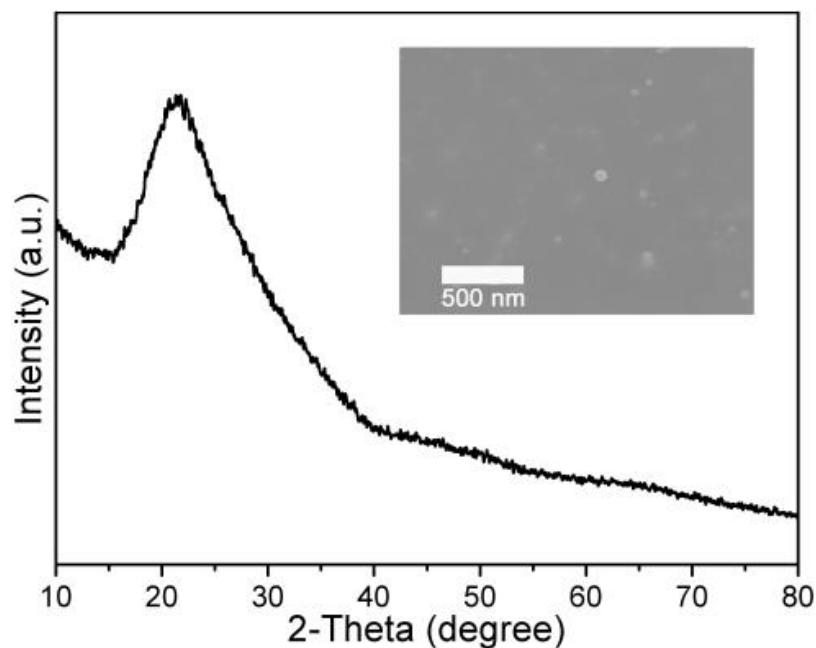


Figure 5.1 XRD pattern of Bi-doped germanate film deposited under 1.0 Pa. The inset is SEM plan view of the film.

Figure 5.1 displays XRD pattern of Bi-doped germanate film deposited under 1.0 Pa. Only a broad diffraction peak at ~ 21 degree is observed, implying the amorphous state of the film. Films deposited under other P_{O_2} show similar crystalline result. The inset presents SEM image of the film. The film is dense and smooth with continuous structure. Only a few particles were seen on the surface of the film.

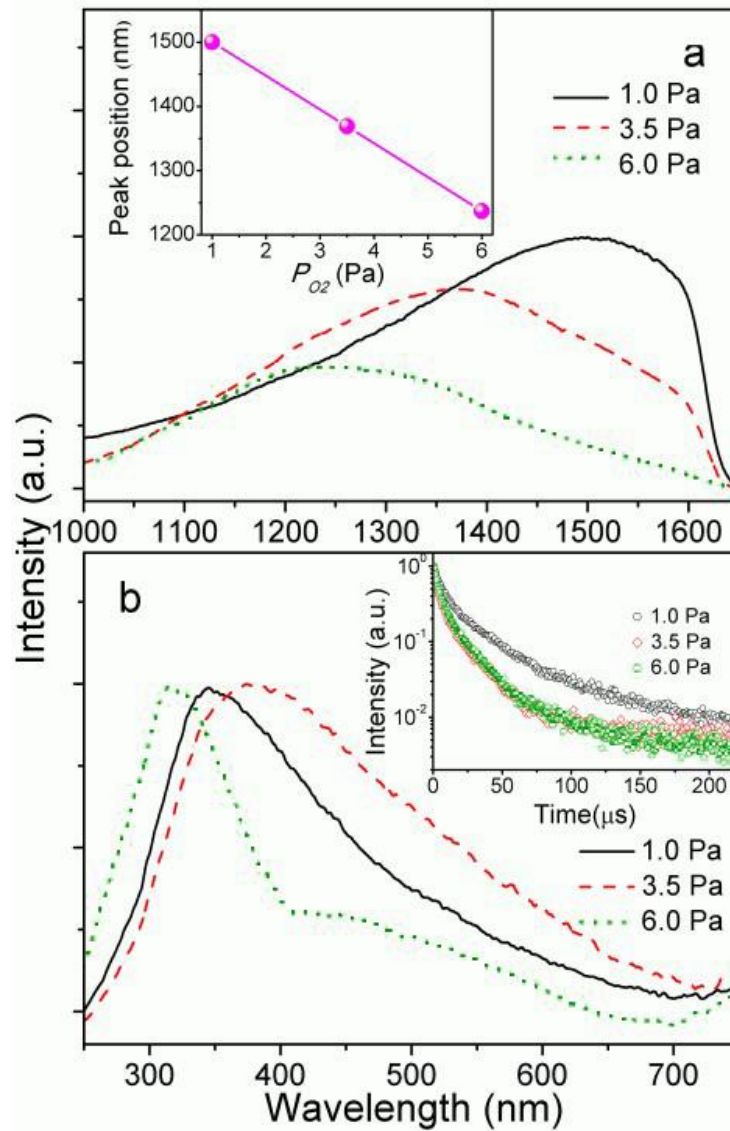


Figure 5.2 PL and PLE spectra of Bi-doped germanate films deposited under different P_{O_2} measured by InGaAs detector. (a) The inset is the P_{O_2} dependent emission peak position change. (b) The monitored emission wavelength is at 1500, 1370 and 1240 nm, respectively. The inset is the fluorescence decay curves of the Bi-

doped germanate films.

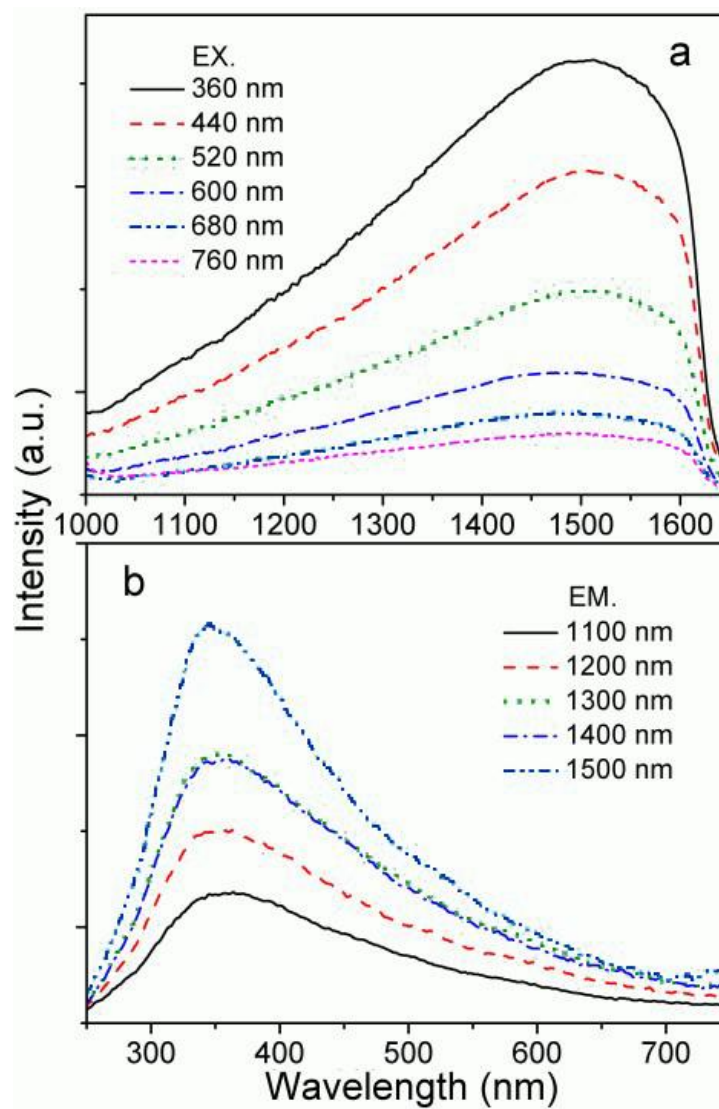


Figure 5.3 (a) PL and (b) PLE spectra of Bi-doped germanate film deposited under 1.0 Pa.



The luminescence properties of Bi-doped germanate films were investigated. Figure 5.2 displays PL spectra of Bi-doped films deposited under different oxygen pressure. All the films present broad emission bands covering 1000-1650 nm. The emission intensity dropping at the wavelength above 1600 nm is due to the low spectral response of InGaAs detector around 1600 nm. The emission peak position shows a red-shift from 1240 to 1500 nm, and the emission intensity rises when decreasing oxygen pressure from 6.0 to 1.0 Pa. Such a trend in P_{O_2} dependent emission peak position has only been observed in Bi-doped films prepared by PLD. For those films prepared by other methods, the emission peak position remains unchanged as P_{O_2} changes [Fujii, 2013; Wu, 2001; Xu, 2012]. As previously reported, the decrease of oxygen pressure during PLD growth results in the reduction of Bi species [Fujii, 2013]. Therefore, the emission at long wavelength is ascribed to Bi species of lower valence state [Fujii, 2013]. Till now, much work has focused on the investigation of low valent state Bi species or Bi cluster ions as the BNAC [Khonthon, 2009; Li, 2013; Ruan, 2009; Peng, 2011; Sun, 2012; Xu, 2011; Xu, 2013; Zhou, 2008; Zhou, 2009]. There is the possibility that as P_{O_2} decreases, the amount of BNAC will increase, leading to higher emission intensity. In Figure 5.2 (b), all the films show a main excitation band in the UV range with a shoulder in the blue-green region. The inset is the fluorescence decay curves of the films. The monitored emission wavelength is at 1500, 1370 and 1240 nm, respectively. All the curves show second-order exponential decay with the mean lifetime of 17.5, 7.3 and 8.9 μ s for the films deposited under 1.0, 3.5 and 6.0 Pa, respectively. The lifetimes here are

much shorter than those reported data obtained from BNAC (Bi^+ , Bi^0 , etc) [Romanov, 2013; Xu, 2013; Zhou, 2008]. Our measured results are close to the lifetime values from Bi clusters (Bi_5^{3+} , etc) [Xu, 2011; Zhou, 2009].

Figure 5.3 displays PL and PLE spectra of Bi-doped germanate film deposited under 1.0 Pa. All the emission peak positions remain at 1500 nm under different excitation wavelength. The excitation peak position remains unchanged as well. The films deposited under other P_{O_2} show similar behaviors. Thus, it is speculated that one kind of BNAC or several kinds of BNAC with similar luminescence properties in the film prepared under certain P_{O_2} [Fujii, 2013].

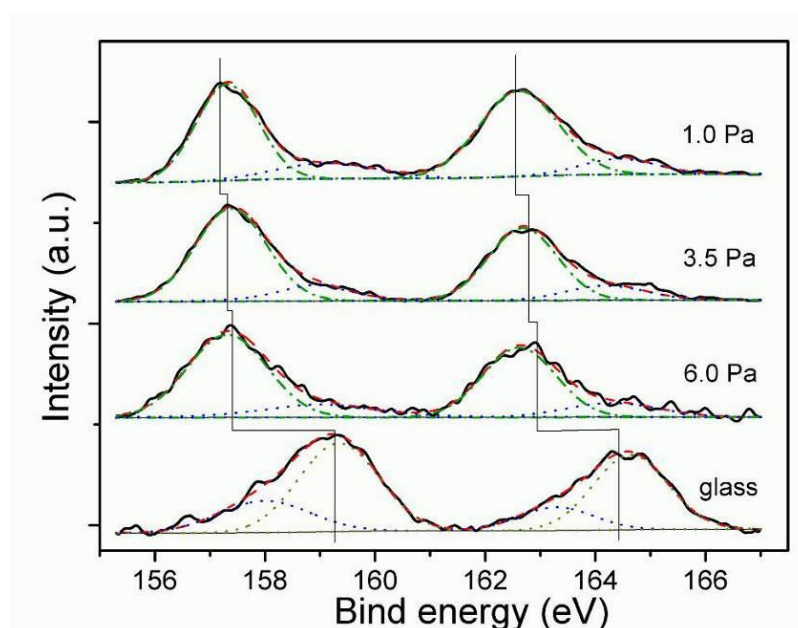


Figure 5.4 XPS spectra of Bi-doped glass and films deposited under different P_{O_2} . Solid lines represent measured curves, the dashed lines fit the Lorentzian-Gaussian

curves.

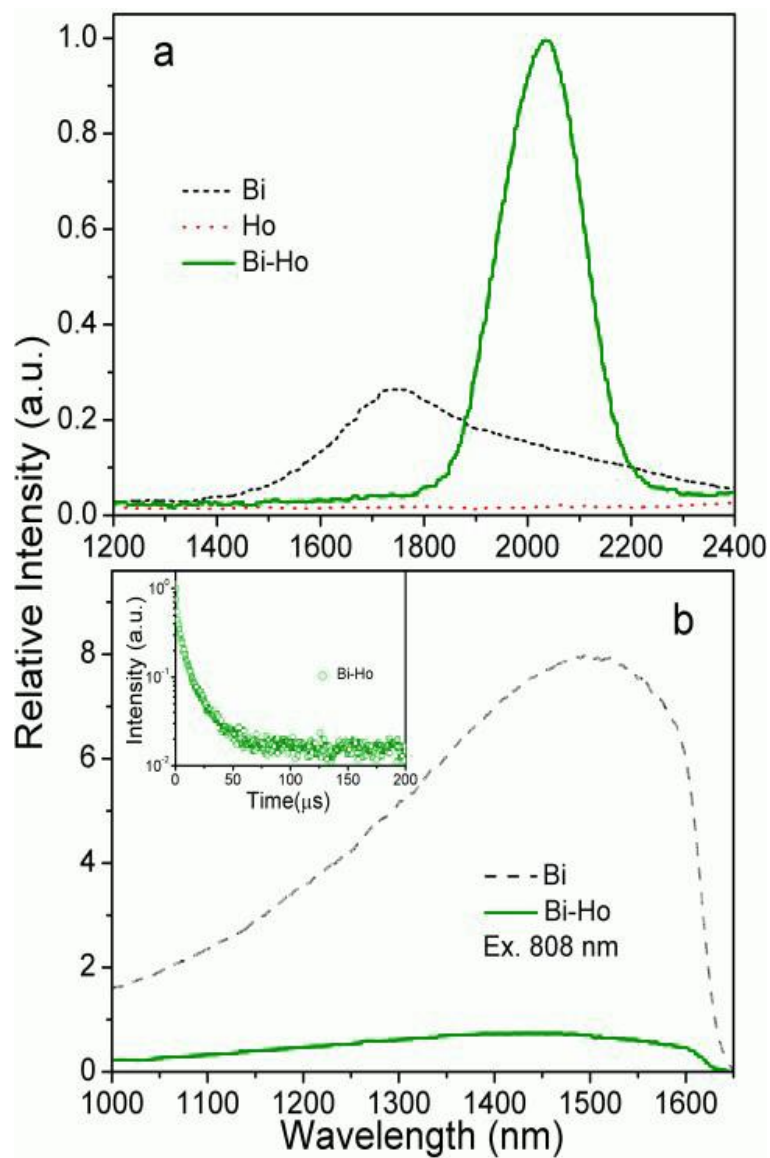


Figure 5.5 PL spectra of germanate films deposited under 1.0 Pa. The luminescence in (a) and (b) is measured by InSb and InGaAs detectors, respectively. The inset in (b) is the fluorescence decay curve of Bi/Ho co-doped germanate film monitored at 1500



nm.

To further reveal the mechanism of NIR luminescence in Bi-doped films, XPS spectra of Bi-doped glass target and films deposited under P_{O_2} of 1.0, 3.5 and 6.0 Pa are measured as shown in Figure 5.4. Each spectrum composes two bands. The binding energy of the glass is much higher than those of films. With the increase of the deposited P_{O_2} , the bands of films continue shifting to higher binding energy. The binding energy of $4f_{7/2}$ core level of Bi species is 5.3 eV lower than that of $4f_{5/2}$ core level in our experiment, which agrees with the reported value [Sun, 2011; Sun, 2012; Xu, 2010]. As either of the two bands can represent the characteristics of Bi species, the origin of the observed band corresponding to $4f_{7/2}$ core level can be interpreted as follows. The dotted lines in Figure 5.4 can be fitted as the Lorentzian-Gaussian curves. In the fitted curves, the glass has a dominant band at 159.3 eV and a weak band at 158.0 eV. The dominant band is due to Bi^{3+} [Hamm, 1998; Plotnichenko, 2013; Xu, 2010]. Typically, Bi^0 atoms have binding energy between 156.9 and 157.1 eV [Xu, 2010]. The weak band at 158.0 eV locates between the binding energy of Bi^{3+} and Bi^0 . It is ascribed to Bi species of low valence states [Hamm, 1998], which is consistent with the report that Bi species of low valence states contribute to the NIR luminescence in glasses [Takahashi, 2003; Xu, 2013]. The main Bi species in the glass is Bi^{3+} . The weak bands for the films deposited under 1.0, 3.5 and 6.0 Pa are at high energy of 159.1, 158.9, 159.0 eV corresponding to Bi^{3+} , respectively [Hamm, 1998; Plotnichenko, 2013; Xu, 2010]. The dominant bands for films



deposited under 1.0, 3.5 and 6.0 Pa are at 157.2, 157.3, 157.3 eV, respectively. They are 0.2-0.3 eV higher than the binding energy of typical Bi^0 atoms. However, we cannot rule out the possibility of Bi^0 atoms responsible for the origin of these bands. When some atomic oxygen is directly attached to Bi^0 adatoms on the surface, the binding energy of Bi^0 atoms can be as high as 157.6 eV [Xu, 2013]. Besides, Bi clusters, such as dimer, trimer, Bi_5^{3+} and so on, may exist as they could also contribute to the shift of the binding energy to higher value. As discussed in Figure 5.2, the emission at long wavelength is ascribed to Bi species of lower valence states. And individual Bi^0 atoms cannot cause the shift of the emission peak position as the P_{O_2} changes. Consequently, the NIR emission spectra and fluorescence lifetimes of the films are most likely to be related to different kinds of Bi clusters (Bi_5^{3+} , Bi_8^{2+}) [Lin, 2011; Xu, 2011], by combing previous reports [Fujii, 2013; Xu, 2011] and our results here. The ratio of the amount of Bi^0 atoms or Bi clusters to that of Bi^{3+} can be calculated according to the integrated area of the bands. With the increase of P_{O_2} , this ratio decreases from 4.7 to 4.5, and then to 3.8, implying the decrease of the amount of Bi^0 atoms or Bi clusters in films. These results are consistent with the explanation of Figure 5.2 (a), where the emission intensity decreases with the increase of P_{O_2} .

As Bi-doped germanate film deposited under 1.0 Pa shows the most intense luminescence, the films deposited under 1.0 Pa are chosen to investigate the luminescence properties in the following part. PL spectra of Bi, Ho singly doped and



Bi/Ho co-doped germanate films are presented in Figure 5.5 (a). Bi-doped germanate film shows broad emission peaked at around 1750 nm. The sharp drop in the wavelength shorter than 1400 nm is due to the low spectra response of InSb detector at specific wavelength region. Combined with Figure 5.2, the results imply that Bi-doped films show super broadband luminescence in 1000-2400 nm. No luminescence is observed in Ho-doped film. Bi/Ho co-doped film shows broad luminescence in the range of 1800-2300 nm with an intense emission peak at around 2030 nm corresponding to the transition from the excited state 5I_7 to the ground state 5I_8 of Ho^{3+} . In addition, the peak at around 1750 nm corresponding to BNAC was not observed. Figure 5.5 (b) shows NIR PL spectra of Bi-doped and Bi/Ho co-doped films. In contrast to Bi-doped film, BNAC in Bi/Ho co-doped film shows much weaker luminescence. The inset is the fluorescence decay curve of Bi/Ho co-doped film monitored at around 1500 nm. The curve shows second-order exponential decay with the mean lifetime of 4.8 μs . The lifetime is much shorter than that of Bi-doped film as the discussion for the inset of Figure 5.2 (b). These results confirm the energy transfer from BNAC to Ho^{3+} in films. The energy transfer efficiency η can be calculated according to the following equation:

$$\eta = 1 - \frac{\tau_{\text{Bi/Ho}}}{\tau_{\text{Bi}}} \quad (5.1)$$

where $\tau_{\text{Bi/Ho}}$, τ_{Bi} are the lifetimes of the emission at 1500 nm of Bi/Ho co-doped and Bi-doped germanate films, respectively. The energy transfer efficiency is calculated

to be 72.6%. Thus, BNAC are efficient to sensitize the $\sim 2 \mu\text{m}$ luminescence of Ho^{3+} in films.

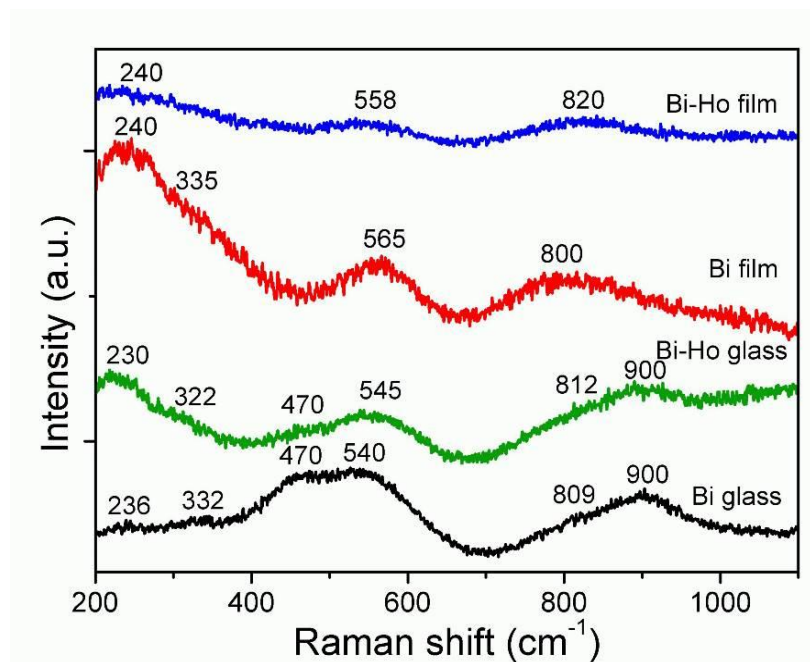


Figure 5.6 Raman spectra of Bi-doped, Bi/Ho co-doped germanate glasses and films.

The structures of Bi-doped and Bi/Ho co-doped germanate films are compared with those of glasses by Raman spectra in Figure 5.6. For the Bi-doped germanate glass, bands at 236 and 332 cm^{-1} are related to bending modes of Q^2 and Q^1 tetrahedra [Sheng, 2013]. Band at 470 cm^{-1} is ascribed to three-membered rings of GeO_4 associated symmetric stretching vibration of Ge-O-Ge bonds [Sun, 2012]. Symmetric bending mode of Ge-O-Ge bonds in GeO_4 corresponds to the band at 540 cm^{-1} [Kamitsos, 1996]. Bands at 809 and 900 cm^{-1} are attributed to the transverse optical and longitudinal optical split asymmetric stretching modes of Ge-O-Ge bonds

[Sun, 2012]. The bands of Bi/Ho co-doped glass are similar to that of Bi-doped glass except a slight shift. Compared with those of glasses, all the bands of films below 700 cm^{-1} have a shift to larger wavenumber, implying the increase of the distortion of GeO_4 . The main difference is the diminish of the bands at 470 and 900 cm^{-1} for both films and the disappearance of the band at 322 cm^{-1} in Bi/Ho co-doped film. All the above changes may indicate that the network in films is more disordered and inhomogeneous than that in glasses [Fujii, 2013]. According to the above discussion about the luminescence properties of films, the slight difference in the bands between Bi-doped and Bi-Ho co-doped films has little influence on the luminescence properties of films.

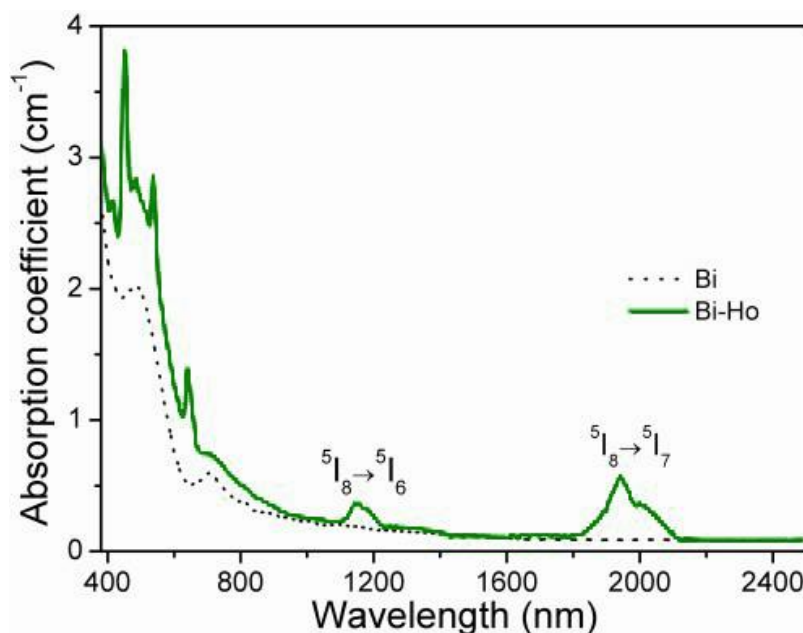


Figure 5.7 Absorption spectra of Bi-doped and Bi/Ho co-doped germanate glasses.

To further reveal the mechanism of the energy transfer from BNAC to Ho^{3+} , absorption spectra are measured. Due to the strong interference of light across films, the absorption spectra of Bi-doped and Bi/Ho co-doped glass are present to study the energy transfer process in Figure 5.7. The inset is the partially enlarged figure. Bi/Ho co-doped glass shows absorption bands at around 1160 and 1950 nm, attributing to the transition from the ground state $^5\text{I}_8$ to the excited states $^5\text{I}_6$ and $^5\text{I}_7$ of Ho^{3+} , respectively. The two absorption bands locate at the emission range of Bi-doped film.

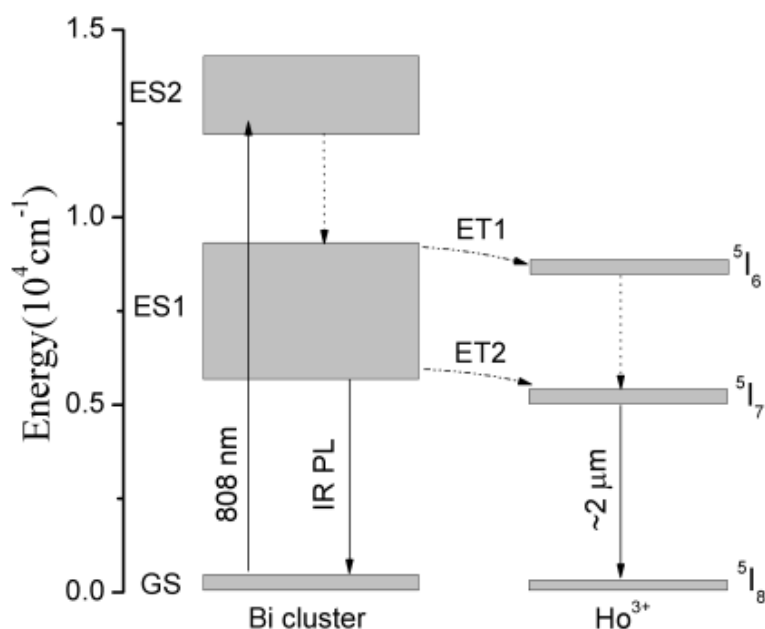


Figure 5.8 Energy level scheme and energy transfer process between Bi cluster and Ho^{3+} .

Thus, the possible mechanism of the enhanced ~2 μm luminescence in Bi/Ho co-doped film is illustrated as shown in Figure 5.8, in which the energy level model



associated with Bi clusters and Ho^{3+} is proposed. The energy can be transferred from the excited states of BNAC to the excited states $^5\text{I}_6$ and $^5\text{I}_7$ of Ho^{3+} through ET1 and ET2 processes. As the phonon energy of the films is $800\text{-}900\text{ cm}^{-1}$ as shown in Figure 5.6, three phonons are needed to bridge the gaps between the excited states $^5\text{I}_6$ and $^5\text{I}_7$ of Ho^{3+} . Then, multi-phonon-assisted relaxation occurs from $^5\text{I}_6$ to $^5\text{I}_7$ level. Subsequently, intense $\sim 2\text{ }\mu\text{m}$ luminescence from the transition $^5\text{I}_7$ to $^5\text{I}_8$ occurs. Here, the energy transfer efficiency is much larger than that found in Bi/Ho co-doped borophosphate glass [Henderson, 1991]. For Bi/Ho co-doped borophosphate glass, there is only energy transfer to the excited state $^5\text{I}_6$ of Ho^{3+} . In contrast, due to the energy transfer to both the excited states $^5\text{I}_6$ and $^5\text{I}_7$ of Ho^{3+} , BNAC can efficiently sensitize the luminescence of Ho^{3+} in films. Moreover, the lower phonon energy of Bi/Ho co-doped oxyfluoride germanate film compared to that of Bi/Ho co-doped borophosphate glass could also lead to the high energy transfer efficiency.

5.3.2 Bi doped phosphate glass thin films

Phosphate glasses are very attractive photonic hosts, and they process a fine solubility for metal ions. The Bi doped phosphate glass with chemical composition $83\text{P}_2\text{O}_5\text{-}17\text{Al}_2\text{O}_3\text{-}1\text{B}_2\text{O}_3$ has been prepared. Considering the Bi-doped germanate film deposited under 1.0 Pa O_2 owning the most intense luminescence and the longest lifetime, Bi doped phosphate thin film is deposited on silicon wafer under 1.0 Pa O_2 , and the luminescence properties would be investigated in the following part.

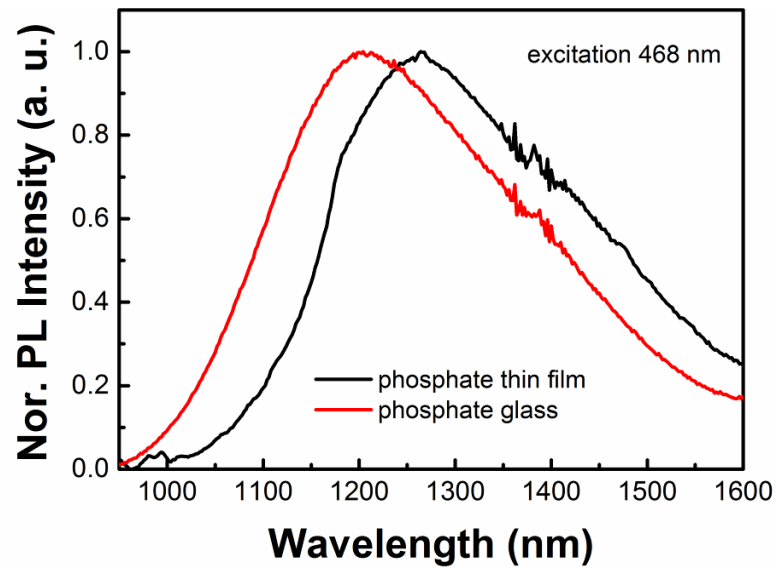


Figure 5.9 PL spectra of Bi-doped phosphate film deposited under 1.0 Pa and the glass target.

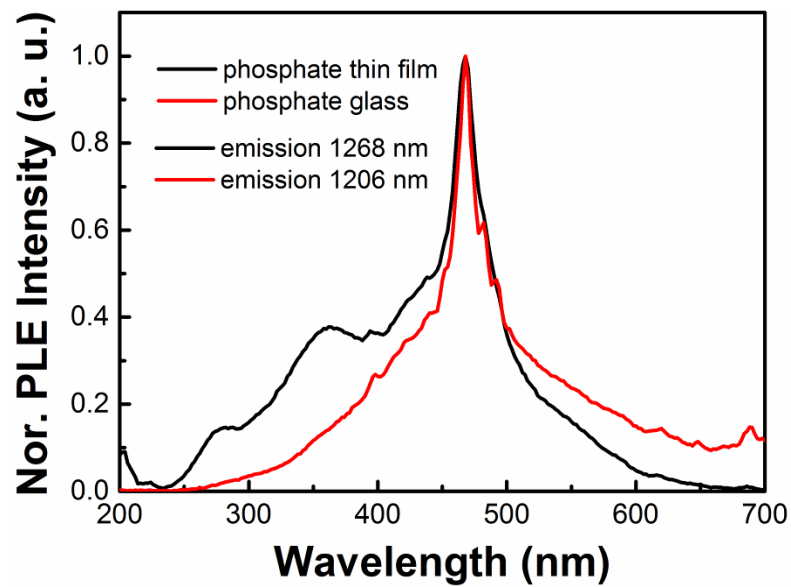


Figure 5.10 PLE spectra of Bi-doped phosphate film deposited under 1.0 Pa and the

glass target.

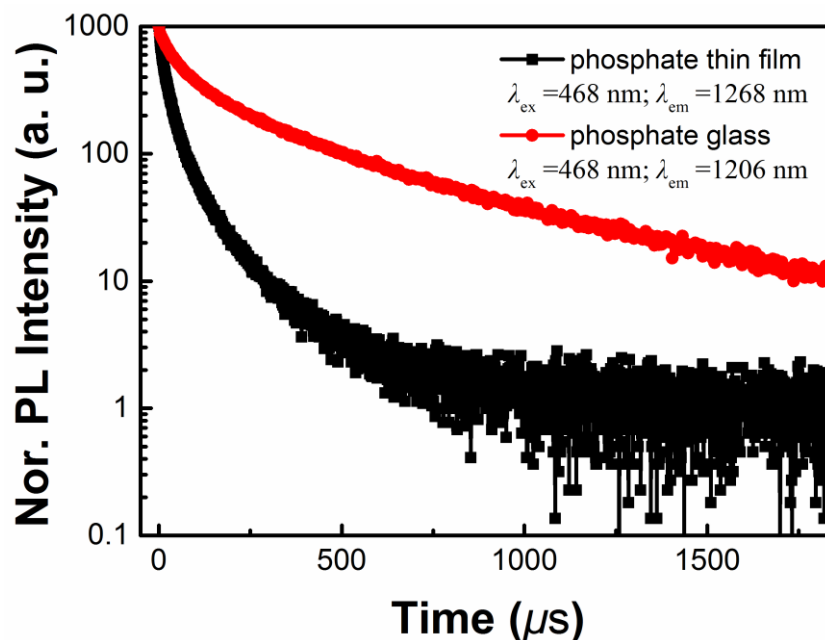


Figure 5.11 The fluorescence decay curves of Bi-doped phosphate film and the glass target.

The luminescence properties of Bi-doped phosphate film and the glass target were investigated. Figure 5.9 shows PL spectra of Bi-doped phosphate glass and film deposited under deposited under 1.0 Pa O_2 . Both the Bi-doped phosphate glass and film present broad emission bands covering 1000-1600 nm, with the typical widths over 250 nm. Compared with the glass target, the emission peak position of the prepared film shows a red-shift from 1206 to 1268 nm. As discussed above, the low oxygen pressure during PLD growth results in the reduction of Bi species, leading to



the emission shift. In Figure 10, both the glass target and film show a main excitation band in the blue-green region with a shoulder in the UV range. Figure 11 shows the fluorescence decay curves of the target and the grown film. The monitored emission wavelength is at the emission peaks, and the excitation wavelength is 468 nm. All the curves show second-order exponential decay with the mean lifetime of 22, 104 μs for the Bi-doped phosphate film and the glass target, respectively. The lifetime of the phosphate target is similar to BNAC (Bi^+ , Bi^0 , etc) in germanate and silicate glasses [Romanov, 2013; Xu, 2013; Zhou, 2008]. The lifetime of Bi-doped phosphate film is close to the lifetime values from that of Bi-doped germanate film deposited under 1.0 Pa O_2 (17.5 μs). Hence, the NIR emission center in the target should be BNAC (Bi^+ , Bi^0 , etc), from the $\text{Bi}^{0,2}\text{D}_{3/2} \rightarrow {}^4\text{S}_{3/2}$ and $\text{Bi}^{+,3}\text{P}_1 \rightarrow {}^3\text{P}_0$ transitions. The NIR luminescence of Bi-doped phosphate film may result from Bi clusters (dimer, trimer, Bi_5^{3+}).

5.4 Conclusion of Bi doped thin films

In conclusion, Bi, Ho singly doped and Bi/Ho co-doped oxyfluoride germanate films have been prepared by PLD. Bi singly doped film shows luminescence in 1000~2400 nm. With the decrease of oxygen pressure during deposition process, the emission peak shows a red-shift. The infrared luminescence may result from Bi clusters. For Bi/Ho co-doped film, large enhancement in broad infrared luminescence of Ho^{3+} at ~2 μm has been observed, due to the energy transfer from the excited states of Bi active centers to the excited states ${}^5\text{I}_6$ and ${}^5\text{I}_7$ of Ho^{3+} . The



energy transfer efficiency is as high as 72.6%. In addition, Bi-doped phosphate film with broadband NIR emission has been developed. These results not only provide a new insight into the mechanism of the NIR luminescence in Bi-doped materials, but also are potentially helpful for the future development of NIR luminescent planar waveguide laser.



Chapter 6 Conclusions and Suggestions for Future Work

6.1 Conclusions of the thesis

In this thesis, two kinds of non-rare-earth doped photonic materials are studied for realizing ultrabroadband NIR luminescence. PL of these photonic materials have been characterized, and the influence of strain, chemical composition, and growth condition of the thin-film photonic materials on their NIR emission have been also investigated. The main conclusions can be briefly described as follows:

Tunable and ultrabroadband NIR luminescence from Ni²⁺-doped ferroelectric perovskites is demonstrated. Ultrabroadband NIR luminescence of the prepared materials covers optical communication band from 1100 nm to over 1600 nm, with the largest bandwidth of 295 nm. With the increase in Ba concentration of Ni²⁺-doped BST, the crystal field becomes weaker, and the peak position of NIR emission is greatly changed from 1273 nm to 1542 nm, while the effective lifetime τ decreases from 303.5 μ s to 51.31 μ s. Exceptional peak shift magnitude up to 269 nm is much larger than that of other previously reported Ni²⁺-doped materials. The results in our study imply that the potential of Ni²⁺-doped ferroelectric perovskites as a new class of multifunctional materials for optical amplifiers, biomedicine, and tunable light sources.



Ultrabroadband NIR luminescence from Ni²⁺-doped BST is demonstrated. With the increase of temperature, the luminescence properties are affected by phase transition induced crystal field change and temperature dependent nonradiative relaxation. Ni²⁺ ions can be a promising probe for the crystal structure at low temperature (below 230 K). The broadband NIR PL covers optical communication band from 1200 nm to > 1600 nm, with a bandwidth greater than 200 nm. The excited state lifetime of ⁶Ni²⁺:³T₂(³F) was found to be 327 μs at 100 K and 160 μs at 300 K. In addition, ultrabroadband NIR luminescence was also observed in Ni²⁺-doped BST thin film at ambient temperature. The presented results make Ni²⁺-doped BST promising for widespread applications in broadband optical amplifier and optoelectronic integrated devices.

Tunable and ultrabroadband NIR luminescence from Ni²⁺-doped ferroelectric perovskites oxides thin films is demonstrated. Ultrabroadband NIR luminescence of the prepared materials covers optical communication band from 1100 nm to over 1600 nm, with FWHM exceeding 200 nm. With the increase in Ba concentration of Ni²⁺-doped BST-*x* thin films, the crystal field becomes weaker, and the peak position of NIR emission is greatly changed from 1287 nm to 1569 nm, while the effective lifetime τ decreases from 910 μs to 30 μs. In addition, fixed the composition of STO:Ni thin film, tunable NIR luminescence is demonstrated through change the deposited wafer. The luminescence properties are affected by the misfit substrate induced crystal field change. The presented results make Ni²⁺-doped BST-*x*



promising for widespread applications in broadband optical amplifier and optoelectronic integrated devices.

Strain induced tunable NIR luminescence of STO:Ni thin film grown on piezoelectric PMN-PT substrate is demonstrated using two approaches of strain engineering. Film thickness dependent misfit strain can greatly affect the luminescent properties, including emission peak position, FWHM, and effective lifetime, due to the variation in crystal field and lattice relaxation around Ni²⁺ ion. Moreover, the emission characteristics of STO:Ni thin film grown on PMN-PT can be tuned under the control of an external electric field in reversible and real-time manner. The reported tuning of NIR luminescence by coupling of photonic and piezoelectric characteristics in the work is contrast to conventional chemical ways, i.e. changes in formula and/or synthesis condition of phosphors. The results may provide a promise to develop novel planar NIR light sources based on strain-controllable luminescent STO:Ni thin films.

Bi, Ho singly doped and Bi/Ho co-doped oxyfluoride germanate films have been prepared by PLD. Bi singly doped germanate film shows luminescence in 1000~2400 nm. With the decrease of oxygen pressure during deposition process, the emission peak shows a red-shift. The infrared luminescence may result from Bi clusters. For Bi/Ho co-doped film, large enhancement in broad infrared luminescence of Ho³⁺ at ~2 um has been observed, due to the energy transfer from the excited states of Bi active centers to the excited states ⁵I₆ and ⁵I₇ of Ho³⁺. The



energy transfer efficiency is as high as 72.6%. The results not only provide a new insight into the mechanism of the near-infrared luminescence in Bi-doped materials, but also are potentially helpful for the future development of near-infrared luminescent planar waveguide laser.



6.2 Suggestions for future work

As discussed in this thesis, non-rare-earth doped photonic materials with ultrabroadband NIR luminescence have been widely studied since they are promising for practical applications in of tunable lasers and broadband optical amplifiers. Non-rare-earth doped thin-film photonic materials with ultrabroadband NIR luminescence (FWHM >200 nm), covering the whole optical telecommunication, have been developed in this thesis. Tunable and ultrabroadband NIR luminescence from Ni²⁺-doped perovskites oxides is demonstrated through control of chemical composition and strain engineering. Tunable and ultrabroadband NIR luminescence from Bi-doped glass thin film is demonstrated through control of growth conditions. This will lead to a better understanding of how to obtain photonic materials with improved and desired optical properties. However, there is plenty room needing further research. It is necessary to further consider the following prospects of the present work.

Tunable and ultrabroadband NIR luminescence from Ni²⁺-doped ferroelectric oxides is developed. Exceptional emitting-wavelength has been achieved through control of chemical composition. Simultaneous tunable photoluminescence and ferroelectric properties are realized in BST-*x*:Ni. Considering the ferroelectric and structure of BTO:Ni, the luminescence of Ni ions should be affected by the external electric field. In the future, electric field induced tunable luminescence of BTO:Ni thin films can be developed, for integrating PL and ferroelectric properties. Since electric field induced tunable luminescence is an *in-situ* and real-time manner, also a



form of optoelectronic integration.

Integration of active optoelectronics on a wafer is relevant to on-chip interconnection and line-of-sight free-space communications, both for reliable friend identification and data communications [Sargent, 2005]. Electroluminescent devices in the NIR associate telecommunications and signal-processing systems with the carriers used in optical communications. Therefore, based on the developed thin-film photonic materials with broadband NIR luminescence, thin-film electroluminescent devices with broadband NIR emission should be considered, for integrated optoelectronics. For gaining NIR electroluminescence, both high-field and injection electroluminescent devices based on the developed thin-film photonic materials can be considered.

Under a single wavelength excitation, both Ni- and Bi-doped thin films present ultrabroadband NIR emission in the wavelength range from 1100 to >1600 nm, with the bandwidth larger than 200 nm. The ferroelectric Ni-doped thin films may present unique waveguide by coupling the electric field. The amorphous Bi-doped glass thin films can be readily adjusted their optical properties (e.g., refractive) by tuning their composite and the growth conditions. To further demonstrate the promising practical applications of these novel photonic thin-films, optical amplification experiments should be taken with a pump laser. Since the parameters of amplification bandwidth, optical gain and loss are important for a planar optical amplifier.



Recently, flexible electronic, photonic, and optoelectronics devices have drawn considerable attention, motivated by their numerous economically relevant applications (e.g., wearable intelligent electronics, lightning, and rollable displays). Using the chemical etching and laser lift-off, the solid substrates can be peeled off. After peel off the substrate, the as-prepared no-RE doped thin films can be transferred to the flexible plastic substrates. And then the prepared photonic thin films can present flexible properties and be utilized as flexible waveguide or other optoelectronics devices. The thesis has suggested that the NIR PL of STO:Ni thin film can be effectively modulated by strain. Considering fabricating flexible and stretchable STO:Ni thin film, its NIR emission may be readily modulated by applying strain.

Tunable NIR emission is achieved in Ni-doped photonic materials, due to the change in crystal field around Ni ions. Whereas tunable NIR luminescence from Bi-doped photonic materials can be achieved by control the Bi species. Unfortunately, in many cases there has no evident and convincing explanation for the relationship between microenvironment and the emitter. Therefore, a clear trend is the research gradually turned to the relationship between the host and emitter [Sun, 2014]. Succeeded in realizing this, one must pay more attention to structural analyses using some advanced characterization techniques. This will lead to a better understanding of how to get materials with desired optical properties or how to lower the luminescence quenching. Although in recent years, ab initio methods and density



functional theory approaches have been used to calculate the electronic structure of Bi units [Huang, 2009; Walsh, 2006], there are still large differences between theoretical and experimental results. Therefore, more detailed work on this direction can help build compelling structure-emitter property relationships, resulting in clearer picture PL mechanisms, including Ni ions and Bi species.



References

Andreici, L., Brik, M. G., and Avram, N. M., Electron-Phonon Coupling in Ni²⁺-Doped MgGa₂O₄ Spinel. *Romanian Reports in Physics*, 63, 1048-1052, 2011.

Arai, Y., Suzuki, T., Ohishi, Y., Morimoto, S., and Khonthon, S., Ultrabroadband near-infrared emission from a colorless bismuth-doped glass. *Applied Physics Letters*, 90, 261110, 2007.

Bagad, V. S., Optical fiber communications. 2009: Technical Publications.

Bai, G., Guo, Y., Tian, Y., Hu, L., and Zhang, J., Light emission at 2 μm from Ho-Tm-Yb doped silicate glasses. *Optical Materials*, 33, 1316-1319, 2011.

Bai, G., Tao, L., Li, K., Hu, L., and Tsang, Y. H., Enhanced ~2 μm and upconversion emission from Ho-Yb codoped oxyfluoride glass ceramics. *Journal of Non-crystalline Solids*, 361, 13-16, 2013.

Bai, G. X., Tao, L. L., Wang, Y. G., and Tsang, Y. H., Upconversion Luminescence of Tm³⁺/Yb³⁺ Codoped Oxyfluoride Glass Ceramics Containing Ba₂YbF₇ Nanocrystals. *Integrated Ferroelectrics*, 142, 31-36, 2013.

Bai, G., Tsang, M. K., and Hao, J., Tuning the Luminescence of Phosphors: Beyond Conventional Chemical Method. *Advanced Optical Materials*, 3, 431, 2015.



Bai, G. X., Zhang, Y., and Hao, J. H., Chemical substitution-induced exceptional emitting-wavelength tuning in transition metal Ni²⁺-doped ferroelectric oxides with ultrabroadband near-infrared luminescence. *Journal of Materials Chemistry C*, 2, 4631-4635, 2014.

Bai, Z., Fujii, M., Mori, Y., Miwa, Y., Mizuhata, M., Sun, H. T., and Hayashi, S., Efficient near-infrared emission from neodymium by broadband sensitization of bismuth in zeolites. *Optics Letters*, 36, 1017-9, 2011.

Bao, H. X., Zhou, S. F., Feng, G. F., Wang, X., Qiao, X. S., and Qiu, J. R., Luminescence properties of nickel and bismuth co-doped barium aluminosilicate glasses. *Journal of Alloys and Compounds*, 456, 239-242, 2008.

Belancon, M. P., Marconi, J. D., Ando, M. F., and Barbosa, L. C., Near-IR emission in Pr³⁺ single doped and tunable near-IR emission in Pr³⁺/Yb³⁺ codoped tellurite tungstate glasses for broadband optical amplifiers. *Optical Materials*, 36, 1020-1026, 2014.

Bilani-Zeneli, O., Rata, A. D., Herklotz, A., Mieth, O., Eng, L. M., Schultz, L., Biegalski, M. D., Christen, H. M., and Dorr, K., SrTiO₃ on piezoelectric PMN-PT(001) for application of variable strain. *Journal of Applied Physics*, 104, 054108, 2008.

Blasse, G. and Grabmaier, B., Luminescent materials. Vol. 44. 1994: Springer.



Brik, M. G., Avram, N. M., and Avram, C. N., Comparative crystal field study of Ni^{2+} energy levels in NiCl_2 , NiBr_2 , and NiI_2 crystals. *Physica B-Condensed Matter*, 371, 43-49, 2006.

Brik, M. G., Avram, N. M., Avram, C. N., Rudowicz, C., Yeung, Y. Y., and Gnutek, P., Ground and excited state absorption of Ni^{2+} ions in MgAl_2O_4 : Crystal field analysis. *Journal of Alloys and Compounds*, 432, 61-68, 2007.

Brik, M. G., Avram, C. N., and Avram, N. M., Comparative study of crystal field effects for Ni^{2+} ion in LiGa_5O_8 , MgF_2 and AgCl crystals. *Journal of Physics and Chemistry of Solids*, 69, 1796-1801, 2008.

Brik, M. G., Crystal field analysis of the absorption spectra and electron-phonon interaction in $\text{Ca}_3\text{Sc}_2\text{Ge}_3\text{O}_{12}:\text{Ni}^{2+}$. *Journal of Physics and Chemistry of Solids*, 67, 738-744, 2006.

Brik, M. G., Kumar, G. A., and Sardar, D. K., Ab initio, crystal field and experimental spectroscopic studies of pure and Ni^{2+} -doped KZnF_3 crystals. *Materials Chemistry and Physics*, 136, 90-102, 2012.

Bünzli, J.-C. G. and Eliseeva, S. V., Lanthanide NIR luminescence for telecommunications, bioanalyses and solar energy conversion. *Journal of Rare Earths*, 28, 824-842, 2010.

Cao, L. Z., Cheng, B. L., Wang, S. Y., Fu, W. Y., Ding, S., Sun, Z. H., Yuan, H. T.,



Zhou, Y. L., Chen, Z. H., and Yang, G. Z., Influence of stress on Raman spectra in $\text{Ba}_{1-x}\text{Sr}_x\text{TiO}_3$ thin films. *Journal of Physics D: Applied Physics*, 39, 2819-2823, 2006.

Chang, W. T., Gilmore, C. M., Kim, W. J., Pond, J. M., Kirchoefer, S. W., Qadri, S. B., Chirsey, D. B., and Horwitz, J. S., Influence of strain on microwave dielectric properties of $(\text{Ba,Sr})\text{TiO}_3$ thin films. *Journal of Applied Physics*, 87, 3044-3049, 2000.

Chen, D. Q., Wang, Y. S., and Hong, M. C., Lanthanide nanomaterials with photon management characteristics for photovoltaic application. *Nano Energy*, 1, 73-90, 2012.

Chen, L. and Wei, X. H., Upconversion Luminescence Tuning of Er^{3+} -Doped Barium Titanate. *Integrated Ferroelectrics*, 140, 187-194, 2012.

Chi, Y. and Chou, P.-T., Transition-metal phosphors with cyclometalating ligands: fundamentals and applications. *Chemical Society Reviews*, 39, 638-655, 2010.

Choi, K. J., Biegalski, M., Li, Y. L., Sharan, A., Schubert, J., Uecker, R., Reiche, P., Chen, Y. B., Pan, X. Q., Gopalan, V., Chen, L. Q., Schlom, D. G., and Eom, C. B., Enhancement of ferroelectricity in strained BaTiO_3 thin films. *Science*, 306, 1005-9, 2004.

Claudionico, https://en.wikipedia.org/wiki/Electron_microscope, 2013.



Dai, N. L., Wang, Y. S., Xu, B., Yang, L. Y., Luan, H. X., and Li, J. Y., Effect of yttrium oxide addition on absorption and emission properties of bismuth-doped silicate glasses. *Journal of Rare Earths*, 30, 418-421, 2012.

Dai, N., Xu, B., Jiang, Z., Peng, J., Li, H., Luan, H., Yang, L., and Li, J., Effect of Yb³⁺ concentration on the broadband emission intensity and peak wavelength shift in Yb/Bi ions co-doped silica-based glasses. *Optics Express*, 18, 18642-8, 2010.

Dianov, E. M., Amplification in Extended Transmission Bands Using Bismuth-Doped Optical Fibers. *Journal of Lightwave Technology*, 31, 681-688, 2013.

Dianov, E. M., Bismuth-doped optical fibers: a challenging active medium for near-IR lasers and optical amplifiers. *Light: Science & Applications*, 1, e12, 2012.

Dianov, E. M., Shubin, A. V., Melkumov, M. A., Medvedkov, O. I., and Bufetov, I. A., High-power cw bismuth-fiber lasers. *JOSA B*, 24, 1749-1755, 2007.

Dong, G. P., Wu, B. T., Zhang, F. T., Zhang, L. L., Peng, M. Y., Chen, D. D., Wu, E., and Qiu, J. R., Broadband near-infrared luminescence and tunable optical amplification around 1.55 μm and 1.33 μm of PbS quantum dots in glasses. *Journal of Alloys and Compounds*, 509, 9335-9339, 2011.

Dugue, A., Cormier, L., Dargaud, O., Galois, L., and Calas, G., Evolution of the Ni²⁺ Environment during the Formation of a MgO-Al₂O₃-SiO₂ Glass-Ceramic: A Combined XRD and Diffuse Reflectance Spectroscopy Approach. *Journal of The*



American Ceramic Society, 95, 3483-3489, 2012.

Dvoyrin, V., Mashinsky, V., and Dianov, E., Efficient bismuth-doped fiber lasers. *IEEE Journal of Quantum Electron*, 44, 834-840, 2008.

Eliseeva, S. V. and Buenzli, J.-C. G., Lanthanide luminescence for functional materials and bio-sciences. *Chemical Society Reviews*, 39, 189-227, 2010.

Fan, X., Su, L. B., Ren, G. H., Jiang, X. T., Xing, H. B., Xu, J., Tang, H. L., Li, H. J., Zheng, L. H., Qian, X. B., and Feng, H., Influence of thermal treatment on the near-infrared broadband luminescence of Bi:CsI crystals. *Optical Materials Express*, 3, 400-406, 2013.

Feng, W., Han, C. M., and Li, F. Y., Upconversion-Nanophosphor-Based Functional Nanocomposites. *Advanced Materials*, 25, 5287-5303, 2013.

Firstov, S., Khopin, V., Bufetov, I., Firstova, E., Guryanov, A., and Dianov, E., Combined excitation-emission spectroscopy of bismuth active centers in optical fibers. *Optics Express*, 19, 19551-19561, 2011.

Firstov, S. V., Shubin, A. V., Khopin, V. F., Mel'kumov, M. A., Bufetov, I. A., Medvedkov, O. I., Gur'yanov, A. N., and Dianov, E. M., Bismuth-doped germanosilicate fibre laser with 20 W output power at 1460 nm. *Quantum Electronics*, 41, 581-583, 2011.



Fujimoto, Y., *Bi-doped glasses for broadband fiber light source*, in *Optical Components and Materials VI*, Jiang, S., Digonnet, M. J. F., Glesener, J. W., and Dries, J. C., Editors. 2009.

Gao, G., Peng, M., and Wondraczek, L., Temperature dependence and quantum efficiency of ultrabroad NIR photoluminescence from Ni²⁺ centers in nanocrystalline Ba-Al titanate glass ceramics. *Optics Letters*, 37, 1166-8, 2012.

Gao, G. J., Reibstein, S., Spiecker, E., Peng, M. Y., and Wondraczek, L., Broadband NIR photoluminescence from Ni²⁺-doped nanocrystalline Ba-Al titanate glass ceramics. *Journal of Materials Chemistry*, 22, 2582-2588, 2012.

Giles, C. R. and Desurvire, E., Modeling erbium-doped fiber amplifiers. *Journal of Lightwave Technology*, 9, 271-283, 1991.

Guo, X., Li, H. J., Su, L. B., Yu, P. S., Zhao, H. Y., Liu, J. F., and Xu, J., Near-infrared broadband luminescence in Bi₂O₃-GeO₂ binary glass system. *Laser Physics*, 21, 901-905, 2011.

Hagimoto, K., Iwatsuki, K., Takada, A., Nakazawa, M., Saruwatari, M., Aida, K., Nakawaga, K., and Horiguchi, M. A 212 km non-repeated transmission experiment at using LD pumped Er³⁺-doped fiber amplifiers in an in/direct-detection repeater system. *Optical Fiber Communication Conference*. 1989. Optical Society of America.



Hao, J., Gao, J., and Cocivera, M., Tuning of the blue emission from europium-doped alkaline earth chloroborate thin films activated in air. *Applied Physics Letters*, 82, 2778-2780, 2003.

Hao, J. H., Gao, J., and Wong, H. K., Laser molecular beam epitaxy growth and properties of SrTiO₃ thin films for microelectronic applications. *Thin Solid Films*, 515, 559-562, 2006.

Hao, J. H., Luo, Z., and Gao, J., Effects of substrate on the dielectric and tunable properties of epitaxial SrTiO₃ thin films. *Journal of Applied Physics*, 100, 2006.

Hao, J., Zhang, Y., and Wei, X., Electric-Induced Enhancement and Modulation of Upconversion Photoluminescence in Epitaxial BaTiO₃: Yb/Er Thin Films. *Angewandte Chemie*, 123, 7008-7012, 2011.

Haruna, T., Kakui, M., Taru, T., Ishikawa, S., and Onishi, M. *Silica-Based Bismuth-Doped Fiber for Ultra Broad Band Light Source and Optical Amplification around at 1.1 μm*. in *Optical Amplifiers and Their Applications*. 2005. Optical Society of America.

Harvey, J., <http://libraryschool.libguidescms.com/achem>. 2015

Hau, T. M., Wang, R. F., Zhou, D. C., Yu, X., Song, Z. G., Yang, Z. W., Yang, Y., He, X. J., and Qiu, J. B., Infrared broadband emission of bismuth-thulium co-doped



lanthanum-aluminum-silica glasses. *Journal of Luminescence*, 132, 1353-1356, 2012.

Hau, T. M., Wang, R. F., Yu, X., Zhou, D. C., Song, Z. G., Yang, Z. W., He, X. J., and Qiu, J. B., Near-infrared broadband luminescence and energy transfer in Bi-Tm-Er co-doped lanthanum aluminosilicate glasses. *Journal of Physics and Chemistry of Solids*, 73, 1182-1186, 2012.

Hazarika, A., Layek, A., De, S., Nag, A., Debnath, S., Mahadevan, P., Chowdhury, A., and Sarma, D. D., Ultranarrow and Widely Tunable Mn^{2+} -Induced Photoluminescence from Single Mn-Doped Nanocrystals of ZnS-CdS Alloys. *Physical Review Letters*, 110, 2013.

Huang, W. L. and Zhu, Q., DFT calculations on the electronic structures of BiOX (X= F, Cl, Br, I) photocatalysts with and without semicore Bi 5d states. *Journal of Computational Chemistry*, 30, 183-190, 2009.

Jiang, A., Scott, J., Lu, H., and Chen, Z., Phase transitions and polarizations in epitaxial $BaTiO_3/SrTiO_3$ superlattices studied by second-harmonic generation. *Journal of Applied Physics*, 93, 1180-1185, 2003.

Kamimura, M., Kanayama, N., Tokuzen, K., Soga, K., and Nagasaki, Y., Near-infrared (1550 nm) in vivo bioimaging based on rare-earth doped ceramic nanophosphors modified with PEG-b-poly (4-vinylbenzylphosphonate). *Nanoscale*, 3, 3705-3713, 2011.



Keiser, G., *Optical fiber communications*. 2003: Wiley Online Library.

Kuleshov, N. V., Shcherbitsky, V. G., Mikhailov, V. P., Kuck, S., Koetke, J., Petermann, K., and Huber, G., Spectroscopy and excited-state absorption of Ni²⁺-doped MgAl₂O₄. *Journal of Luminescence*, 71, 265-268, 1997.

Kück, S., Laser-related spectroscopy of ion-doped crystals for tunable solid-state lasers. *Applied Physics B*, 72, 515-562, 2001.

Kramer, B., *Advances in Solid State Physics*, Springer, Berlin, 2003.

Krsmanovic, R. M., Antic, Z., Mitric, M., Dramicanin, M. D., and Brik, M. G., Structural, spectroscopic and crystal field analyses of Ni²⁺ and Co²⁺ doped Zn₂SiO₄ powders. *Applied Physics A-materials Science & Processing*, 104, 483-492, 2011.

Lee, C. T., Zhang, M. S., Yin, Z., and Zhu, W., Structural and vibrational properties of Ba_xSr_{1-x}TiO₃ nanoparticles. *Journal of Materials Science*, 40, 1277-1279, 2005.

Lemanov, V., Smirnova, E., Syrnikov, P., and Tarakanov, E., Phase transitions and glasslike behavior in Sr_{1-x}Ba_xTiO₃. *Physical Review B*, 54, 3151, 1996.

Li, K., Fan, H., Zhang, G., Bai, G., Fan, S., Zhang, J., and Hu, L., Broadband near-infrared emission in Er³⁺-Tm³⁺ co-doped bismuthate glasses. *Journal of Alloys and Compounds*, 509, 3070-3073, 2011.

Liu, Y. S., Tu, D. T., Zhu, H. M., and Chen, X. Y., Lanthanide-doped luminescent



nanoprobes: controlled synthesis, optical spectroscopy, and bioapplications. *Chemical Society Reviews*, 42, 6924-6958, 2013.

Mech, A., Monguzzi, A., Meinardi, F., Mezyk, J., Macchi, G., and Tubino, R., Sensitized NIR erbium (III) emission in confined geometries: a new strategy for light emitters in telecom applications. *Journal of The American Chemical Society*, 132, 4574-4576, 2010.

Melkumov, M., Bufetov, I., Shubin, A., Firstov, S., Khopin, V., Guryanov, A., and Dianov, E., Laser diode pumped bismuth-doped optical fiber amplifier for 1430 nm band. *Optics Letters*, 36, 2408-2410, 2011.

Miwa, Y., Sun, H. T., Imakita, K., Fujii, M., Teng, Y., Qiu, J., Sakka, Y., and Hayashi, S., Sensitized broadband near-infrared luminescence from bismuth-doped silicon-rich silica films. *Optics Letters*, 36, 4221-3, 2011.

Mironova-Ulmane, N., Brik, M. G., and Sildos, I., Crystal field calculations of energy levels of the Ni²⁺ ions in MgO. *Journal of Luminescence*, 135, 74-78, 2013.

Morimoto, S., Fujii, M., Sun, H. T., Miwa, Y., Imakita, K., Qiu, J. R., and Hayashi, S., Broadband near-infrared emission from bismuth-doped multilayer films. *Journal of Applied Physics*, 112, 073511, 2012.

Mott, N. F. and Gurney, R. W., *Electronic processes in ionic crystals*, Dover, New



York, 1964.

Murata, K., Fujimoto, Y., Kanabe, T., Fujita, H., and Nakatsuka, M., Bi-doped SiO₂ as a new laser material for an intense laser. *Fusion Engineering and Design*, 44, 437-439, 1999.

Nakazawa, M., Kimura, Y., and Suzuki, K., Efficient Er³⁺-doped optical fiber amplifier pumped by a 1.48 μm InGaAsP laser diode. *Applied Physics Letters*, 54, 295-297, 1989.

Peng, M. Y., Dong, G. P., Wondraczek, L., Zhang, L. L., Zhang, N., and Qiu, J. R., Discussion on the origin of NIR emission from Bi-doped materials. *Journal of Non-crystalline Solids*, 357, 2241-2245, 2011.

Peng, M. Y., Meng, X. G., Qiu, J. R., Zhao, Q. Z., and Zhu, C. S., GeO₂: Bi, M (M = Ga, B) glasses with super-wide infrared luminescence. *Chemical Physics Letters*, 403, 410-414, 2005.

Peng, M. Y., Qiu, J. R., Chen, D. P., Meng, X. G., Yang, I. Y., Jiang, X. W., and Zhu, C. S., Bismuth- and aluminum-codoped germanium oxide glasses for super-broadband optical amplification. *Optics Letters*, 29, 1998-2000, 2004.

Peng, M. Y., Zhao, Q. Z., Qiu, J. R., and Wondraczek, L., Generation of Emission Centers for Broadband NIR Luminescence in Bismuthate Glass by Femtosecond



Laser Irradiation. *Journal of The American Ceramic Society*, 92, 542-544, 2009.

Qiu, J. R., Peng, M. Y., Ren, J. J., Meng, X. G., Jiang, X. W., and Zhu, C. S., Novel Bi-doped glasses for broadband optical amplification. *Journal of Non-crystalline Solids*, 354, 1235-1239, 2008.

Qiu, J. R., Zhou, S. F., Ren, J. J., Wu, B. T., and Aoe, *Novel glasses and glass-ceramics for broadband optical amplification*. Aoe 2007: Asia Optical Fiber Communication & Optoelectronic Exposition & Conference, Conference Proceedings. 2008. 617-619.

Raman, C. V., and Krishnan, K. S., A New Type of Secondary Radiation. *Nature*, 121, 501, 1928.

Romanov, A. N., Haula, E. V., Fattakhova, Z. T., Veber, A. A., Tsvetkov, V. B., Zhigunov, D. M., Korchak, V. N., and Sulimov, V. B., Near-IR luminescence from subvalent bismuth species in fluoride glass. *Optical Materials*, 34, 155-158, 2011.

Romanov, A. N., Veber, A. A., Fattakhova, Z. T., Usovich, O. V., Haula, E. V., Trusov, L. A., Kazin, P. E., Korchak, V. N., Tsvetkov, V. B., and Sulimov, V. B., Subvalent bismuth monocation Bi^+ photoluminescence in ternary halide crystals KAlCl_4 and KMgCl_3 . *Journal of Luminescence*, 134, 180-183, 2013.

Ruan, J., Chi, Y. Z., Liu, X. F., Dong, G. P., Lin, G., Chen, D. P., Wu, E., and Qiu, J. R., Enhanced near-infrared emission and broadband optical amplification in Yb-Bi



- co-doped germanosilicate glasses. *Journal of Physics D-applied Physics*, 42, 2009.
- Ruan, J., Su, L., Qiu, J., Chen, D., and Xu, J., Bi-doped BaF₂ crystal for broadband near-infrared light source. *Optics Express*, 17, 5163-9, 2009.
- Ruan, J., Wu, E., Wu, B. T., Zeng, H. P., Zhang, Q., Dong, G. P., Qiao, Y. B., Chen, D. P., and Qiu, J. R., Spectral properties and broadband optical amplification of Yb-Bi codoped MgO-Al₂O₃-ZnO-SiO₂ glasses. *Journal of the Optical Society of America B-optical Physics*, 26, 778-782, 2009.
- Ruan, J., Wu, B. T., Chen, D. P., Qiao, Y. B., and Qiu, J. R., Energy transfer and enhanced broadband near-infrared luminescence in Yb-Bi codoped phosphate glasses. *Journal of Materials Research*, 24, 516-519, 2009.
- Samson, B., Pinckney, L., Wang, J., Beall, G., and Borrelli, N., Nickel-doped nanocrystalline glass-ceramic fiber. *Optics Letters*, 27, 1309-1311, 2002.
- Sargent, E. H., Infrared quantum dots. *Advanced Materials*, 17, 515-522, 2005.
- Schlaghecken, G., Gottmann, J., Kreutz, E. W., and Poprawe, R., Pulsed laser deposition of Er : BaTiO₃ for planar waveguides. *Applied Physics A-materials Science & Processing*, 79, 1255-1257, 2004.
- Schlom, D. G., Chen, L. Q., Eom, C. B., Rabe, K. M., Streiffer, S. K., and Triscone, J. M., *Strain tuning of ferroelectric thin films*, in *Annual Review of Materials*



Research, 2007, p. 589-626.

Schubert, E. F. and Kim, J. K., Solid-state light sources getting smart. *Science*, 308, 1274-1278, 2005.

Sheng, Q. C., Wang, X. L., and Chen, D. P., Enhanced Luminescent Properties and Mechanism in a Novel Yb-Bi Co-doped Boro-phosphate Glass. *Materials Letters*, 80, 135-137, 2012.

Sheng, Q. C., Zhou, Q. L., and Chen, D. P., Efficient methods of obtaining good optical properties in Yb-Bi co-doped phosphate glasses. *Journal of Materials Chemistry C*, 1, 3067-3071, 2013.

Shirasaki, Y., Supran, G. J., Bawendi, M. G., and Bulović, V., Emergence of colloidal quantum-dot light-emitting technologies. *Nature Photonics*, 7, 13-23, 2013.

Sigaev, V. N., Golubev, N. V., Ignat'eva, E. S., Savinkov, V. I., Campione, M., Lorenzi, R., Meinardi, F., and Paleari, A., Nickel-assisted growth and selective doping of spinel-like gallium oxide nanocrystals in germano-silicate glasses for infrared broadband light emission. *Nanotechnology*, 23, 015708, 2012.

Skoromets, V., Kadlec, C., Kuzel, P., Kamba, S., and Schubert, J., Electric field tuning of hard polar phonons in strained SrTiO₃ films. *Journal of Applied Physics*, 107, 2010.



Smith, A. M., Mancini, M. C., and Nie, S., Bioimaging: second window for in vivo imaging. *Nature Nanotechnology*, 4, 710-711, 2009.

Sokolov, V. O., Plotnichenko, V. G., and Dianov, E. M., Origin of broadband near-infrared luminescence in bismuth-doped glasses. *Optics Letters*, 33, 1488-1490, 2008.

Sokolov, V. O., Plotnichenko, V. G., and Dianov, E. M., Interstitial BiO molecule as a broadband IR luminescence centre in bismuth-doped silica glass. *Quantum Electronics*, 41, 1080-1082, 2011.

Sokolov, V. O., Plotnichenko, V. G., Koltashev, V. V., and Dianov, E. M., Centres of broadband near-IR luminescence in bismuth-doped glasses. *Journal of Physics D-applied Physics*, 42, 2009.

Song, Z. G., Li, C., Li, Y. J., Yang, Z. W., Zhou, D. C., Yin, Z. Y., Wang, X., Wang, Q., Hau, T. M., Zhao, Z. Y., Yang, Y., Yu, X., and Qiu, J. B., The influence of alkali ions size on the superbroadband NIR emission from bismuth-doped alkali aluminoborophosphosilicate glasses. *Optical Materials*, 35, 61-64, 2012.

Song, Z. G., Yang, Z. W., Zhou, D. C., Yin, Z. Y., Li, C., Wang, R. F., Shang, J. H., Lou, K., Xu, Y. Y., Yu, X., and Qiu, J. B., The effect of P₂O₅ on the ultrabroadband near-infrared luminescence from bismuth-doped SiO₂-Al₂O₃-CaO glass. *Journal of Luminescence*, 131, 2593-2596, 2011.



Sorokin, E., Naumov, S., and Sorokina, I. T., Ultrabroadband infrared solid-state lasers. *IEEE Journal of Selected Topics In Quantum Electronics*, 11, 690-712, 2005.

Steckel, J. S., Coe-Sullivan, S., Bulovic, V., and Bawendi, M. G., 1.3 μm to 1.55 μm tunable electroluminescence from PbSe quantum dots embedded within an organic device. *Advanced Materials*, 15, 1862-1866, 2003.

Su, L., Zhou, P., Yu, J., Li, H., Zheng, L., Wu, F., Yang, Y., Yang, Q., and Xu, J., Spectroscopic properties and near-infrared broadband luminescence of Bi-doped SrB_4O_7 glasses and crystalline materials. *Optics Express*, 17, 13554-60, 2009.

Sun, H. T., Xu, B. B., Yonezawa, T., Sakka, Y., Shirahata, N., Fujii, M., Qiu, J. R., and Gao, H., Photoluminescence from $\text{Bi}_5(\text{GaCl}_4)_3$ molecular crystal. *Dalton Transactions*, 41, 11055-11061, 2012.

Sun, H. T., Sakka, Y., Shirahata, N., Gao, H., and Yonezawa, T., Experimental and theoretical studies of photoluminescence from Bi_8^{2+} and Bi_5^{3+} stabilized by AlCl_4^- in molecular crystals. *Journal of Materials Chemistry*, 22, 12837-12841, 2012.

Sun, H.-T., Shimaoka, F., Miwa, Y., Ruan, J., Fujii, M., Qiu, J., and Hayashi, S., Sensitized superbroadband near-IR emission in bismuth glass/Si nanocrystal superlattices. *Optics Letters*, 35, 2215-2217, 2010.

Sun, H.-T., Zhou, J., and Qiu, J., Recent advances in bismuth activated photonic



materials. *Progress In Materials Science*, 64, 1-72, 2014.

Suzuki, T., Hughes, M., and Ohishi, Y., Optical properties of Ni-doped MgGa_2O_4 single crystals grown by floating zone method. *Journal of Luminescence*, 130, 121-126, 2010.

Takeda, K., Muraishi, T., Hoshina, T., Takeda, H., and Tsurumi, T., Dielectric tunability and electro-optic effect of $\text{Ba}_{0.5}\text{Sr}_{0.5}\text{TiO}_3$ thin films. *Journal of Applied Physics*, 107, 074105, 2010.

Teng, Y., Sharafudeen, K., Zhou, S. F., and Qiu, J. R., Glass-ceramics for photonic devices. *Journal of The Ceramic Society of Japan*, 120, 458-466, 2012.

Tessler, N., Medvedev, V., Kazes, M., Kan, S. H., and Banin, U., Efficient near-infrared polymer nanocrystal light-emitting diodes. *Science*, 295, 1506-1508, 2002.

Tong, F., Hao, J. H., Chen, Z. P., Gao, G. Y., and Miao, X. S., Phase-change control of ferromagnetism in GeTe-based phase change magnetic thin-films by pulsed laser deposition. *Applied Physics Letters*, 99, 081908, 2011.

Tong, F., Hao, J. H., Chen, Z. P., Gao, G. Y., Tong, H., and Miao, X. S., Anomalous second ferromagnetic phase transition as a signature of spinodal decomposition in Fe-doped GeTe diluted magnetic semiconductor. *Applied Physics Letters*, 99, 202508, 2011.



Tsang, M.-K., Bai, G., and Hao, J., Stimuli responsive upconversion luminescence nanomaterials and films for various applications. *Chemical Society Reviews*, 44, 1585-1607, 2015.

Usovich, O. V., Trusov, L. A., Lennikov, V. V., de la Fuente, G., Veber, A. A., and Kazin, P. E., Laser-assisted production of Bi-doped silica glasses. *Materials Letters*, 85, 44-46, 2012.

Van Deun, R., Nockemann, P., Gorller-Walrand, C., and Binnemans, K., Strong erbium luminescence in the near-infrared telecommunication window. *Chemical Physics Letters*, 397, 447-450, 2004.

Wang, R. and Zhang, F., NIR luminescent nanomaterials for biomedical imaging. *Journal of Materials Chemistry B*, 2, 2422-2443, 2014.

Wang, X. L., Sheng, Q. C., Hu, L. L., and Zhang, J. J., Observation of broadband infrared luminescence in a novel Bi-doped P_2O_5 - B_2O_3 - Al_2O_3 glass. *Materials Letters*, 66, 156-158, 2012.

Wang, X. S., Xu, C. N., Yamada, H., Nishikubo, K., and Zheng, X. G., Electro-mechano-optical conversions in Pr^{3+} -doped $BaTiO_3$ - $CaTiO_3$ ceramics. *Advanced Materials*, 17, 1254, 2005.

Won, N., Jeong, S., Kim, K., Kwag, J., Park, J., Kim, S. G., and Kim, S., Imaging depths of near-infrared quantum dots in first and second optical windows. *Molecular*



Imaging, 11, 338, 2012.

Wu, B. T., Qiu, J. R., Wu, E., and Zeng, H. P., Broadband near-infrared luminescence from transparent glass-ceramics containing Ni²⁺-doped SrTiO₃ nanocrystals. *Optical Materials*, 35, 983-987, 2013.

Wu, B. T., Ruan, J., Qiu, J. R., and Zeng, H. P., Enhanced broadband near-infrared luminescence from Ni in Bi/Ni-doped transparent glass ceramics. *Journal of Physics D-applied Physics*, 42, 135110, 2009.

Wu, B. T., Zhou, S. F., Ruan, J., Qiao, Y. B., Chen, D. P., Zhu, C. S., and Qiu, J. R., Enhanced broadband near-infrared luminescence from transparent Yb³⁺/Ni²⁺ codoped silicate glass ceramics. *Optics Express*, 16, 1879-1884, 2008.

Wu, B. T., Zhou, S. F., Qiu, J. R., Peng, X. Y., Yang, L. Y., Jiang, X. W., and Zhu, C. S., Transparent Ni²⁺-doped MgO-Al₂O₃-SiO₂ glass ceramics with broadband infrared luminescence. *Chinese Physics Letters*, 23, 2778-2781, 2006.

Wu, X., Rare-earth-doped KNN-based Ceramics for Photoluminescent and Electro-optic Applications. Thesis of The Hong Kong Polytechnic University, 2014.

Wu, Z. P., Huang, W., and Hao, J. H., Growth mode and dielectric properties in laser MBE grown multilayer of SrTiO₃ and YBa₂Cu₃O_y. *Vacuum*, 85, 639-642, 2010.

Wu, Z. P., Huang, W., Wong, K. H., and Hao, J. H., Structural and dielectric



properties of epitaxial SrTiO₃ films grown directly on GaAs substrates by laser molecular beam epitaxy. *Journal of Applied Physics*, 104, 2008.

Xiang, H., Cheng, J., Ma, X., Zhou, X., and Chruma, J. J., Near-infrared phosphorescence: materials and applications. *Chemical Society Reviews*, 42, 6128-6185, 2013.

Xiao, B., Avrutin, V., Liu, H., Rowe, E., Leach, J., Gu, X., Özgür, Ü., Morkoç H., Chang, W., Alldredge, L. M. B., Kirchoefer, S. W., and Pond, J. M., Effect of large strain on dielectric and ferroelectric properties of Ba_{0.5}Sr_{0.5}TiO₃ thin films. *Applied Physics Letters*, 95, 2009.

Xu, B. B., Bai, G. X., Wang, J. C., Guo, Q. B., Tan, D. Z., Chen, W. B., Liu, X. F., Zhou, S. F., Hao, J. H., and Qiu, J. R., Enhanced broadband excited upconversion luminescence in Ho-doped glasses by codoping with bismuth. *Optics Letters*, 39, 3022-3025, 2014.

Xu, B. B., Chen, P., Zhou, S. F., Hong, Z. L., Hao, J. H., and Qiu, J. R., Enhanced broadband near-infrared luminescence in Bi-doped glasses by co-doping with Ag. *Journal of Applied Physics*, 113, 2013.

Xu, B., Tan, D., Zhou, S., Hong, Z., Sharafudeen, K. N., and Qiu, J., Enhanced broadband near-infrared luminescence of Bi-doped oxyfluoride glasses. *Optics Express*, 20, 29105-11, 2012.



Xu, B. B., Hao, J. H., Zhou, S. F., and Qiu, J. R., Ultra-broadband infrared luminescence of Bi-doped thin-films for integrated optics. *Optics Express*, 21, 18532-18537, 2013.

Xu, B. B., Zhou, S. F., Tan, D. Z., Hong, Z. L., Hao, J. H., and Qiu, J. R., Multifunctional tunable ultra-broadband visible and near-infrared luminescence from bismuth-doped germanate glasses. *Journal of Applied Physics*, 113, 2013.

Xu, J. and Su, L. B., Main-group Metal Ions doped Materials-A New Developing Direction of Laser Materials. *Journal of Inorganic Materials*, 26, 347-353, 2011.

Xu, S. Y., Yeh, Y. W., Poirier, G., McAlpine, M. C., Register, R. A., and Yao, N., Flexible Piezoelectric PMN-PT Nanowire-Based Nanocomposite and Device. *Nano Letters*, 13, 2393-2398, 2013.

Xu, X. D., Zhao, Z. W., Song, P. X., Zhou, G. Q., Xu, J., and Deng, P. Z., Infrared (1.2-1.6 μm) luminescence in Yb, Cr : YAG with 940 nm diode pumping. *Materials Science and Engineering B-Solid State Materials for Advanced Technology*, 117, 17-20, 2005.

Xu, Y. S., Qi, J. N., Lin, C. G., Zhang, P. Q., and Dai, S. X., Nanocrystal-enhanced near-IR emission in the bismuth-doped chalcogenide glasses. *Chinese Optics Letters*, 11, 2013.

Yang, R., Mao, M. F., Zhang, Y., Zhuang, Y. X., Zhang, K., and Qiu, J. R.,



Broadband near-infrared emission from Bi-Er-Tm Co-doped germanate glasses. *Journal of Non-crystalline Solids*, 357, 2396-2399, 2011.

Yang, Z. B. and Hao, J. H., In-plane dielectric properties of epitaxial $\text{Ba}_{0.7}\text{Sr}_{0.3}\text{TiO}_3$ thin films grown on GaAs for tunable device application. *Journal of Applied Physics*, 112, 054110, 2012.

Yang, Z. W., Liu, Z. L., Song, Z. G., Zhou, D. C., Yin, Z. Y., and Qiu, J. B., Investigation on origin of broadband infrared emission in Bi doped aluminosilicate glasses. *Materials Research Innovations*, 15, 264-267, 2011.

Yu, J., Zhou, P., Zhao, H. Y., Wu, F., Xia, H. P., Su, L. B., and Xu, J., Study on near-infrared broadband emission spectroscopic properties of Bi-doped alpha- BaB_2O_4 single crystal induced by gamma-irradiation. *Acta Physica Sinica*, 59, 3538-3541, 2010.

Yuan, Z., Lin, Y., Weaver, J., Chen, X., Chen, C., Subramanyam, G., Jiang, J., and Meletis, E., Large dielectric tunability and microwave properties of Mn-doped (Ba, Sr) TiO_3 thin films. *Applied Physics Letters*, 87, 152901-152901-3, 2005.

Zannoni, E., Cavalli, E., Toncelli, A., Tonelli, M., and Bettinelli, M., Optical spectroscopy of $\text{Ca}_3\text{Sc}_2\text{Ge}_3\text{O}_{12}:\text{Ni}^{2+}$. *Journal of Physics and Chemistry of Solids*, 60, 449-455, 1999.

Zhai, Z., Wu, X., Jiang, Z., Hao, J., Gao, J., Cai, Y., and Pan, Y., Strain distribution



in epitaxial SrTiO₃ thin films. *Applied Physics Letters*, 89, 262902-3, 2006.

Zhang, J., Sathi, Z. M., Luo, Y., Canning, J., and Peng, G. D., Toward an ultra-broadband emission source based on the bismuth and erbium co-doped optical fiber and a single 830 nm laser diode pump. *Optics Express*, 21, 7786-92, 2013.

Zhang, K., Zhou, S. F., Zhuang, Y. X., Yang, R., and Qiu, J. R., Bandwidth broadening of near-infrared emission through nanocrystallization in Bi/Ni co-doped glass. *Optics Express*, 20, 8675-8680, 2012.

Zhang, N., Qiu, J. R., Dong, G. P., Yang, Z. M., Zhang, Q. Y., and Peng, M. Y., Broadband tunable near-infrared emission of Bi-doped composite germanosilicate glasses. *Journal of Materials Chemistry*, 22, 3154-3159, 2012.

Zhang, N., Sharafudeen, K. N., Dong, G. P., Peng, M. Y., and Qiu, J. R., Mixed Network Effect of Broadband Near-Infrared Emission in Bi-Doped B₂O₃-GeO₂ Glasses. *Journal of The American Ceramic Society*, 95, 3842-3846, 2012.

Zhang, P. X., Zhang, H., Cha, L. M., and Habermeier, H. U., Tailoring the physical properties of manganite thin films by tuning the epitaxial strain. *Physica B-Condensed Matter*, 327, 257-261, 2003.

Zhang, Y. Optical properties and modulated luminescence of metal ion doped phosphors. Thesis of The Hong Kong Polytechnic University, 2012.



Zhang, Y. and Hao, J., Metal-ion doped luminescent thin films for optoelectronic applications. *Journal of Materials Chemistry C*, 1, 5607-5618, 2013.

Zhang, Y., Hao, J., Mak, C. L., and Wei, X., Effects of site substitutions and concentration on upconversion luminescence of Er³⁺-doped perovskite titanate. *Optics Express*, 19, 1824-1829, 2011.

Zhang, Y., Gao, G. Y., Chan, H. L. W., Dai, J. Y., Wang, Y., and Hao, J. H., Piezo-Phototronic Effect-Induced Dual-Mode Light and Ultrasound Emissions from ZnS:Mn/PMN-PT Thin-Film Structures. *Advanced Materials*, 24, 1729-1735, 2012.

Zhao, H. Y., Yu, P. S., Guo, X., Su, L. B., Li, X. N., Fang, X. M., Yang, Q. H., and Xu, J., Near-infrared broadband emission spectroscopic properties of Bi: alpha-BaB₂O₄ single crystal induced by electron irradiation. *Acta Physica Sinica*, 60, 2011.

Zheng, F. G., Xin, Y., Huang, W., Zhang, J. X., Wang, X. F., Shen, M. R., Dong, W., Fang, L., Bai, Y. B., Shen, X. Q., and Hao, J. H., Above 1% efficiency of a ferroelectric solar cell based on the Pb(Zr,Ti)O₃ film. *Journal of Materials Chemistry A*, 2, 1363-1368, 2014.

Zhou, S. F., Dong, H. F., Zeng, H. P., Feng, G. F., Yang, H. C., Zhu, B., and Qiu, J. R., Broadband optical amplification in Bi-doped germanium silicate glass. *Applied Physics Letters*, 91, 2007.

Zhou, S. F., Dong, H. F., Zeng, H. P., Hao, J. H., Chen, J. X., and Qiu, J. R., Infrared



luminescence and amplification properties of Bi-doped GeO₂-Ga₂O₃-Al₂O₃ glasses. *Journal of Applied Physics*, 103, 103532, 2008.

Zhou, S. F., Lei, W. Q., Jiang, N., Hao, J. H., Wu, E., Zeng, H. P., and Qiu, J. R., Space-selective control of luminescence inside the Bi-doped mesoporous silica glass by a femtosecond laser. *Journal of Materials Chemistry*, 19, 4603-4608, 2009.

Zhou, S., Li, C., Yang, G., Bi, G., Xu, B., Hong, Z., Miura, K., Hirao, K., and Qiu, J., Self-Limited Nanocrystallization-Mediated Activation of Semiconductor Nanocrystal in an Amorphous Solid. *Advanced Functional Materials*, 23, 5436, 2013.

Zhou, B., Lin, H., Chen, B., and Pun, E. Y., Superbroadband near-infrared emission in Tm-Bi codoped sodium-germanium-gallate glasses. *Optics Express*, 19, 6514-23, 2011.

Zhou, S. F., Hao, J. H., and Qiu, J. R., Ultra-Broadband Near-Infrared Luminescence of Ni²⁺: ZnO-Al₂O₃-SiO₂ Nanocomposite Glasses Prepared by Sol-Gel Method. *Journal of The American Ceramic Society*, 94, 2902-2905, 2011.

Zhou, S. F., Jiang, N., Miura, K., Tanabe, S., Shimizu, M., Sakakura, M., Shimotsuma, Y., Nishi, M., Qiu, J. R., and Hirao, K., Simultaneous Tailoring of Phase Evolution and Dopant Distribution in the Glassy Phase for Controllable Luminescence. *Journal of The American Chemical Society*, 132, 17945-17952, 2010.

Zhou, S. F., Jiang, N., Dong, H. F., Zeng, H. P., Hao, J. H., and Qiu, J. R., Size-



induced crystal field parameter change and tunable infrared luminescence in Ni²⁺-doped high-gallium nanocrystals embedded glass ceramics. *Nanotechnology*, 19, 015702, 2008.

Zhou, S. F., Jiang, N., Wu, B. T., Hao, J. H., and Qiu, J. R., Ligand-Driven Wavelength-Tunable and Ultra-Broadband Infrared Luminescence in Single-Ion-Doped Transparent Hybrid Materials. *Advanced Functional Materials*, 19, 2081-2088, 2009.

Zhou, S. F., Jiang, N., Zhu, B., Yang, H. C., Ye, S., Lakshminarayana, G., Hao, J. H., and Qiu, J. R., Multifunctional bismuth-doped nanoporous silica glass: From blue-green, orange, red, and white light sources to ultra-broadband infrared amplifiers. *Advanced Functional Materials*, 18, 1407-1413, 2008.